UNIVERSITY OF OKLAHOMA

GRADUATE COLLEGE

ASSESSMENT OF ULTRA-HIGH-PERFORMANCE-CONCRETE (UHPC) PROPERTIES USING DIFFERENT FIBERS

A THESIS

SUBMITTED TO THE GRADUATE FACULTY

in partial fulfillment of the requirements for the

Degree of

MASTER OF SCIENCE

By

DIP BANIK
Norman, Oklahoma
2022

ASSESSMENT OF ULTRA-HIGH-PERFORMANCE-CONCRETE (UHPC) PROPERTIES USING DIFFERENT FIBERS

A THESIS APPROVED FOR THE
SCHOOL OF CIVIL ENGINEERING AND ENVIRONMENTAL SCIENCE

BY THE COMMITTEE CONSISTING OF

Dr. Royce Floyd, Chair

Dr. Jeffery Volz

Dr. Shreya Vemuganti

ACKNOWLEDGEMENTS

I would like to extend my heartfelt thanks and appreciation to my advisor Dr. Floyd for his guidance throughout the research. It helped me learn the procedure for conducting experimental research and how to express the outcomes in this thesis. I also would like to thank the rest of my thesis committee members, Dr. Jeffery Volz and Dr. Shreya Vemuganti, for their comments to improve the thesis.

I want to thank my parents, and my fiancée, Srejoni Dutta, who are the greatest source of strength and support in my life. Their encouragement propelled me to follow my academic goals with passion and interest.

During my research, I had unconditional help from Omar Yadak, fellow grad student and researcher and John Bullock, FEARS Lab manager regarding building and testing of my specimens. Also, I had the privilege of working with a team of dedicated and talented students, including Stephen Roswurm, Zach Tiry, Mujtaba Ahmadi, Cade Harris, Jacob Starks, Trevor Looney, Jacob G. Choate, who made it possible to complete the project on time, and I am grateful to all of them.

Table of Contents

List of Tables

List of Figures

Abstract

Ultra-high-performance-concrete (UHPC) is a cementitious material with a high compressive strength, densely packed structure resulting in near zero permeability, small crack opening, and significant post-cracking tensile strength. UHPC has both mechanical properties and durability exceeding those of normal strength concrete. However, these properties come with a substantial material cost, with most of the cost associated with the fiber amounts. In this research, the effect of both fiber content (1, 2, 4 and 6% by volume) and type (0.5 in. straight microfibers and 1.2 in. hooked-end fibers) on UHPC properties has been studied in a non-proprietary UHPC mix developed at the University of Oklahoma (J3). Compression, flexure, direct tensile, and splitting tensile behaviors emphasizing strain responses of J3 concrete have been examined in this study to better understand the linear-elastic response, fiber bridging property and failure mode. Also, the study of flexure behavior of J3 concrete with hooked-end fibers subjected to freezing-thawing cycles in both pre-cracked and uncracked specimens was undertaken to better understand the effect of initial cracking on durability and actual damage of rapid freezing and thawing on the concrete matrix.

Furthermore, UHPC was used to retrofit a half-scale AASHTO Type-II prestressed girder which was failed using a point load positioned to induce bond shear failure. The beams were then repaired by encapsulating the failure zone using J3 mix with 2% straight microfibers. Though this process did not restore the prestress, it successfully restored original shear capacity and created an impermeable layer to prevent water ingress into the existing cracks.

Chapter 1 Introduction

1.1 Background

Concrete has been produced and used for different structural purposes since Roman times. However, the idea of producing a concrete having very high strength owing to dense microstructure was put forward beginning in the 1980s. The practical advancement was accompanied by improvement of steel microfibers, a particularly effective superplasticizer that empowered the development of a cementitious matrix with a high extent of firmly packed supplementary cementitious materials, and simultaneously a low water/binder proportion of just around 0.20 with a flowable consistency [1]. The optimum combination of dense packing with low water/binder ratio is what gives ultra-high-performance concrete (UHPC) its special properties. UHPC class materials can massively outperform conventional concrete in terms of mechanical and durability properties, owing to a very dense discontinuous pore structure and high volume of high-strength steel microfiber reinforcement.

Though definitions of UHPC vary, generally it is accepted as having compressive strength greater than 17.4 ksi and a minimum direct tensile strength of 0.72 ksi [2]. The Federal Highway Administration (FHWA) defines UHPC as a densely packed cementitious material with a water/binder ratio less than 0.25 having compressive strength over 21.7 ksi and post-cracking tensile strength over 0.72 ksi [3]. The American Concrete Institute (ACI) defines UHPC as concrete having a 22 ksi minimum compressive strength, with specified durability, tensile ductility and toughness [4]. To acknowledge the key importance fibers play in the characteristics of UHPC, it is also referred to as ultra-high performance fiber reinforced concrete (UHPFRC) in some places [2]. The main potential usage of UHPC may be in the precast industry as lighter and durable components for accelerated construction are possible due superior material properties. Also, the long-term benefits of using UHPC in many applications are evident. However, commercially available UHPC mixes can cost 20 times more than conventional concrete, which has significantly limited the spread of UHPC. Moreover, 50% or more of this cost is associated with the fiber reinforcement [5]. Many organizations have responded to this problem by developing lower-cost UHPC mix designs with locally available components [6]–[9] that provide additional flexibility relative to commercially available solutions. Over the last few years, researchers [6], [10] at the University of Oklahoma (OU) have developed a non-proprietary UHPC class material (designated J3) using locally available materials to make it cost-effective. It is being extensively tested to tailor its properties for suitability to be used in expansion joint headers, slab connections, link slabs, beam end repairs, continuity joints and so on. The challenge is to further reduce the cost of J3 concrete while providing required properties, and the best way to do this is to tailor the amount of steel fibers to the given application since these are the most expensive component and have little impact on the particle optimization of the developed mix.

1.2 Purpose

The study described in this thesis was undertaken to better understand the properties of J3 concrete with varying fiber types and contents and its potential application to retrofit prestressed concrete girders subjected to end region damage.

Under this research work compressive, tensile (flexure, split tensile, direct tensile) responses and freeze-thaw resistance of J3 with different fiber types were measured. One approximately half-scale AASHTO Type-II girder was cast, tested, repaired, and re-tested to understand the repair's contribution in restoring girder's shear capacity.

1.3 Objectives

The underlying objectives of this study are as follows.

- Identify suitable fiber type and volume fraction for J3 concrete to be used for structural purposes.
- Quantify the damage induced to the J3 concrete if exposed to rapid weather changes.
- Identify the efficiency of J3 concrete with specific fibers in restoring shear damage of a prestressed girder.

Chapter 2 Literature Review

2.1 Overview

This section provides a summary of a wide range of literature that relates to the general characteristics of UHPC and how fibers impact different properties of UHPC.

The UHPC matrix is densely packed to ensure a discontinuous pore structure and near zero permeability [1]. Portland cement, fine-grained sand, silica fume, water, superplasticizer, and steel fibers are the typical constituents used for UHPC to ensure high-strength, ductility and sustainability [11]. These superior properties of UHPC enable the manufacturers to reduce the weight of structures by creating smaller sections. Figure 1 depicts the packing system of both conventional concrete and UHPC as well as the difference in section sizes. However, without steel reinforcement, concrete is liable to be brittle and the cracks cannot be stopped [11]. So, it is important to reinforce UHPC with steel fibers to ensure better resistance towards crack generation and improve the tensile capacity and fracture resistance [12].

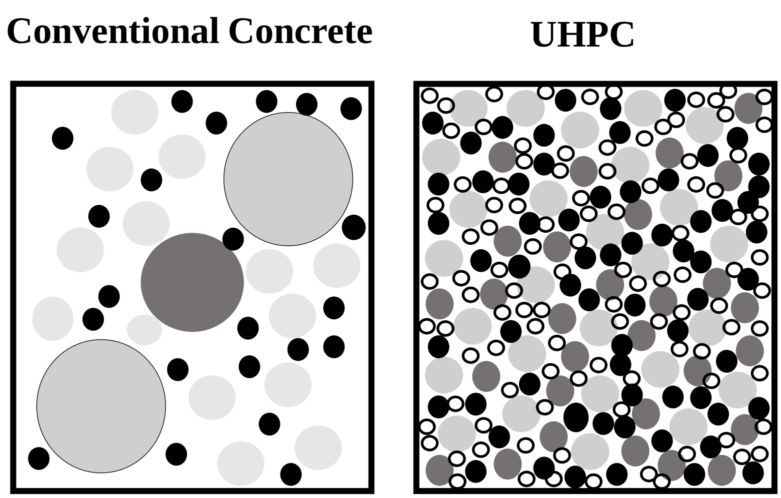

Figure 1. Particle packing for conventional concrete vs UHPC [13]

The OU developed J3 concrete has been optimized to get maximum packing density using fine sand, Type-I/II cement, silica fume, slag cement, water, steel microfibers and superplasticizer [6]. As fibers can vary in geometry, materials, and availability, it is important to understand the combined effect of the local materials used in J3 concrete and the type of fibers incorporated.

2.2 Influence of Fiber Incorporation on Properties of UHPC

Fibers enhance the intrinsic rigidity of the concrete matrix, and introduce a crack-restraining effect which in return improves the mechanical properties of UHPC [14]. Fiber incorporation can ensure ductility in tensile behavior and change the brittle compressive failure to a ductile failure [15]. However, several factors relating to fibers can contribute to the degree of enhancement of UHPC properties, such as type, content, shape, aspect ratio, orientation, and distribution [1]. Some researchers have suggested that deformed hooked-end fibers can perform better than straight fibers [11], [14]. In terms of fiber content, there are still debates about the exact amount up to which it is beneficial to increase the fiber amount considering cost/benefit ratio. However, researchers have agreed that excessive fiber contents in UHPC can hamper uniform fiber dispersion and thus impair the mechanical properties [16]–[18].

2.2.1 Effect of Fibers on the Compressive Response

Post-peak compressive response of UHPC is significantly impacted by incorporation of fibers, though fibers have close to no effect on the rising-portion of the stress-strain curve [1], [19]. In other words, fiber inclusion changes failure in compression from brittle to ductile. Inclusion of fibers can introduce superior resistance to crack formation and propagation which in return can benefit the overall compressive properties of the UHPC matrix [20], [21]. Some researchers reported less than 10% or no substantial increase in compressive strength as a result of fiber inclusion [22], [23]. However, substantial improvements (above 50%) in compressive strength for UHPC with fibers relative to UHPC without fibers have also been reported in several studies [19]–[21]. Some researchers have suggested a positive relationship between compressive strength and fiber content up to a certain point [19]–[21], [24]–[26]. However, fiber agglomeration in the concrete mix is also a possibility and some researchers suggested that the possibility of agglomeration is increased significantly with fiber contents exceeding 3% by volume [15], [27], which in turn adversely affects the compressive strength of the concrete [28]. Researchers are also not in agreement about the impact of fiber amounts on the elastic modulus of UHPC. One study reported improvement in compressive elastic modulus with increasing fiber contents up to 3% by volume [28]. However, one study stated no noticeable improvement in elastic modulus with inclusion of fibers [15].

2.2.2 Effect of Fibers on the Tensile Response

The largest benefit of fiber inclusion in UHPC can be observed in tensile behavior. Increased fiber amounts have positive impacts on tensile strength, fracture energy capacity and post-cracking behavior [1], [19]. Though post-cracking tensile strength is significantly impacted by fibers, proper fiber distribution and volume has insignificant but positive impact on pre-cracking tensile behavior [29] According to previous researchers [30], [31], deflection-hardening behavior resulting in higher load carrying capacity after the first crack is a prominent feature of UHPC with fibers under tension. By bridging fractures and transmitting stress across them, fibers enable the concrete to maintain structural integrity under tension after initial cracking. After peak load, a stress-sustaining zone is also typically observed due to repeated fiber bridging and then pullout of fibers [19].

An almost pseudo-linear increase in flexural strength with increasing fiber volume fractions was reported by several researchers [19], [21], [28], [31]. One possibility might be that higher fiber concentration ensures more tightly spaced fibers and thus ensures better bond between the concrete matrix and fibers and better management of fracture propagation [32], [33]. Flexural toughness, which is an indicator of post-cracking flexural resistance and fiber efficiency, is also significantly influenced by varying fiber concentration in the concrete mix [15], [19], [31]. Deformed fibers can impart better crack bridging properties because of higher pullout strength [27], [34]. Comparing the impact of utilizing different deformed fibers with 0.5 in. straight micro-fibers, the impact of utilizing deformed fibers varies from a 5% decrease [33], [35] to a 40% increase [36]. Yoo et al.[33] reported that UHPFRC fiber volume up to 1% of single fiber, deformed fibers showed the highest strength, and above that fiber percentage, straight fibers performed better. The reason can be a weakening of the concrete matrix due to a high number of split cracks introduced by pulling out of fibers with a higher bond strength.

According to Graybeal and Baby [37] introducing fibers can break the uniaxial tension response of UHPC into four distinct phases: elastic, multi-cracking, crack straining, and crack localization. Hoang and Fehling [15] reported that the steel fiber amount does not influence the linear elastic stage, however, fiber content and aspect ratio can significantly impact the post-cracking behavior. One research program suggested that fibers can nearly double the direct tensile strength comparing with unreinforced UHPC [38]. Wille et al. [39] looked into the tensile behavior of both straight (volume = 2%, 2.5%, 3%) and hooked-end (volume = 1.5%, 2%, 3%) fibers and reported strong fiber volume dependency and fiber type insensitivity. Liu et al. [40] also measured the effect of fiber geometry and type on direct tensile strength of UHPC and reported that both geometry and content have positive impact on tensile properties, however, the utilization efficiency of fibers degrades with increasing fiber content. However, some researchers have reported a decrease in uniaxial tensile strength for hooked-end fibers comparing to straight fibers because of fiber clotting and damage in the matrix due to superior bond strength [41].

The inherent problem with direct tensile strength lies with the appropriate specimen size. The boundary conditions of smaller specimens significantly influence the fracture process zone, and the larger size causes the specimens to flex sideways, which is a result of non-uniform cracks [42]. These effects are exacerbated while making specimens with higher fiber amounts as the fiber distribution is highly affected and cannot represent actual full-scale structures [43]. Splitting tensile strength specimens can create representative samples of actual structure because of the nature of the specimen shape. However, the split tensile test has one downside. Because of the existence of biaxial state of stress in the location of tensile crack, the post-cracking behavior found from the splitting tensile test does not represent the actual tensile post-cracking behavior [43], [44]. However, inclusion of fibers in concrete matrix can increase the first-cracking strength of specimens under splitting tensile strength [30], [45]. Haber et al.[46] tested different specimens having 1.18 in. hooked-end fibers with 3% volume fractions and 0.5 in. straight fibers with 1%-4.5% fiber contents having different dry components ratios under splitting tensile test. This experiment reported that fiber types and fractions did not have any influence on the first cracking strength and failed to establish any correlation between first cracking or cracking strength with fiber volume fractions in the splitting tensile test. However, Qadir et al.[45] tested UHPC with 1% - 4% straight fibers (0.25 in. long) with two different w/c ratios and reported an increase in splitting tensile strength with increasing fiber volumes. Another study with fiber-reinforced concrete having 0.5% - 2%, 1.4 in. hooked-end fibers also reported an increase in splitting tensile strength with increasing fiber volume [47].

2.2.3 Freeze-Thaw Resistance of UHPC

Several investigations have shown that UHPC shows no degradation after freeze–thaw cycle counts of 300 or 600 and has a durability factor of 100 or higher with almost negligible mass loss [48], [49]. In a few previous studies, mass gain and an increase in dynamic modulus with increase in freeze-thaw cycles were reported [50], [51]. This can be attributed to the self-healing property that occurs when UHPC is submerged in water during freeze-thaw tests and micro-cracks allow water ingression which can hydrate some of the large amount of unhydrated cement particles [52]. One study conducted on concrete with cement, fly ash, silica fume, sand, gravel, and no fibers, reported that maximum applied load, stress, and crack opening decrease with increasing freeze-thaw cycles [51]. Another study done by Yang et al. [53] on conventional concrete with cement, fine aggregate and course aggregate shows that a pre-existing damage zone increases when specimens are exposed to freezing and thawing leading to complete failure of the specimens depending of the intensity of pre-existing damage.

Several investigations reported an increase in freeze-thaw durability with inclusion of fibers in regular concrete [54], [55]. One investigation suggested that under 300 freeze-thaw cycles a ductile fiber-reinforced cementitious composite loses ductility, however, the modulus of rupture remains relatively unchanged [56]. One study demonstrated an insignificant drop in flexural capacity of high-performance cement board specimen withstanding 300 freeze-thaw cycle [57]. One review revealed that for 144 freeze-thaw cycles an induced pre-strain had little impact on the tensile performance of high-performance fiber reinforced concrete (HPFRCC) specimens with a mix of polyvinyl alcohol (PVA) and polyethylene (PE) fibers [58]. Jang et al. [59] studied the effect of 300 cycles of rapid freezing and thawing on sustainable strain-hardening cement composite (2SHCC) with polyethylene terephthalate (PET), and PVA fibers. This study reported that cylinders exposed to freeze-thaw showed average compressive strength of 75% of the virgin specimens. This study also reported decreases in modulus of rupture, interfacial bond, direct tensile strain capacity, and splitting tensile strength of specimens exposed to 300 cycles of freezing and thawing compared to virgin specimens.

2.2.4 UHPC as a Material to Repair Prestressed Girder End Regions

Considering the superior mechanical properties, very low to negligible permeability, superior durability, and high cost, incorporating UHPC into repair and rehabilitation of structures can be a beneficial use of the material. One potential application of UHPC is for repairing a structurally deficient prestressed girder with shear cracks in the end region. Leaking expansion joints can transmit chloride laden water on bridge girder ends and lead to severe corrosion damage. Shear damage may result if corrosion deterioration is combined with increasing load levels. Based on the severity of damage, a damaged member can be repaired, or in severe cases, replaced. The most common approaches for retrofitting a damaged girder are adding new structural elements like steel, external post tensioning, using fiber reinforced polymer reinforcement, or concrete encapsulation. However, due to incompatibility between substrate and repair material, debonding and cracking at the interface can occur, which leads to failure of the repair [60]. Higher strength, ductility, and durability are also important criteria for a repair material rather than just bond to the existing concrete. Considering these requirements, UHPC is the one of the most suited materials. Also, the flowability and self-consolidating properties of UHPC allow for complex formworks required for many repairs. Zmetra et al.[61] used UHPC to repair the end region of a steel bridge girder and reported improved shear capacity, protection against corrosion, and an unchanged ductile failure mode. Shafei et al.[62] used UHPC patches to repair shear damage on bulb-tee-C shaped beams and reported a good bond performance and failure of the substrate concrete before the UHPC patch. Also, Murthy et al.[63] reported that UHPC is not only suitable for restoring shear capacity, but because of less susceptibility to fatigue, it can be an excellent choice to restore flexural damage too. Ahmadi[64] examined using a J3 UHPC encapsulation of prestressed girder end regions subjected to shear damage and Huynh[65] examined using UHPC to restore sections lost due to spalling and corrosion around the prestressing strands at the girder end. Both researchers showed that the repairs produced an increase in load carrying capacity.

2.3 Research Significance

From the extensive review of previous research work, it can be summarized that though much research has been done on UHPC properties, little consensus exists between the researchers about the contributions of fiber types and amount on UHPC properties. As concrete vastly depends on the raw materials, even similar mixes developed using different raw materials or materials from varying sources will show different characteristics.

This research focuses on the characterization of the non-proprietary UHPC mix developed using locally available materials in Oklahoma. This study will reduce the existing knowledge gap about the performance of this non-proprietary mix with varying fiber type and volume fractions. Furthermore, this study will help to understand the significance of rapid change in temperature on a structural element subjected to bending.

Chapter 3 Approach and Methods

3.1 Overview

The baseline UHPC mix design examined in this thesis, identified as J3, was developed in previous research at the University of Oklahoma [6], [10]. The properties of the constituents of J3 mix are presented in Table 1.

Table 1. Key properties of J3 mix ingredients [10].

	Type I Cement	Silica Fume	Slag Cement	Masonry Sand
Source	Dolese	Norchem	LafargeHolcim	Metro Materials
Reaction Type	Hydraulic	Pozzolanic	Pozzolanic	None
Shape of Particle	Angular	Spherical	Amorphous	Angular
Specific Gravity	3.15	2.22	2.97	2.63

Table 2 presents the baseline composition of the UHPC with a 2% fiber content. Mix components were reduced proportionally to maintain the same weight ratio and a constant mix volume with changes in steel fiber content from the baseline 2%. The water-cementitious materials ratio (*w*/*cm*) was kept constant throughout testing, but a polycarboxylate based superplasticizer or High-Range-Water-Reducer (HRWR) named Glenium 7920, acquired from Dolese was used to disperse the water molecules. The HRWR dosage was adjusted from a baseline of 18 oz/cwt (fluid ounces per 100 lb of cementitious material) to ensure the required 8 in. – 10 in. flow.

Table 2. Composition of J3 UHPC (weight ratios).

Constituent	Mix Proportion
Type I Cement	0.3
Silica Fume	0.05
Slag Cement	0.15
Masonry Sand (1:1 agg/cm)	0.5
w/cm	0.2

The research described in this thesis extends the initial studies [6], [66] to examine the mechanical properties of the J3 concrete with different fiber types and contents in compression and tension and compare to those used in previous research on J3. The two main fiber types examined were a new source of 0.5 in. long straight microfibers (ST) with fiber contents of 1%, 2%, 4% and 6% by volume and a 1.2 in. long hooked end (HE) fiber intended for structural applications along with fiber contents of 1%, 2%, and 4% (Figure 2). The fiber percentages were chosen to compare with the works done by Dyachkova [66] at OU. However, for long HE fibers, it was not possible to get a proper mix with 6% fiber volume fraction as fiber clogging was too much in the middle of mixing, which stopped the mixer after addition of fibers even with an extremely high dosage of HRWR. Individual mixes will be identified in this thesis by fiber type and content. For example, mixes with straight microfiber at a 2% fiber volume content will be designated as ST-2%. The properties of two different fiber types used in this research are presented in Table 3.

Figure 2. Two types of steel fibers used in this research.

Table 3. Properties of fibers used in the research.

Fiber Type	Length (in.)	Diameter (in.)	Aspect Ratio	Tensile Strength (ksi)	Specific Gravity
ST	0.5	0.0079	63.6	413	7.8
HE	1.2	0.01	80	290	7.8

Durability of J3 concrete with 2% straight and hooked end fibers was also examined using rapid freeze-thaw cycles on specimens identical to those tested in flexure. The test matrix for the J3 concrete considering different mechanical and durability tests is presented in Table 4. Finally, the end of a prestressed girder damaged in shear using an applied point load was repaired using J3 with ST-2%, and then the loading was repeated to failure. This study was done to examine the effect of changing the fiber type on performance of the J3 material including the efficiency of J3 as a repair material.

Table 4. J3 test matrix including testing day relative to casting (concrete age) and number of specimens tested

Test Starting Day (Concrete Age (Days))	Test Name	Procedure	Fiber Types	Volume Fractions (%)	Specimen Nos.
0	Flow	ASTM C1437 [67]	Both	1,2,4,6	-
3	Compression	ASTM C39 [68]	Both	1,2,4,6	3
28	Compression	ASTM C39 [68]	Both	1,2,4,6	3
	Elasticity Modulus (MOE)	ASTM C469 [69]	Both	1,2,4,6	3
	Flexural Strength	ASTM C78 [70]	ST	1,2,4,6	3
56	Compression	ASTM C39 [68]	Both	1,2,4,6	3
	Flexural Strength	ASTM C78 [70]	Both	1,2,4,6	3
	Splitting Tensile	ASTM C496 [71]	HE	1,2,4	3
	Direct Tension	Graybeal and Baby [37]	Both	1,2,4,6	3
60 +	Freeze-Thaw	ASTM C666 [72]	HE	1,2	4

3.2 Concrete Mixing and Curing Procedure

A fixed mixing procedure originated from McDanial [10] was followed for every mix design tested to maintain consistency throughout the research. A high-shear mechanical mixer was used to provide proper energy. The step-by-step mixing procedure with the required time is documented in Table 5.

Table 5. J3 mixing procedure followed in this research.

Process	Timeline (minutes)
Loading dry materials in the mixer Mixing dry materials	0 – 10
Mixing water and half HRWR	10 – 12
Mixing	12 – 13
Adding remaining HRWR	13 – 14
Mixing	14 – 24 (until the attainment of liquid consistency)
Adding steel fibers (if applicable)	24
Final mixing (if applicable)	24 – 26

Immediately after mixing, concrete was poured into required specimen molds primed with form-release oil. The ST-4%, ST-6% and HE-4% mixes were placed on a vibration table to ensure proper consolidation. All the concrete filled molds were kept in an environmentally controlled chamber with temperature maintained at 73.5 ± 3.5 °F and approximately 50% humidity. All the specimen molds were covered with plastic to ensure negligible moisture loss. All specimens were demolded at 3 days of age and those to be tested at later ages were completely submerged in a lime-water solution until the day of testing. Figure 3 depicts the specimens after 3 days wrapped in plastic in the temperature-controlled chamber and immediately before demolding.

Figure 3. J3 specimens 3 days after casting immediately before demolding.

3.3 Specimen Preparation and test setup

Standard mechanical tests were performed for J3 specimens with varying contents of both HE and ST fibers. The beam-end repair was done only for the ST-2% mix and the freeze-thaw test were done only for the HE-1% and HE-2% mixes.

3.3.1 Flowability

The flowability test was done on fresh concrete immediately after completion of mixing using the mini slump cone according to ASTM C1437 [67] with modification for UHPC from ASTM C1856 [73] as shown in Figure 4. The cone was filled and lifted, and the uninterrupted spread of concrete after two minutes was the governing parameter measured in this test. The average of two perpendicular flow diameters was recorded as the flow of that specific concrete mix. The targeted flow was 8 in. – 10 in., however, for mixes with 4% and 6% fiber volume, it was not possible to get that flow without causing segregation of the concrete matrix.

Figure 4. Slump flow test of J3 concrete

3.3.2 Compressive Strength and Elasticity Modulus

Compressive strength tests were performed on 3-in. diameter by 6-in. long cylinders in accordance with ASTM C39 [68] with the modifications listed for UHPC in ASTM C1856 [73]. A total of nine cylinders were tested (three at each age) for measuring compressive strength at 3, 28 and 56 days of age for each fiber percentage. Considering the strength of UHPC, the loading rate for all compression tests (including elasticity modulus (MOE) tests) was adjusted to 150 psi/s based on ASTM C1856 [73]. All cylinders were ground plane using a cylinder end grinder immediately before testing. Figure 5 depicts the concrete cylinders surfaces before and after grinding.

Figure 5. J3 cylinders before and after grinding

For the 28 days compression test linear voltage differential transformers (LVDT) having 1-in. stroke were used to measure axial strain for three specimens of each fiber content as shown in Figure 6. The average values from the three LVDTs were used to derive peak strain for the specimens. The LVDTs measured movement between the machine platen and loading head and the resulting measurements included deformation of the spacer plates used for the tests. The filler plates used in the axial stress-strain tests were made of high-quality steel and the axial deflection of the steel plates calculated from the variable loads were subtracted from the total deflection to determine the cylinder deformation and resulting stress-strain relationship of the cylinders.

Figure 6. Test setup to measure axial compressive strain.

The elasticity modulus (MOE) test was performed on three 4-in. diameter by 8-in. long cylinders in accordance with ASTM C469 [69] and with modifications for UHPC from ASTM C1856 [73]. This test was done at 28 days of age and the maximum applied axial stress was 40% of the compressive strength measured for each fiber amount at the same age. An LVDT was attached to the compressometer ring to measure deformation of the cylinders (Figure 7) and these values were used along with the compressometer gauge length to determine strain. The chord elasticity modulus was determined using load and strain values at a strain of 50 millionths and at a stress of 40% of the compressive strength using Equation 1.

$$E = \frac{S_2 - S_1}{\varepsilon_2 - 0.00005} \tag{1}$$

Where, E = chord modulus of elasticity (psi), S_2 = stress corresponding to 40% of ultimate load (psi), S_1 = stress corresponding to a longitudinal strain, ε_1, of 50 millionths (psi), and ε_2 = longitudinal strain corresponding to stress S_2.

Figure 7. MOE test setup for J3 concrete

3.3.3 Flexural Strength/Modulus of Rupture (MOR)

The flexural strength test was performed on three 3-in. by 3-in. by 12-in. prisms utilizing the methods of ASTM C78 [70] and ASTM C1609 [74] at 28 days of age (for J3 with only ST fibers) and 56 days of age (for J3 with both type of fibers). Care was taken to facilitate randomness in the orientations of the fibers during concrete casting as concrete placement can significantly influence the flexural performance of UHPC [31]. The loading rate was adjusted to 17.5 psi/s from that specified in the ASTMs due to the capacity of available testing equipment relative to deflection control and available data storage considering the high strength. In addition to measuring peak load, vertical deflection of the specimens was measured for calculating toughness using two LVDTs at mid span. An additional LVDT was attached at the bottom of each specimen to measure overall crack width. The test setup for the MOR test is shown in Figure 8.

Figure 8. Flexural strength (MOR) test setup

The bending strength of specimens was calculated using the Equation 2 at the point of interest if the fracture initiated in the middle third of the span length and Equation 3 if the initiated fracture formed outside the middle third by no more than 5% of the total span length. If the fracture initiated elsewhere, the specimens were discarded and not considered for calculating flexural capacity.

$$R = \frac{PL}{bd^2} \tag{2}$$

$$R = \frac{3Pa}{bd^2} \tag{3}$$

Where P = sustained load (lb) at point of interest, L = span length (in.), b = average width of the specimen at fracture (in.), d = average depth of specimen at fracture (in.), a = average distance between line of fracture and the nearest support measured on the tension surface of the beam (in.).

3.3.4 Direct Tensile Strength

The direct tensile test assembly was based on previous research work done at the University of Oklahoma by Campos [75], which was a modification of a testing apparatus designed by Graybeal and Baby [37] to suit the available equipment. Three prismatic specimens having 2-in. by 2-in. by 17-in. dimensions were tested at 56 days of age. The specimen length and gripping plate dimensions were selected to minimize stress concentrations during original development of the testing method [37]. The test setup is shown in Figure 9. Hinges were used at the top and bottom of the loading apparatus, and a neoprene pad and a rod were used to create a swivel at the bottom connection to allow the testing assembly to self-align with the tensile load to ensure concentric loading and help avoid bending stress. A loading rate between 100 lb/sec and 150 lb/sec was used to test the specimens due to equipment limitations for strain-controlled loading. Steel collars were placed 5.5 in. apart to create the measurement gauge length and an LVDT was placed on each side of the test specimen to measure deformation during testing as shown Figure 9.

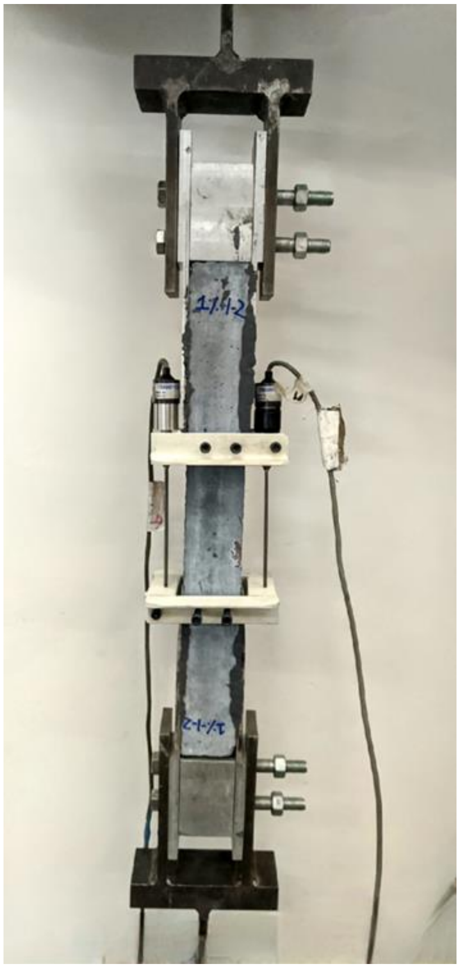

Figure 9. Direct tensile strength test setup

3.3.5 Splitting Tensile Strength

Splitting tensile strength testing was performed on a set of three 3-in. diameter cylinders for each fiber content in accordance with ASTM C496 [71] with modifications listed in ASTM C1856 [73] for UHPC. After recording the dimensions of the cylinders using caliper, a diametrically applied compressive force was applied along the length at a rate resulting in 2.5 psi/s on the expected failure surface. A strip of Masonite hardboard was placed between the specimen and each loading plate to uniformly distribute the load and minimize stress concentrations near the point of load application. An LVDT was placed at each end of the cylinder attached to aluminum angles glued to the specimen face and spaced 1-in. apart to measure deflection perpendicular to the loading direction (crack opening) as shown in Figure 10. The typical procedure is to stop the test when the cylinder splits into halves along a vertical plane, however as fibers hold major cracks together in UHPC, the test was continued past the point of first cracking. For that reason, the final failure occurred due to the crushing of the specimens as depicted in Figure 10. The first cracking load was used to calculate the splitting tensile strength of the specimens as the load bearing capacity beyond first crack was related to enhanced fiber pull-out resistance of the specimens due to compressive forces running parallel to the cracks rather than the actual tensile strength [44]. Equation 4 was used to calculate the splitting tensile strength of the specimen at different points of interest.

$$T = \frac{2P}{\pi l d} \tag{4}$$

Where, T = splitting tensile strength (psi) at point of interest, P = load indicated by machine (lb) at point of interest, l = length of specimen (in.), and d = specimen diameter (in.)

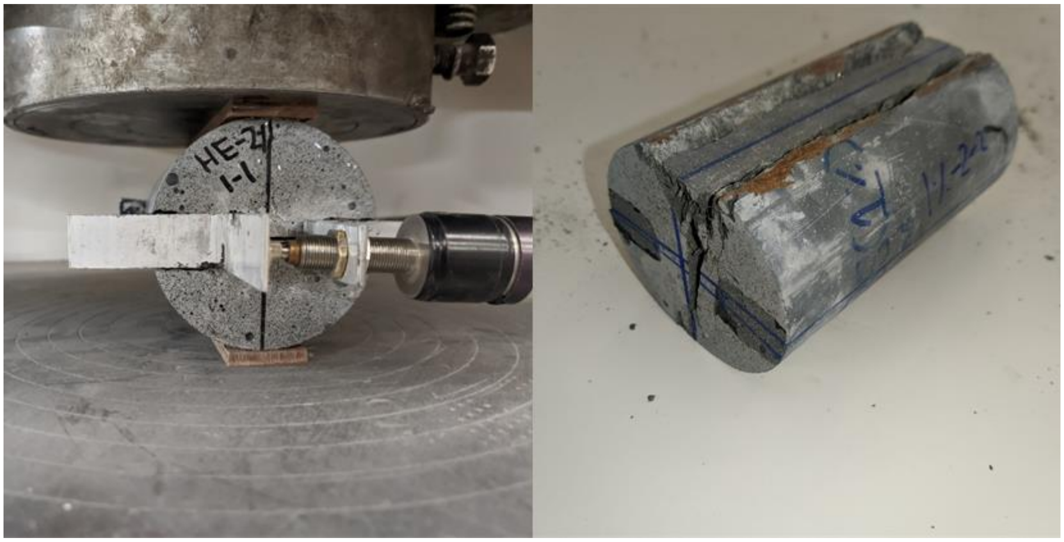

Figure 10. Splitting tensile strength test setup (left) and the final failure of the specimens due to compression (right)

3.3.6 Freeze-Thaw

Freeze-thaw testing for this research was performed on two uncracked and two cracked 3-in. by 3-in. by 12-in. prisms with HE-1% and HE-2% fibers in accordance with ASTM C666 [72]. The prisms were cured in a water bath until maturity (minimum 60 days), then dried to remove excess water by wiping the surfaces with cloth or air-drying for 30 minutes to 1 hour and weighed. The cracked specimens were loaded using the same methods as the MOR test. However, the loading was continued only until the first load drop was observed, indicative of first cracks. Figure 11 shows the induced cracks in one specimen for each fiber content. The cracks generated in the HE-1% specimens were more visible than the cracks generated in HE-2% specimens.

Figure 11. Hairline crack generated in Freeze-Thaw specimens after loading till first load drop for an HE-1% specimen (left) and HE-2% specimen (right)

Baseline longitudinal resonant frequency of the prisms was then measured using a James Instruments E-Meter (Figure 12). Measurements were taken for the cracked specimens immediately after loading and for uncracked specimens immediately after drying. Initial specimen dimensions were measured before the specimens were placed in the freeze-thaw chamber (Figure 13). Care was taken to ensure that the specimens were covered with at least 1/8 in. of water on all sides. Frequency and dimensional measurements were repeated every 36 or fewer cycles as specified in ASTM C666. At each measurement increment, the specimens were kept overnight in the freeze-thaw machine submerged in water to bring the specimens to room temperature before measurements were taken. After measurements were taken the specimens were returned to the freeze-thaw machine and were moved one cell to the right after each measurement increment to ensure all specimens experienced the same average conditions. The total number of cycles for the test was adjusted from the specified 300 in ASTM C666 [72] to 350 due to the higher durability of UHPC.

Figure 12. E-Meter device used to generate resonant frequency (left) and test setup to measure resonant frequency of the freeze-thaw specimens (right).

Figure 13. Specimens placed in the freeze-thaw chamber

3.3.7 Prestressed Girder Repair to Restore Shear Strength

3.3.7.1 Prestressed Girder Design and Construction

An 18 ft long approximately half-scale AASHTO Type II prestressed girder was constructed for this work using self-consolidating concrete for the girder and Oklahoma Department of Transportation (ODOT) class AA bridge deck concrete for the composite deck. The beam was constructed as part of previous research work done at the University of Oklahoma by Ahmadi [64]. Figure 14 depicts the beam cross section and reinforcement details of the prestressed girder. The two ½ in. special (0.52 in.) prestressing strands were stressed to 75% of the 270 ksi ultimate strength plus approximately 1.5% extra to count for minor anchor slip. The prestress release was done 24 hours after casting when the concrete compressive strength reached more than 4000 psi. The deck was cast 28 days after girder construction.

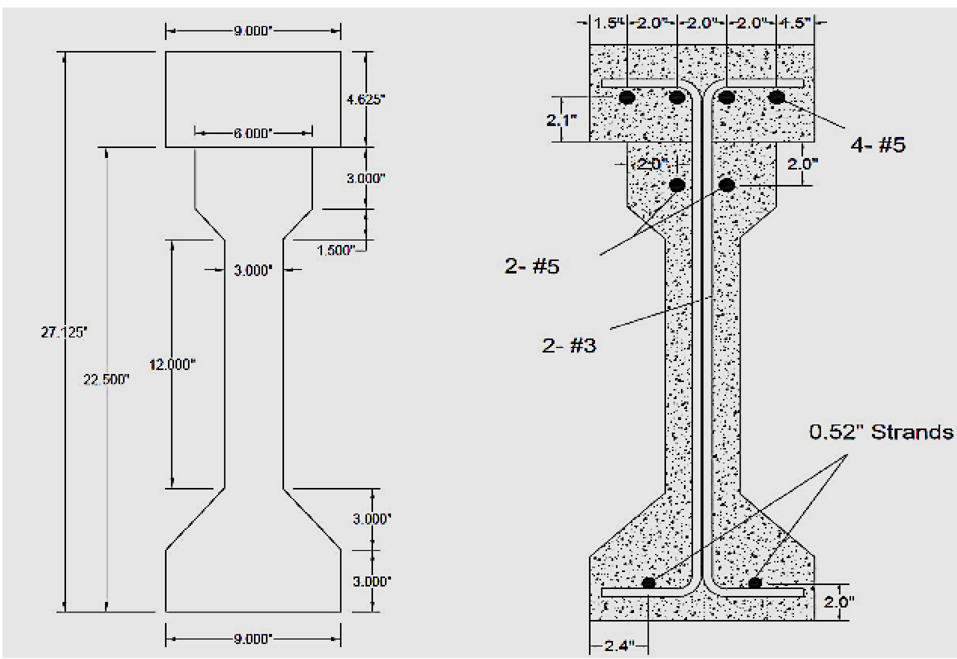

Figure 14. Prestressed girder cross-section (left) and reinforcement details (right) [64]

3.3.7.2 Testing of Undamaged and Repaired Girder

The tests of the girder before and after repair were conducted in similar fashion following the test setup presented by Ahmadi [64] and depicted in Figure 15. The beam was placed on 6 in. wide neoprene bearing pads to create a 17 ft – 4.5 in. span center to center of bearing. A single point load was applied 3.5 ft from the beam end using a hydraulic actuator until the beam was no longer capable to sustaining additional load. Applied load was measured using a 100 kips capacity load cell, four LVDTs were attached to the exposed strand portions (two at each end) to measure strand slip, and two wire potentiometers were placed at the loading position to measure vertical deflection. The load was applied in 5 kips increments until the first crack was observed and in 2 kips increments after initial cracking. After each load increment cracks were marked, and deflection was measured manually to match with the data from wire potentiometers.

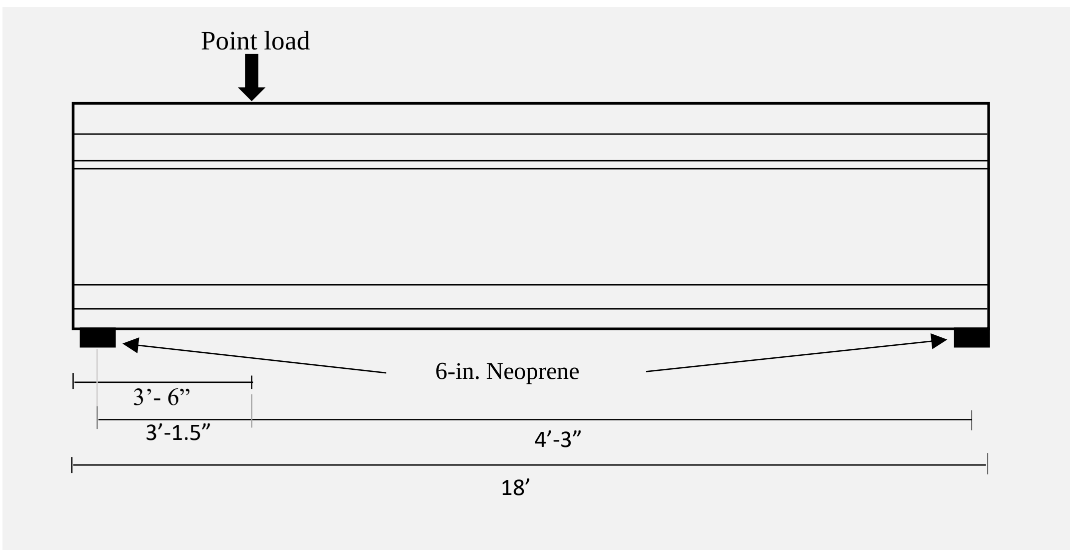

Figure 15. Test setup and location of point load for undamaged and repaired beams.

3.3.7.3 Repair Procedure of Damaged Girder

The section between the beam end and the point load damaged during the initial test was encapsulated using the ST-2% J3 UHPC mix following the procedure reported by Ahmadi [64]. The surface of the girder was roughened using an angle grinder and sand blaster throughout the 3.5 ft repair length and a total of eighteen ¼ in. diameter by 3-1/4 in. long concrete screws were distributed on both sides in an alternative pattern to act as shear studs between original and repair material. The interface shear transfer provision of AASHTO LRFD (2017) [76] Section 5.7.4.3 and concrete shear friction were used with the manufacturer specified shear capacity of the screws to calculate the required number and spacing of the screws. The screws were inserted roughly 1-3/4 in. into the existing concrete. The arrangement of the screws is presented in Figure 16.

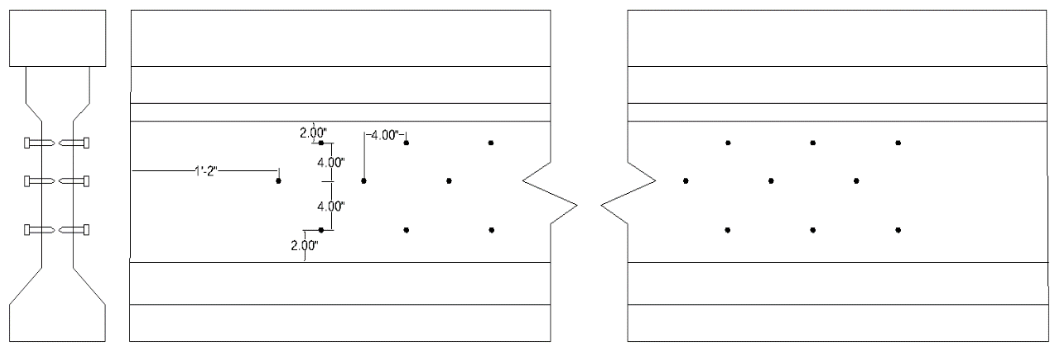

Figure 16. Distribution of shear screws to repair the damaged section of the beam

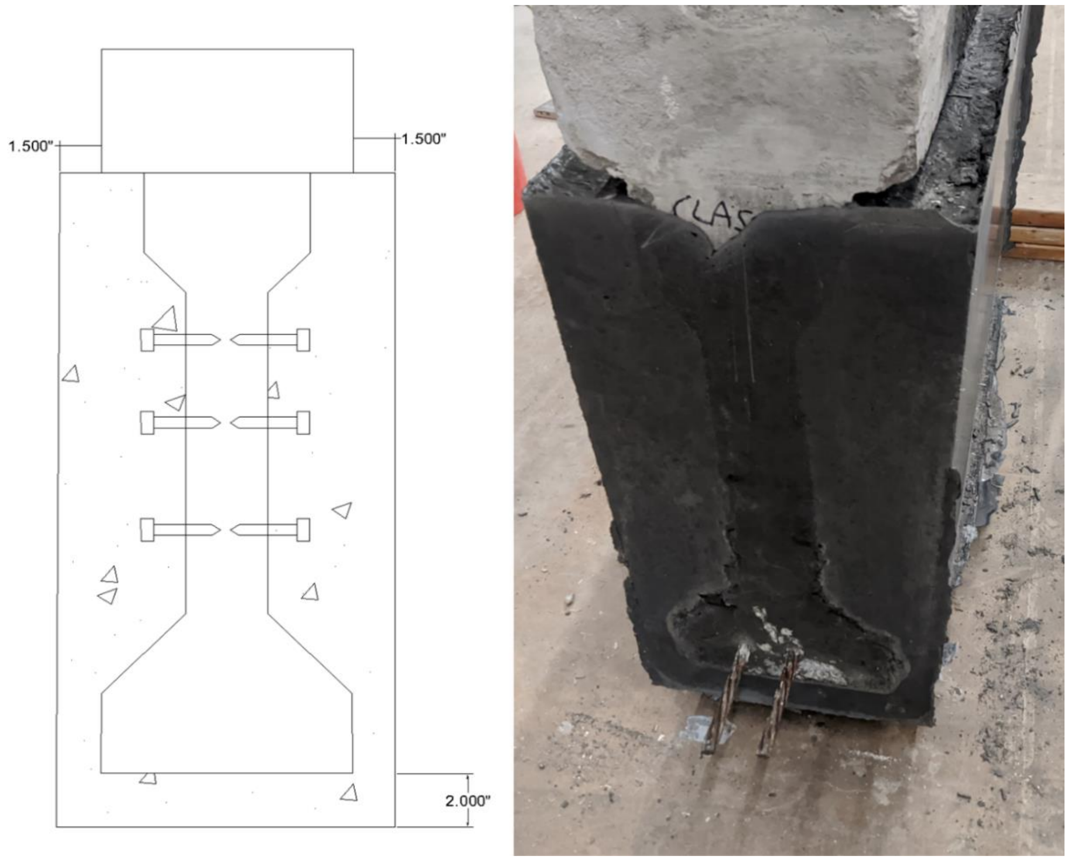

Figure 17. Repaired dimension of the beam (left), repaired section of the beam using ST-2% (right).

A strut and tie model was used to determine the force that needed to be transferred between the beam and repair using shear studs and 1.5 in. thickness was chosen to calculate the capacity using shear calculation by Ahmadi [64]. The repair dimensions and the repaired surface are presented in Figure 17. The damaged portion of the deck below the load point was also removed and repaired using rapid setting belitic calcium sulfoaluminate cement concrete (Figure 18), which was not done in the work by Ahmadi [64].

Figure 18. Repaired deck section using belitic calcium sulfoaluminate cement.

Chapter 4 Results and Discussions

4.1 Flowability

This section describes the flow results measured immediately after the completion of mixing the J3 concrete. The targeted flow for each mix was between 8 in. and 10 in. As the w/cm ratio was fixed, high-range water reducer (HRWR) amount was adjusted to ensure proper flowability with changing fiber content.

Though HRWR can increase flowability of the concrete, it also impedes the initial set and strength gaining process. As adding HRWR introduced air and extra water to the mix, care was taken while increasing HRWR dosage, as it could cause segregation of the mix components. For these reasons the maximum HRWR amount used in this experimental program was limited to 35 oz/cwt.

Table 6 presents the flows and associated HRWR with J3 mixes with both straight (ST) and hooked-end (HE) fibers. Though fiber volume fraction and fiber type were the major factors affecting flowability of the mixes, surrounding temperature was also a substantial factor. Lowering the temperature of the dry materials and using cold mixing water were two other steps used to lower the HRWR demand. The dry ingredients also played an important role the flowability of the mixes. The source and general properties of all the constituent materials (Table 1) were consistent throughout testing. However, as the supplementary cementitious materials were mostly byproducts, changing from barrel to barrel introduced some inconsistencies in the flows and HRWR demands. Table 6 presents the flows and associated HRWR with J3 mixes with both straight and hooked-end fibers.

Table 6. Flows and HRWR demands of the J3 mixes with straight and hooked-end fibers.

Fiber Type	Volume Fraction (%)	HRWR oz./cwt	Flow in.
ST	1	32.5	10.0
	2	25.0	9.75
	4	30.3	7.0
	6	34.7	4.5
HE	1	33.8	10.0
	2	33.4	8.5
	4	35.3	6.5

Figure 19 and Figure 20 present the observed flows for thee J3 mixes with ST and HE fibers. The ST-1%, ST-2% and HE-1% mixes showed homogenous mixes that evenly spread out the flow table plate. As the HE-1% mix required a higher dosage of HRWR, air bubbles were observed during the flow test which are visible in Figure 20. Although the fiber volume was the same for the ST-2% and HE-2% mixes, the HE-2% mix was not homogenous even though the HRWR dosage was increased. This was because of the nature of the hooked-end fibers. The hooked-end fibers were clumped together in the middle and the mortar flowed out for HE-2%. This also caused fibers settling at the bottom of the specimen molds. Clumping of fibers in the middle of the flow was also visible for the ST-4%, ST-6% and HE-4% mixes because of the extremely higher number of fibers. Though the ST-4% and HE-4% mixes showed some amount of flowability, the ST-6% mix did not show any flow of the concrete mortar. This clumping of fibers caused problems while placing concrete in the molds, particularly for the direct tensile test specimens. A vibration table was used to help consolidate the ST-4%, ST-6%, and HE-4% specimens. However, fibers settled to the bottom of many specimens which made it difficult to get even properties both at the cast surface and bottom surface.

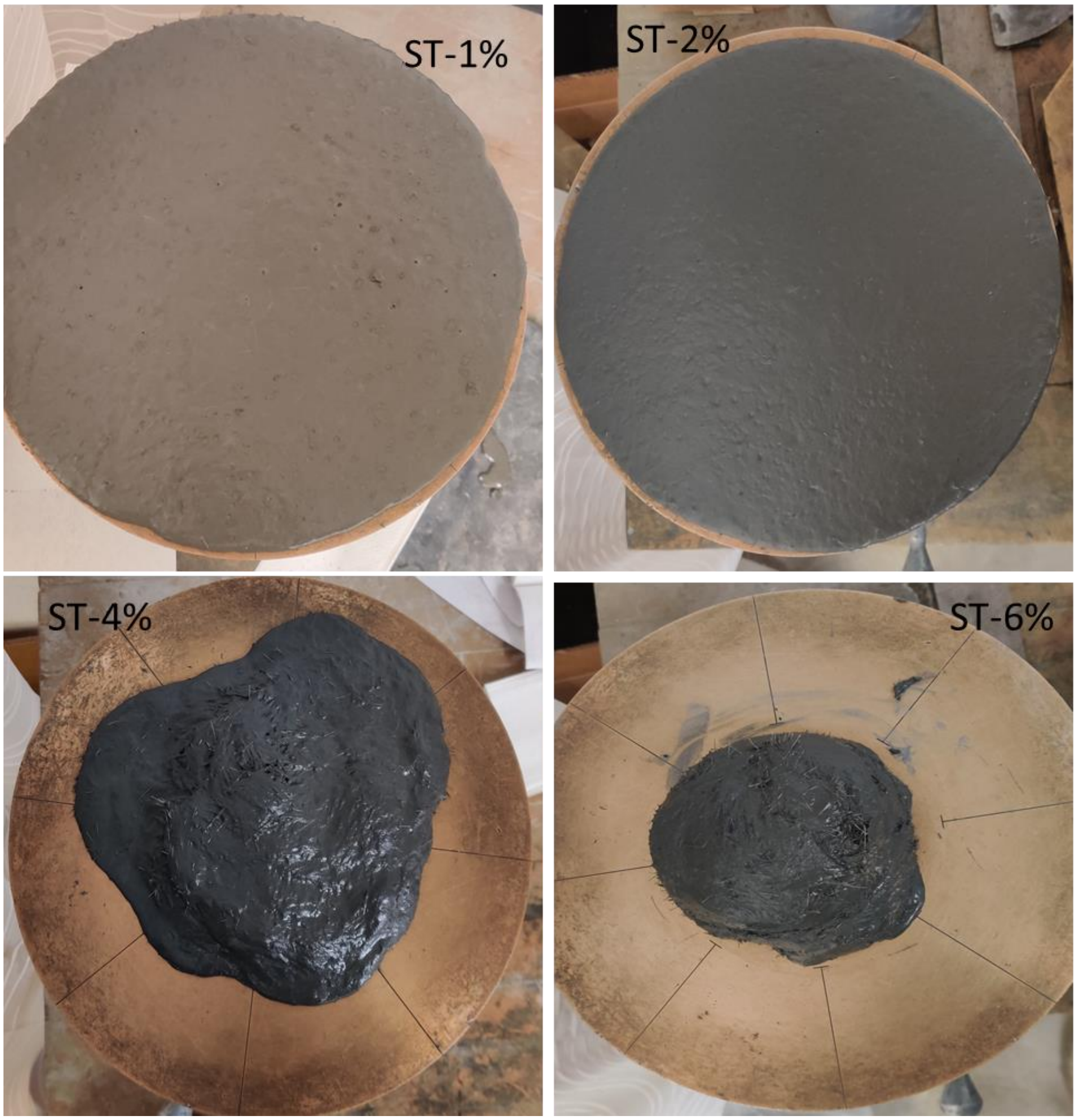

Figure 19. Flows of J3 mixes with ST fibers.

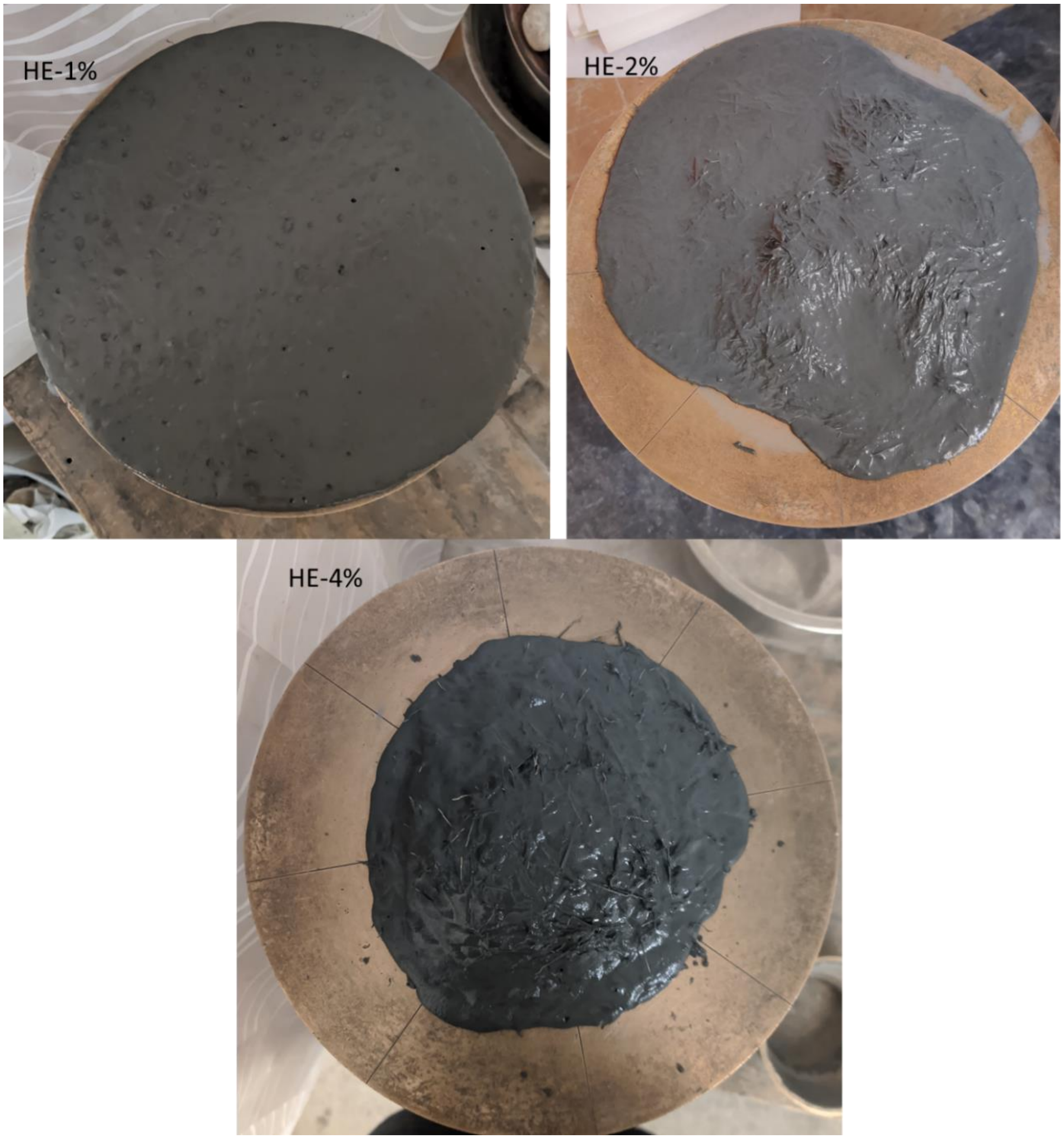

Figure 20. Flows of J3 mixes with HE fibers.

4.2 Compressive Response

This section provides a summary of compressive strength and elasticity modulus for J3 concrete having various fiber volume fractions of both ST and HE fibers.

4.2.1 Failure Pattern

Fibers in UHPC turn an extreme brittle failure under compression into a more ductile failure by preventing fragmentation of the specimens, which was observed throughout this research. The typical failure patterns observed in J3 cylindrical specimens with various volume fraction of ST microfibers are presented in Figure 21. The ST-1% and ST-2% specimens showed vertical splitting failure, while the ST-4% and ST-6% specimens tried to split diagonally. The ST-4% and ST-6% specimens generated higher numbers of cracks compared to the ST-1% and ST-2% specimens because of higher number of fibers bridging the cracks. Also, localization of failure was observed in ST-1% and ST-2% specimens which led to widening of the cracks and the specimens almost splitting into halves, whereas ST-4% and ST-6% specimens tried to bulge due to significant fiber bridging.

Figure 22 presents the failure patterns of the J3 cylindrical specimens with HE fibers. A mixture of diagonal and vertical splitting during failure was observed in the HE-1% and HE-2% specimens. The HE-1% and HE-2% specimens showed significantly less localization and widening of cracks compared to the ST-1% and ST-2% specimens because of the superior bonding strength of hooked-end fibers with the concrete matrix. In return the HE-1% and HE-2% specimens exhibited higher damage to the concrete where the cracks were spanned by fibers. The HE-4% specimens showed a significantly higher number of distributed cracks compared to the ST-4% specimens and generated small chunks of broken concrete from the surface.

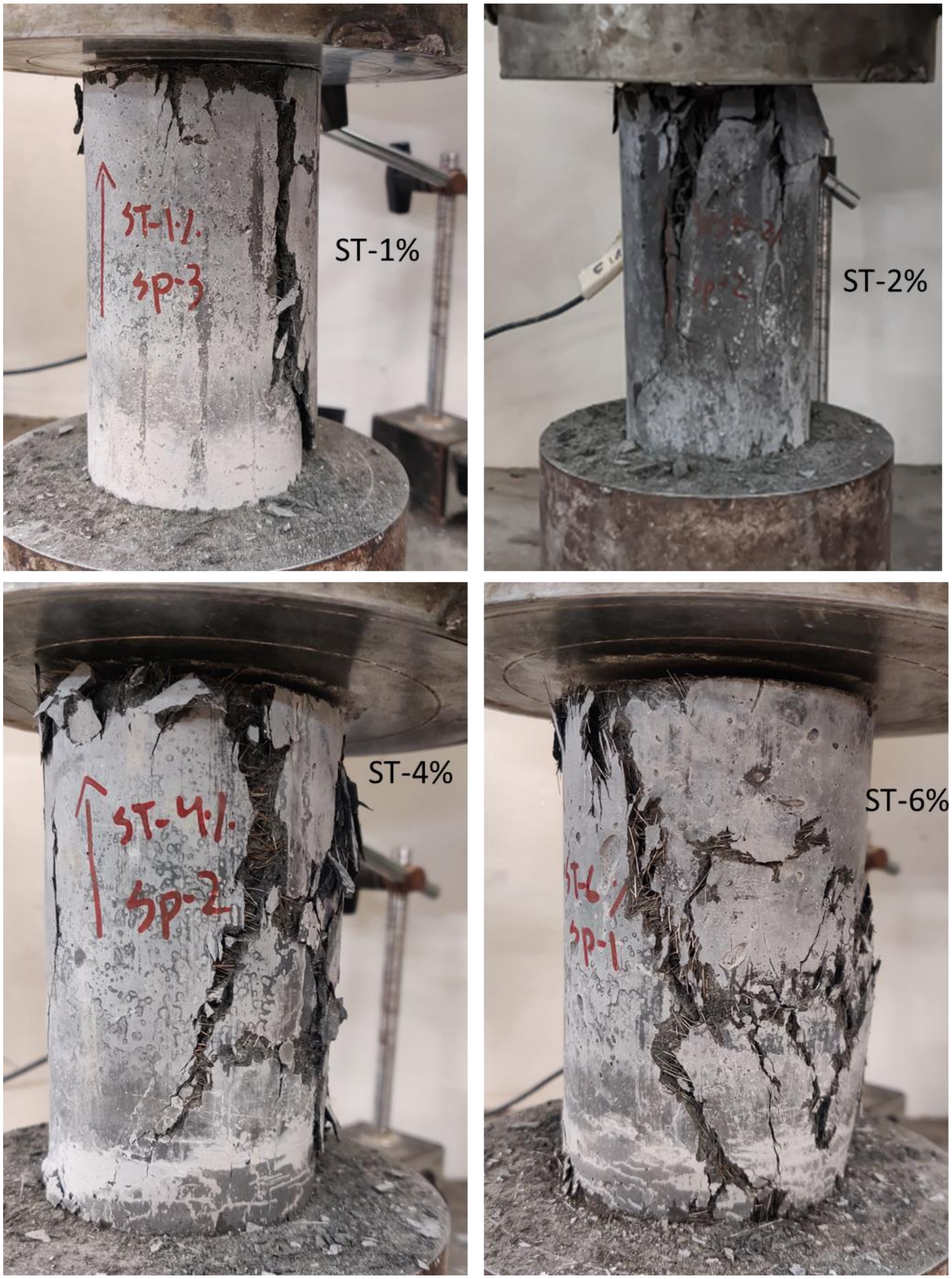

Figure 21. Failure pattern of J3 cylindrical specimens with straight microfibers under axial compressive load.

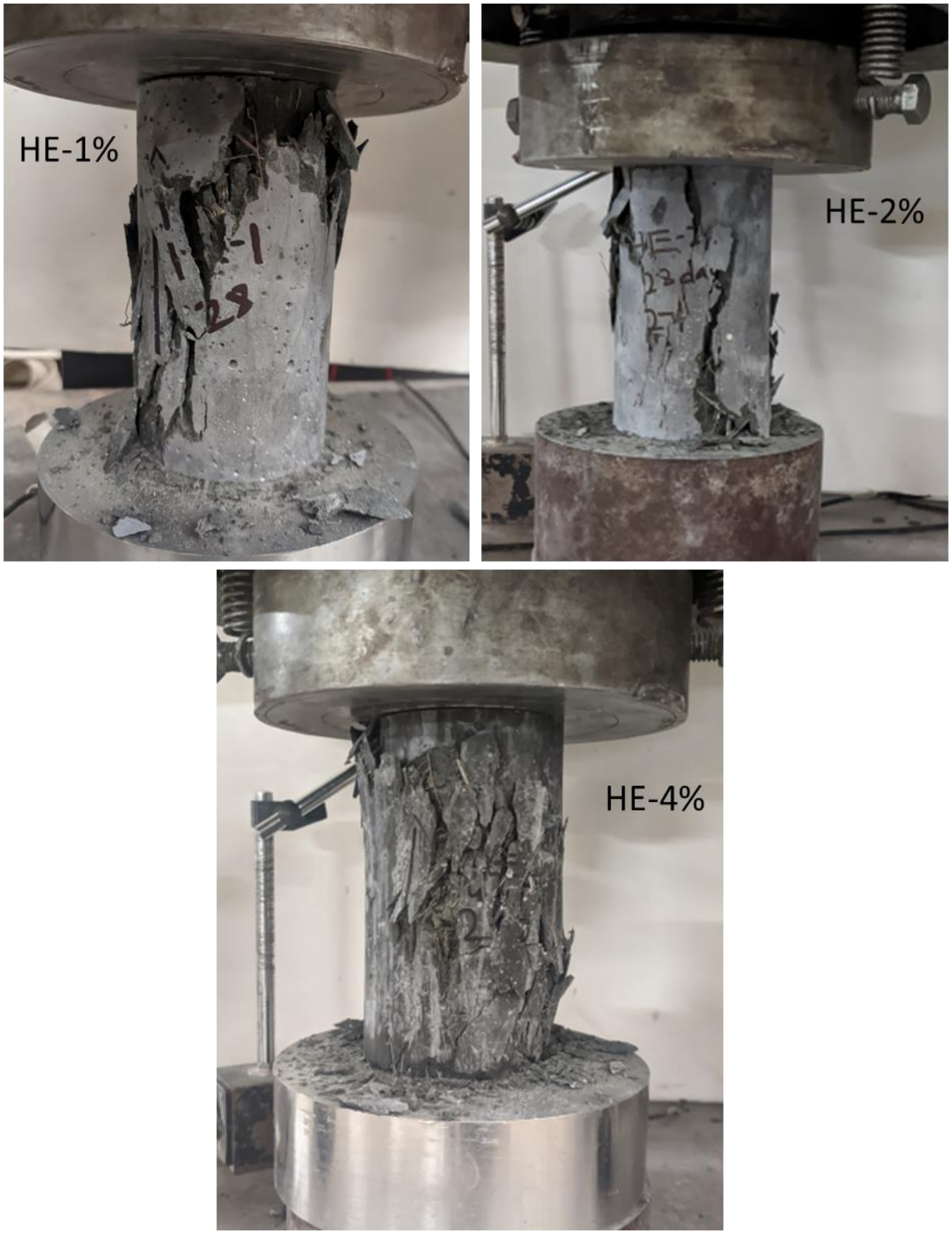

Figure 22. Failure pattern of J3 cylindrical specimens with hooked-end fibers under axial compressive load.

4.2.2 Compressive Strength

Figure 23 presents the average compressive strengths of three 3-in. cylindrical specimens for J3 concrete with both ST microfibers and HE fibers. All the mixes with HE and ST fibers, except mix ST-4%, showed an increase in compressive strength with age. No strength gain was observed between 28 and 56 days strength for the ST-4% specimens. Though the ST-4% mix had a 7 in. flow, improper fiber distribution due to fiber clumping and fast loss of flowability due to high surrounding temperature could be the reasons for ST-4% specimens not gaining strength beyond 16 ksi. Compressive strength of 2 in. by 2 in. cubes made from a small mix of the ST-4% mix were 12 ksi, 15.4 ksi and 19.5 ksi for 3, 28 and 56 days of age, respectively, which indicates that with proper casting the ST-4% specimens would also be able to show increase in strength with age.

The J3 mixes with ST showed no noticeable increase in compressive strength with higher volume of fibers. Ignoring 56 days strength of mix ST-4%, all the average strengths at 3, 28 and 56 days ages for 1%, 2%, 4% and 6% volume fractions were within a 1.3 ksi strength range, which indicates that additional straight fiber amounts had no positive impact on the compressive strength of specimens.

However, mixes with hooked-end fibers showed a decrease in compressive strength with increasing fiber volume fractions at 3, 28 and 56 days ages beyond 2%. The HE-1% and HE-2% mixes showed similar results with a difference around 1 ksi. Significant difficulties were encountered for obtaining a homogenous mix for HE 4%, which impacted the compressive strength of specimens with higher fiber contents.

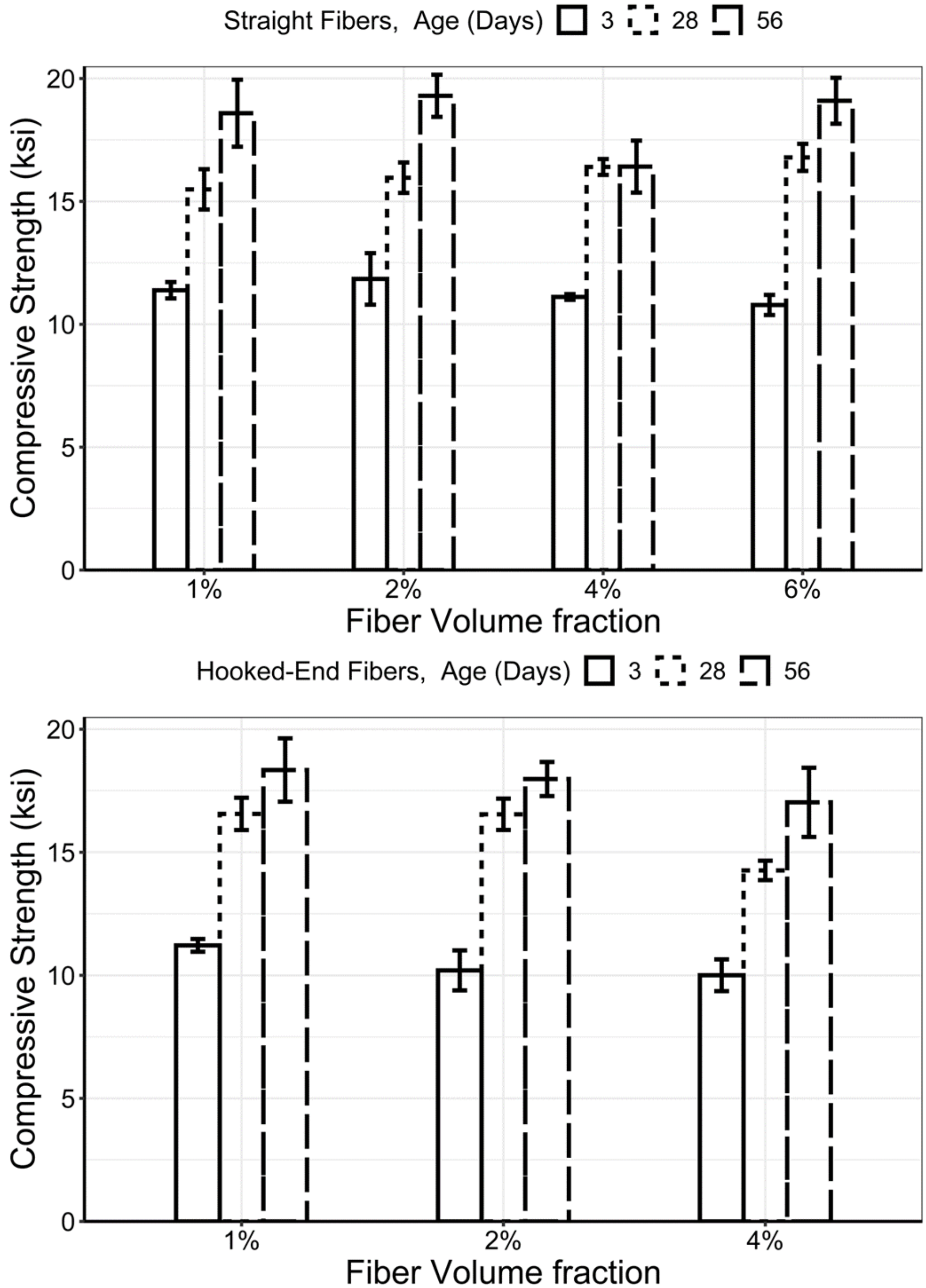

Figure 23. Compressive strength of J3 specimens at various ages with varying fiber volume fraction of ST micro-fibers (top) and HE fibers (bottom).

4.2.3 Stress-Strain Behavior

Figure 24 presents the typical pre-crack response of J3 specimens measured using strain gauges on specimens which had 1% volume fraction of HE fibers. Two of the specimens, mounted with three strain gauges each, showed almost linear behavior until a strain value of 0.0033 in./in., when the specimens reached peak load and formed cracks. However, the strain gauges were not able to measure the behavior of J3 cylindrical specimens after reaching peak load. After reaching the peak-load a sudden significant load drop was observed for all the specimens, which was not captured by the strain gauges as the stress release of the specimens by forming cracks rendered the strain gauges ineffective.

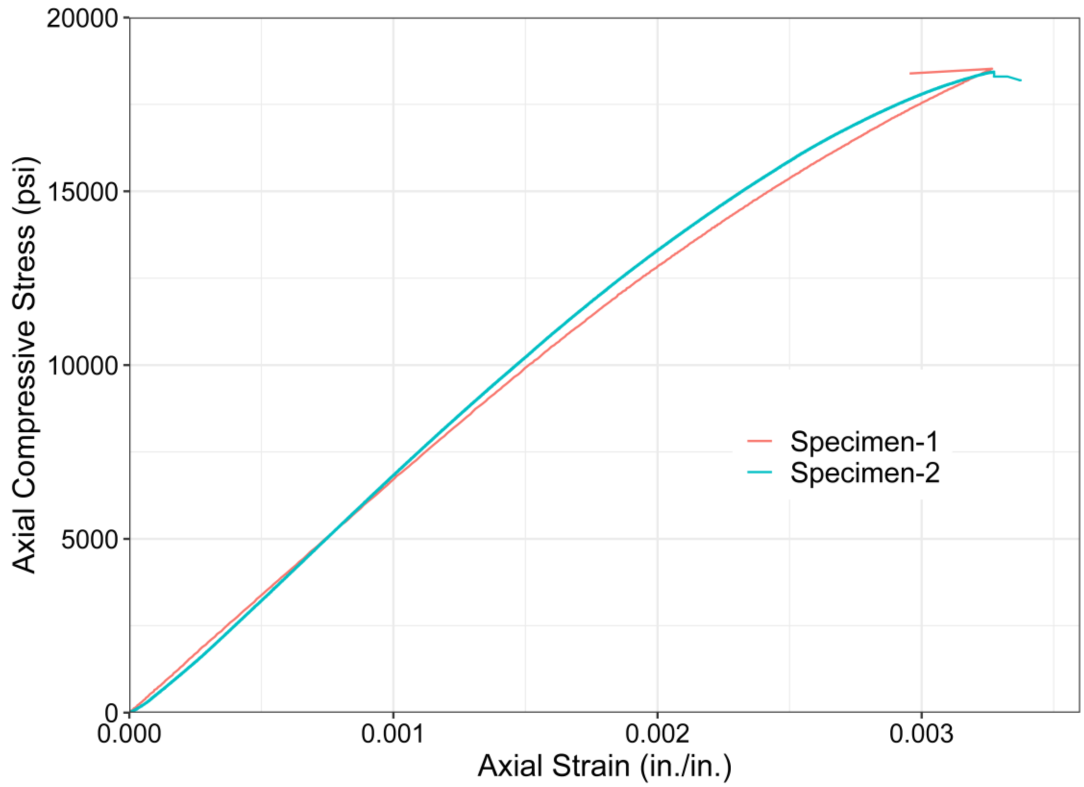

Figure 24. Typical stress-strain behavior of J3 concrete before peak-stress.

After the sudden load drop the specimen tried to sustain loads and showed a progressive strain softening behavior. As the strain gauges were not able to capture the general stress-strain behavior after the first crack, an attempt was made to measure the response using LVDTs as presented in section 3.3.2 and shown in Figure 6. The axial strain was measured using the whole gauge length between the LVDTs, which represented the average strain over the whole gauge length rather than actual strain values. However, due to equipment constraints and having different filler plates capable of deforming and moving, the generated response curves could not identify the real strain values.

Figure 25 presents the approximate shapes of the axial stress-strain curves for J3 cylindrical specimens with straight microfibers. After peak-stress, sudden drop in stress occurred until second peak-stress, which marked the beginning of large deformation. The second peak-stress and subsequent stress bearing capacity was dependent on the fiber amount as the crack bridging started from that point. Second peak-load marked the beginning of gradual strain-softening behavior and the specimen started showing larger deformations after that.

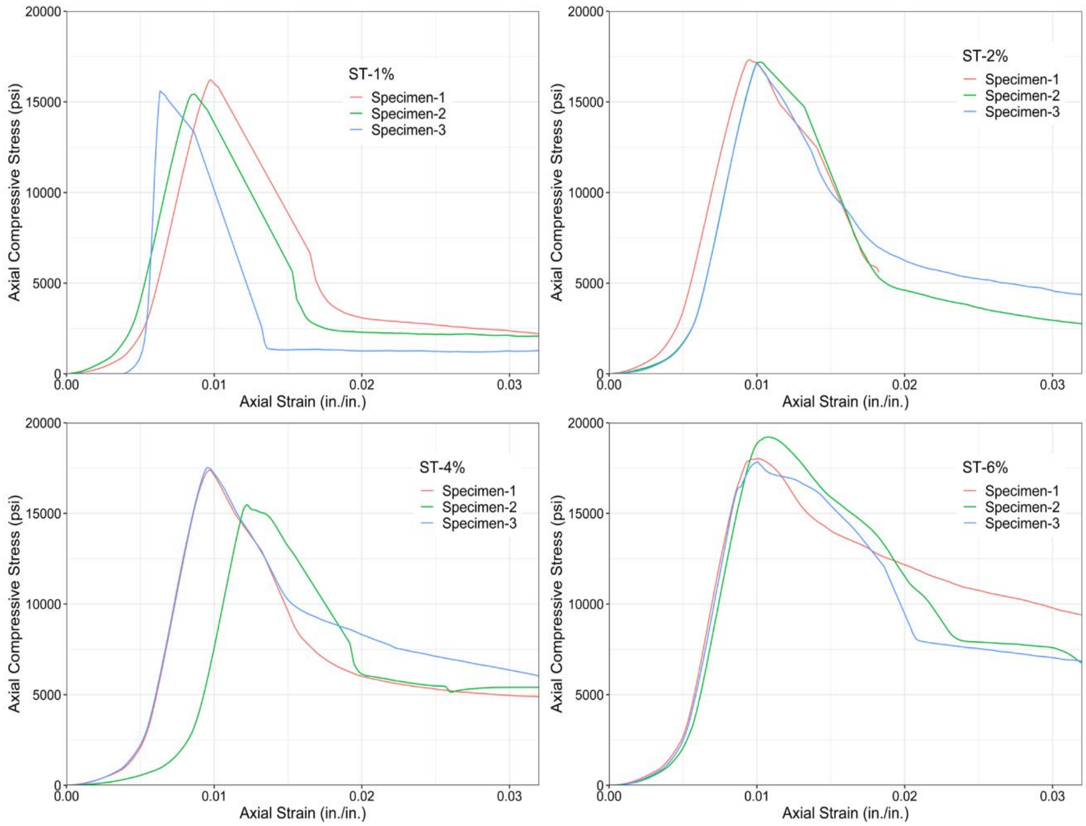

Figure 25. Approximate stress-strain curves for cylinders with ST microfibers under uniaxial compression.

However, the curves were able to show the approximate stress behavior after first cracks of the specimens and could be used for comparison purposes. A concave portion was observed for each specimen at the start of the stress-strain curve. This was due to specimens engaging and could be corrected by extending the linear-elastic portion of the curve backward as Figure 26.

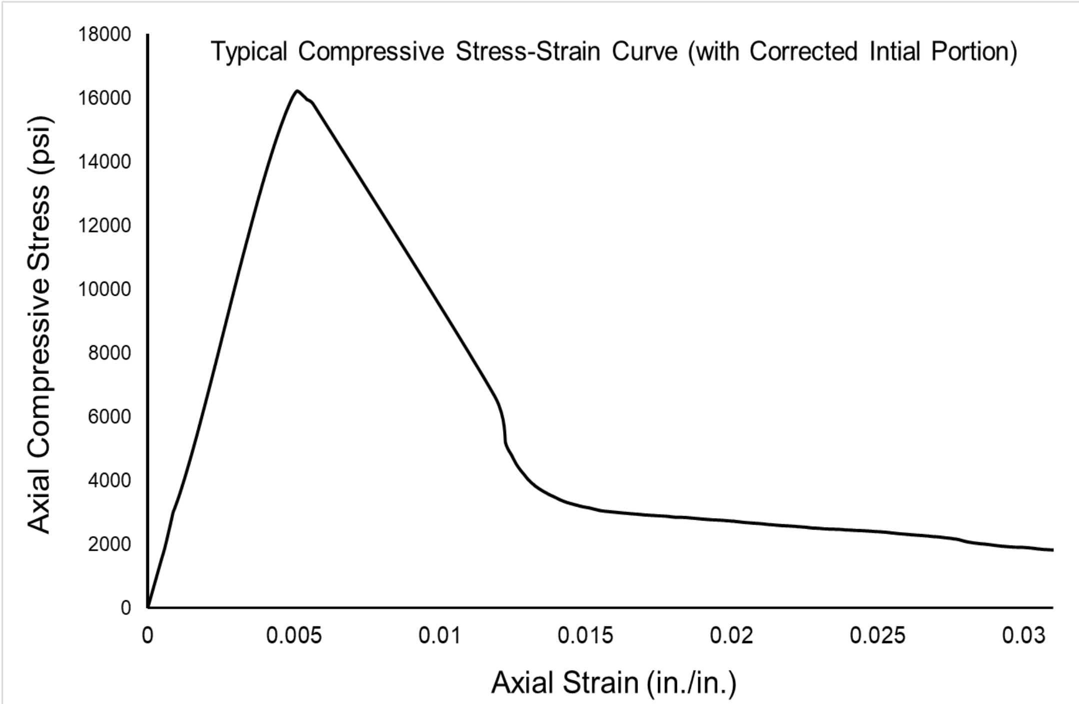

Figure 26. Typical compressive stress-strain curve after considering and correcting initial concave portion due to specimen engaging.

Figure 27 presents the approximate shapes of the axial stress-strain curves for J3 cylindrical specimens with HE fibers. Due to an error at recording, data for HE-1% one specimen were lost and considering the likelihood of higher variability one extra specimen for HE-4% was tested. Specimens showed similar post-cracking behavior to the ST microfiber specimens. Second peak-stress started the strain-softening behavior, and the descending portion was dependent on fiber volume fraction.

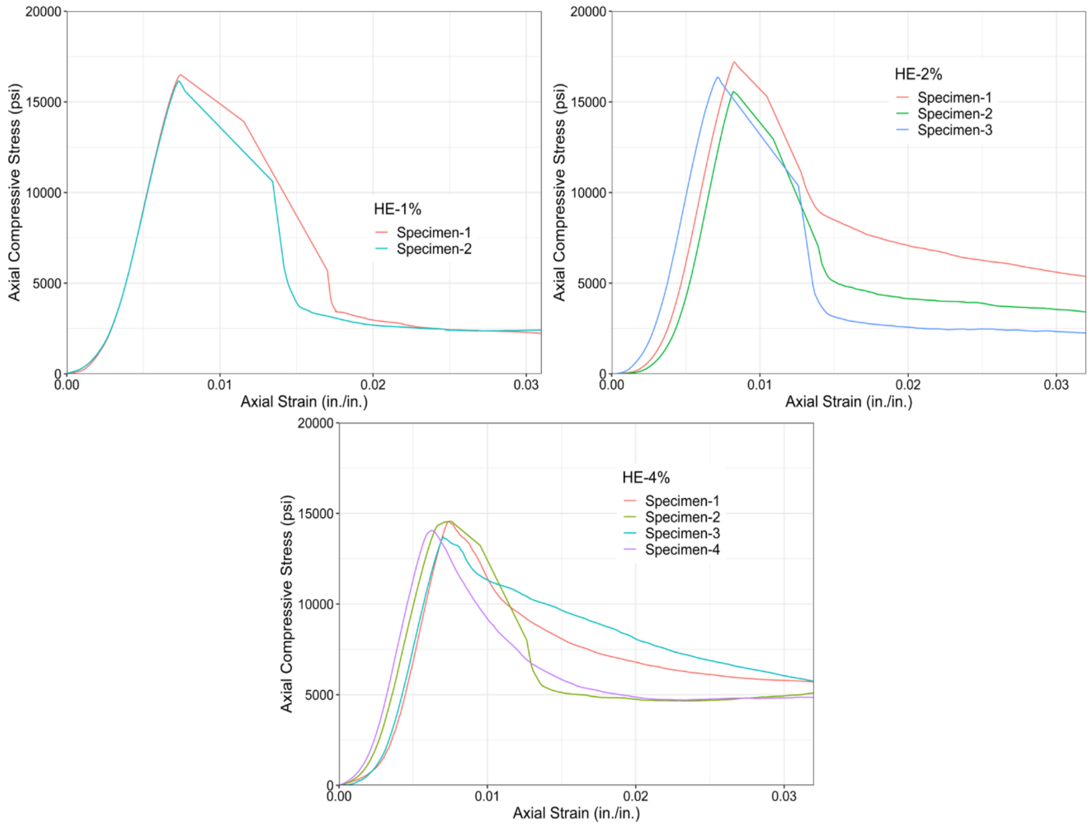

Figure 27. Approximate stress-strain curve for cylinders with hooked-end fibers under uniaxial compression.

4.2.4 Elasticity Modulus

Figure 28 presents the average elasticity modulus of three 4 in. by 8 in. cylinders made with J3 concrete having ST and HE fibers. All the mixes showed almost identical elasticity modulus. As the elasticity modulus represents the linear portion of compressive stress-strain behavior of concrete, aggregate and cementitious volume fraction dominate the elasticity modulus [1], [77]. However, a significantly high portion of fibers crossing certain portions of specimens can contribute to the stiffness of the specimens. Also, steel being stiffer than concrete can favor the specimens with high number of steel fibers. This could be the reason why the HE-4% and ST-6% specimens showed a minor increase in elasticity modulus relative to the specimens with other volume fractions.

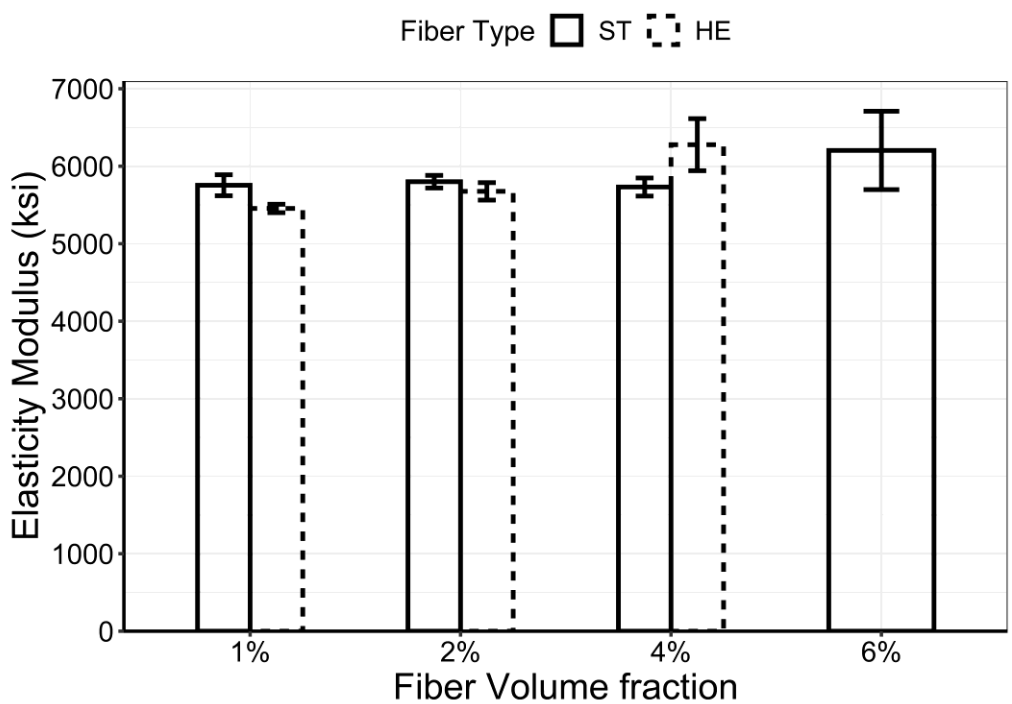

Figure 28. Elasticity modulus of J3 concrete with different fiber types.

4.3 Flexural Strength/Modulus of Rupture (MOR)

4.3.1 Specimens with Straight Fibers at 28 days age

4.3.1.1 Crack Pattern

Figure 29 - Figure 32 show the crack patterns of the specimens with straight fibers (ST) after the MOR tests at 28 days. The specimens developed hairline cracks in the middle third region at the point of first cracking. After the first crack, the fibers started bridging the crack(s) and transferring loads, which allowed more hairline cracks to develop rather than widening of the single crack. However, after a certain load, crack localization started, and one wide crack formed. At the ultimate state, the fibers were pulled out of the matrix. It can be observed from Figure 29-Figure 32 that the major cracks occurred in the middle third zone, though ST-1-1 exhibited a minor crack outside the middle third but inside the 5% of the span length specified as acceptable by ASTM C78 [70]. The fibers carrying load by bridging cracks resulted in a non-uniform crack pattern. The ST-1% and ST-2% specimens showed relatively linear cracks, however, ST-4% and ST-6% specimens showed more uneven cracks because of higher fiber density. Though six specimens were cast for the ST-4% mix to test on 28 days and 56 days, due to instrumentation issue, only two specimens were able to be tested at 28 days and the remaining four specimens were tested at 56 days.

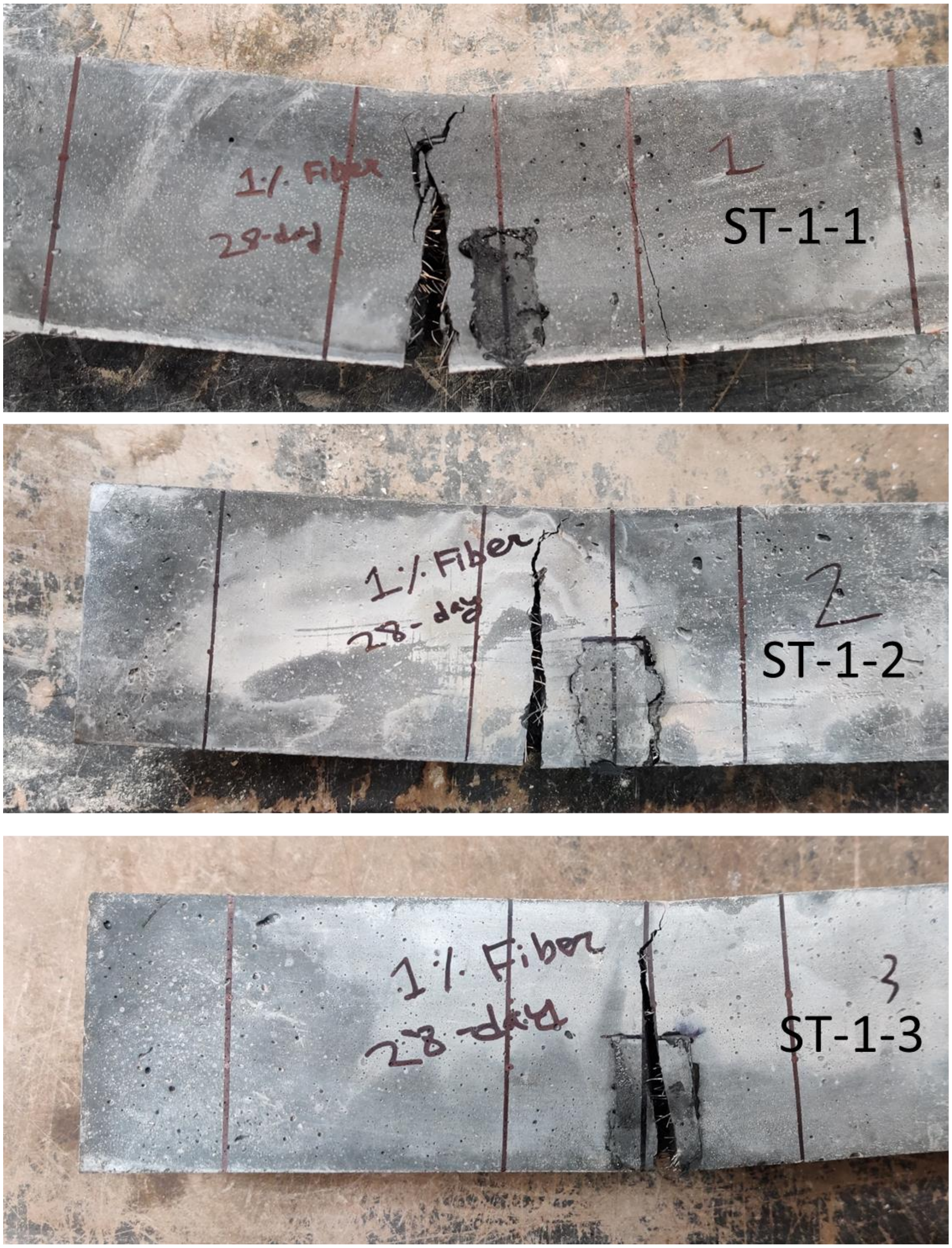

Figure 29. Crack pattern of ST-1% MOR specimens at 28 days.

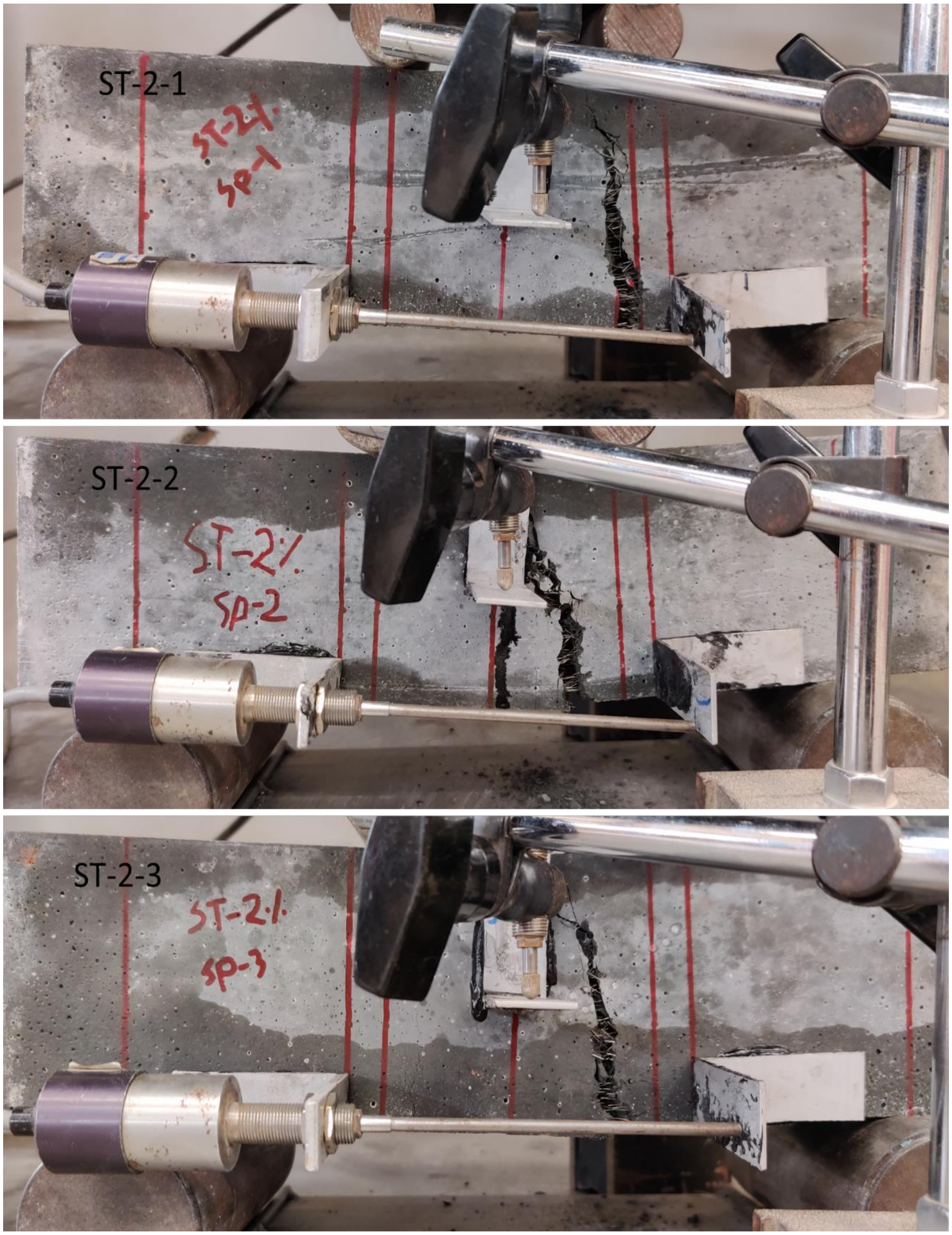

Figure 30. Crack pattern of ST-2% MOR specimens at 28 days.

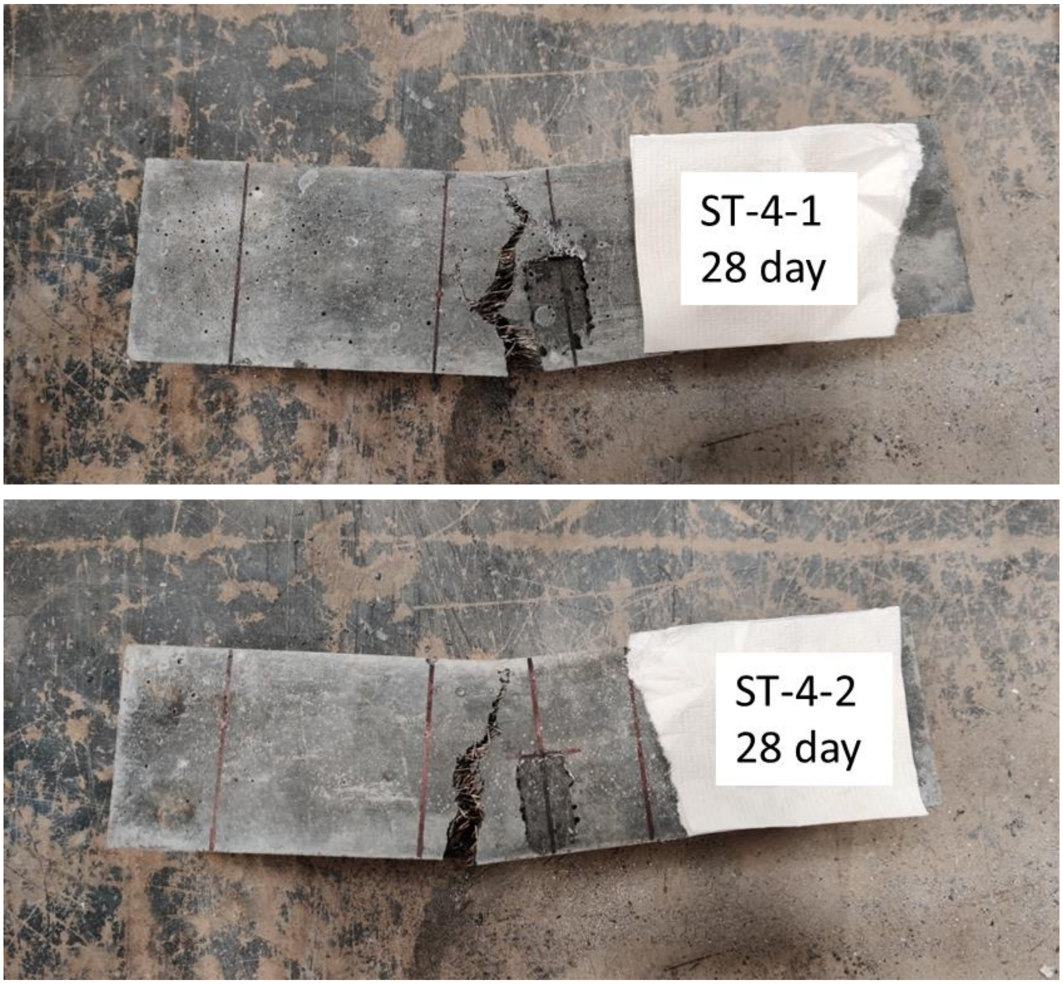

Figure 31. Crack pattern of ST-4% MOR specimens at 28 days.

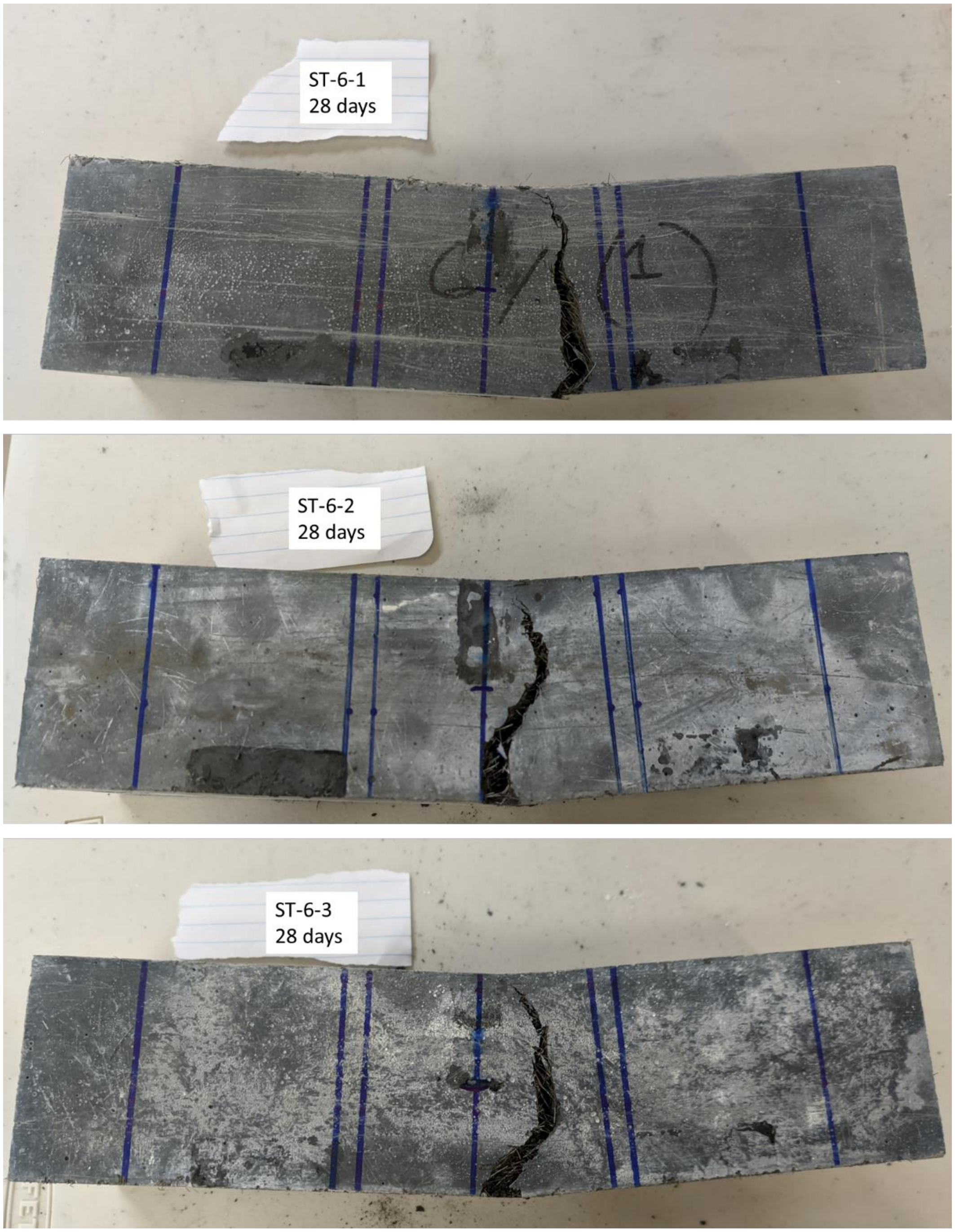

Figure 32. Crack pattern of ST-6% MOR specimens at 28 days.

4.3.1.2 Flexural Behavior

Figure 33 presents the load-deflection graphs for the bending tests of straight fiber (ST) specimens at 28 days. All the specimens showed three distinctive stages in load deflection behavior; a linear-elastic behavior in the uncracked state, fiber activation state, where fibers bridged cracks and carried load, and fiber pull-out state, which started after reaching the maximum post first crack loads. Fiber bridging and multiple crack creation occurred in the fiber activation stage and at the fiber pull-out stage widening of cracks and matrix softening occurred.

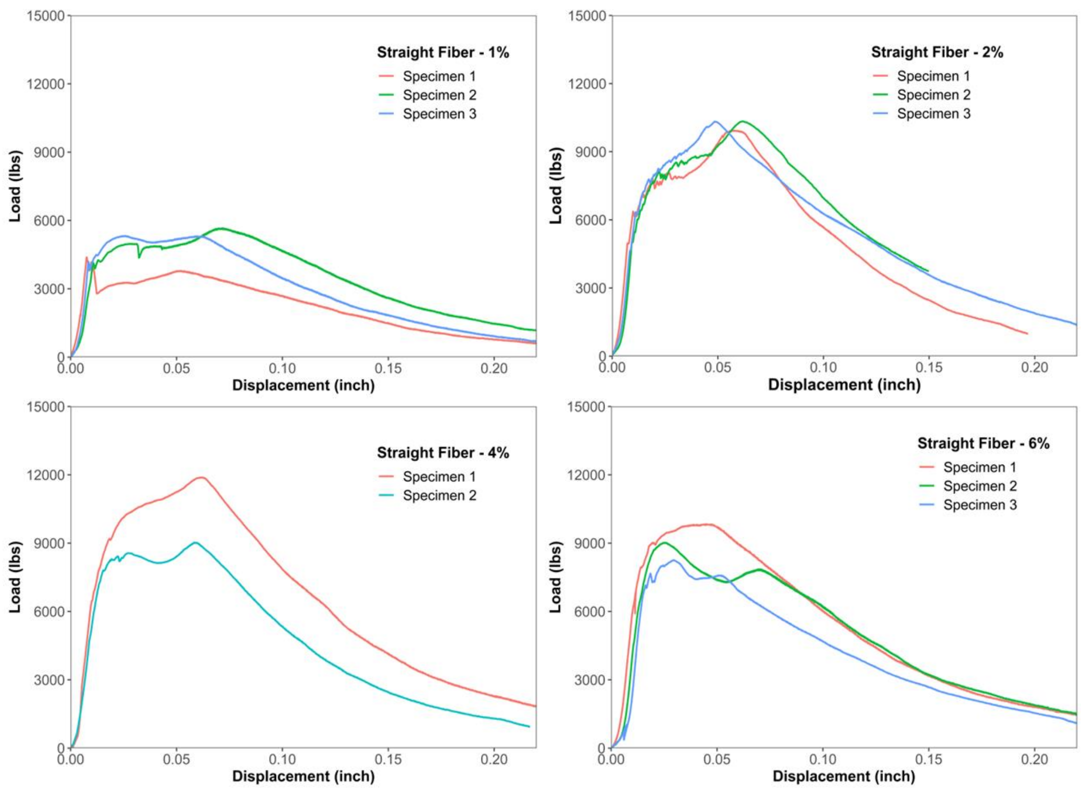

Figure 33. Load - deflection graphs for all straight fiber volumes at 28 days.

The performance of the J3 specimens with ST fibers can be evaluated by observing first-cracking flexural strength (f_{LOP}), post-cracking flexural strength (f_{MOR}), and deflection and toughness/load absorption capacity (area under load-deflection curve). The first point to change the stiffness or the point where the slope in the load-deflection graph changed was used to calculate the limit of proportionality (LOP) of the specimen as defined by previous researchers [29], [44]. Modulus of rupture (MOR) was defined by the post-cracking peak load point. For all specimens expect ST-1-1 and ST-6-2, distinctive deflection-hardening behavior ($f_{MOR} > f_{LOP}$) resulting in higher strength after the first crack can be observed, which is a prominent feature of UHPC as shown by previous researchers [30], [31]. Specimens ST-1-1 and ST-6-2 showed deflection-softening behavior ($f_{MOR} < f_{LOP}$).

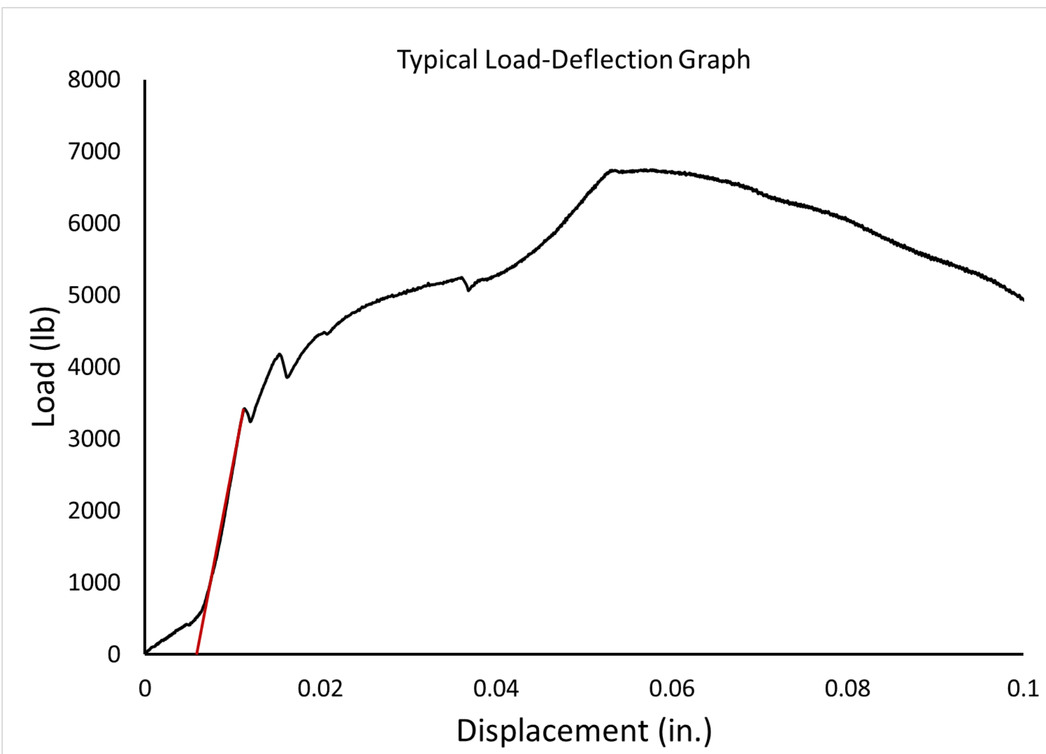

Figure 34. Typical load-deflection graphs for the flexural test.

Figure 34 shows a typical curve that was observed from the flexural tests with both HE and ST specimens. All the specimens were subjected to small deflection, which was around 0.004 in. at the start of the test. This was due to settlement of the rollers placed underneath the specimen and breaking of small concrete chips where the top load plate and bottom rollers touched the specimens because fibers made it difficult to get an even surface. This extra deflection induced by external factors was subtracted from each specimen to get actual linear-elastic behavior in the load-deflection curve and properly identify deflections at LOP and MOR.

Figure 35 summarizes the effect of straight fibers on strength and deflection capacity of specimens at 28 days with mean and first standard deviation. As the placement of materials in forms was random and care was taken to facilitate randomness in the fiber orientation, variations can be seen in the results. The first crack point mostly depends on specimen stiffness rather than on the fiber volume and type. The average deflections at the first-cracking point (δ_{LOP}) are around 0.006 in. to 0.007 in. and the deflection values for specimens with different fiber volumes overlap indicating no trend with fiber volume. Figure 35 shows similar f_{LOP} for all fiber volume fractions, which further confirms the claim that fiber volume has no impact of the first-cracking properties of ST specimen tested at 28 days. The average deflections at post-cracking peak load (δ_{MOR}) are also nearly identical (significant overlap of the standard deviation), between 0.047 in. and 0.058 in. for ST-1%, ST-2% and ST-4%, which can be related to effective length of the fiber except for ST-6%. After reaching that deflection, the fibers do not have enough length to further develop enough grip to continue load bearing. This leads to softening of the concrete matrix and continuous decreases in load carrying capacity. However, relatively higher stiffness and improper fiber distribution might be reasons the ST-6% specimens reached peak deflection earlier. Figure 35 shows that the average MOR strength increases with fiber volumes up to ST-2%, while the MOR capacity of ST-4% is almost identical to ST-2%, and decreased strength for ST-6% is primarily because of fiber clogging in the specimens during casting due to the extremely high number of fibers. Fiber clogging and effect of improper distribution can also be observed from the higher range of f_{MOR} in ST-4% result, however, the effects were less severe than ST-6%.

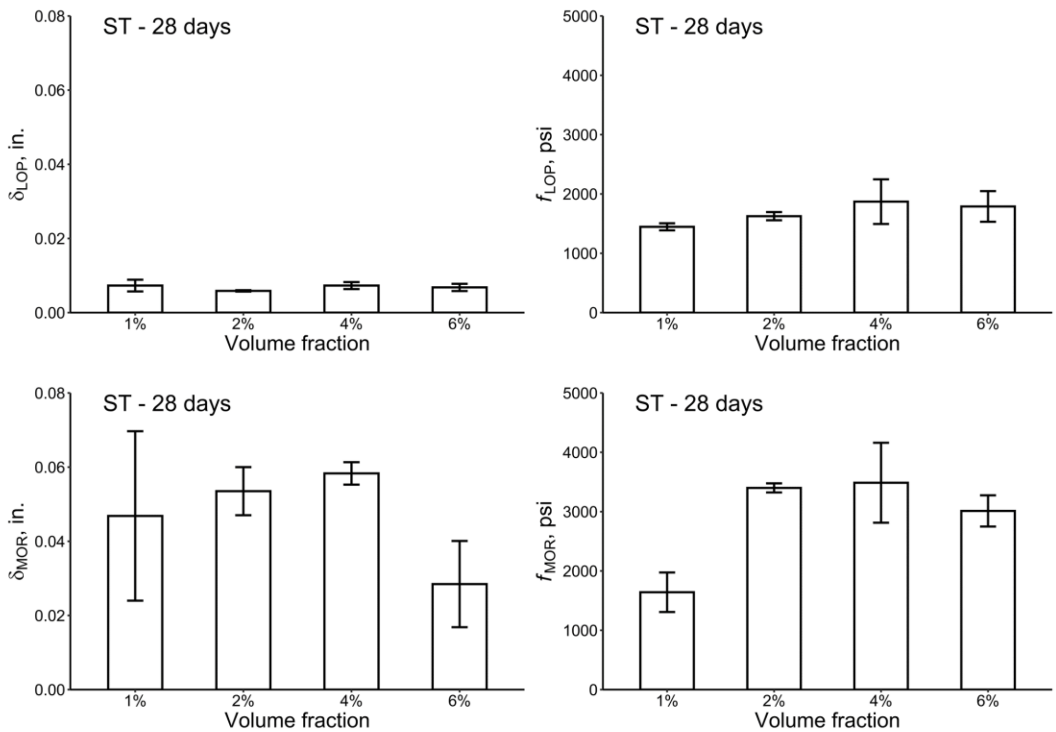

Figure 35. Effect of straight fiber percentages on strength and deflection capacity; at limit of proportionality (LOP) and at modulus of rupture (MOR) at 28 days.

4.3.2 Specimens with Straight Fibers at 56 days

4.3.2.1 Crack Pattern

Similar crack patterns to those observed in specimens tested at 28 days were observed in specimens with straight fibers after MOR tests at 56 days, as shown in Figure 36 - Figure 39. The crack generation process was also similar. First a single hairline crack was generated after the linear elastic stage, then tightly spaced multiple cracks were generated in the fiber activation stage, and later widening of single crack which spanned over all the hairline cracks was observed in the fiber pull-out stage. Similar to specimens tested at 28 days, the patterns of crack formation were mostly linear for the ST-1% and ST-2% specimens, and because of higher fiber number and concrete stiffness, were in a more zigzag pattern in the ST-4% and ST-6% specimens at 56 days. Cracks spanned outside the middle third zone in specimens ST-1-2 and ST-6-2. ST-6-3 generated cracks beyond 5% of the span length outside the middle third zone, and thus those results were discarded. The fracture generated in ST-2-3 was near the edge of the middle third zone.

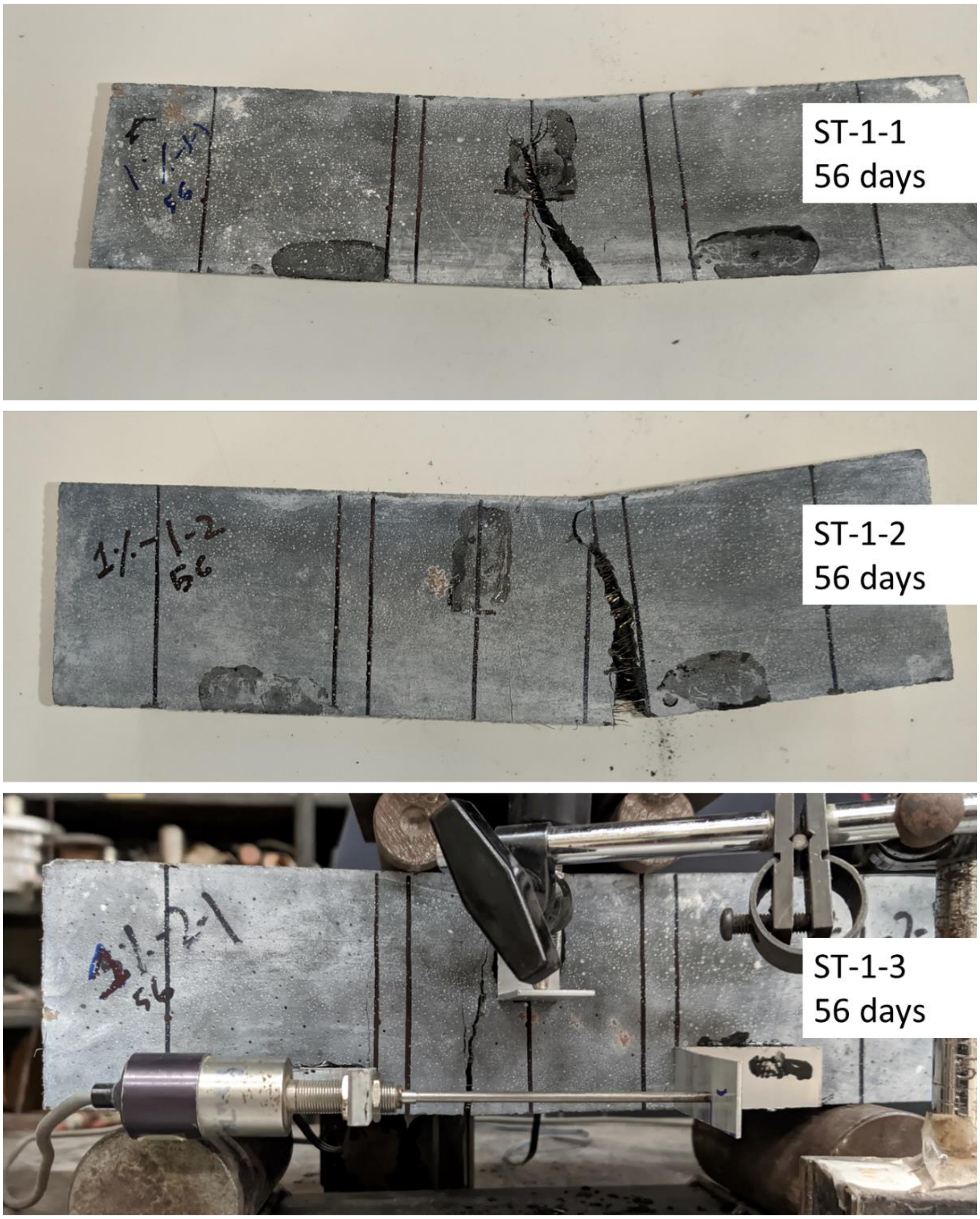

Figure 36. Crack pattern of ST-1% MOR specimens at 56 days age

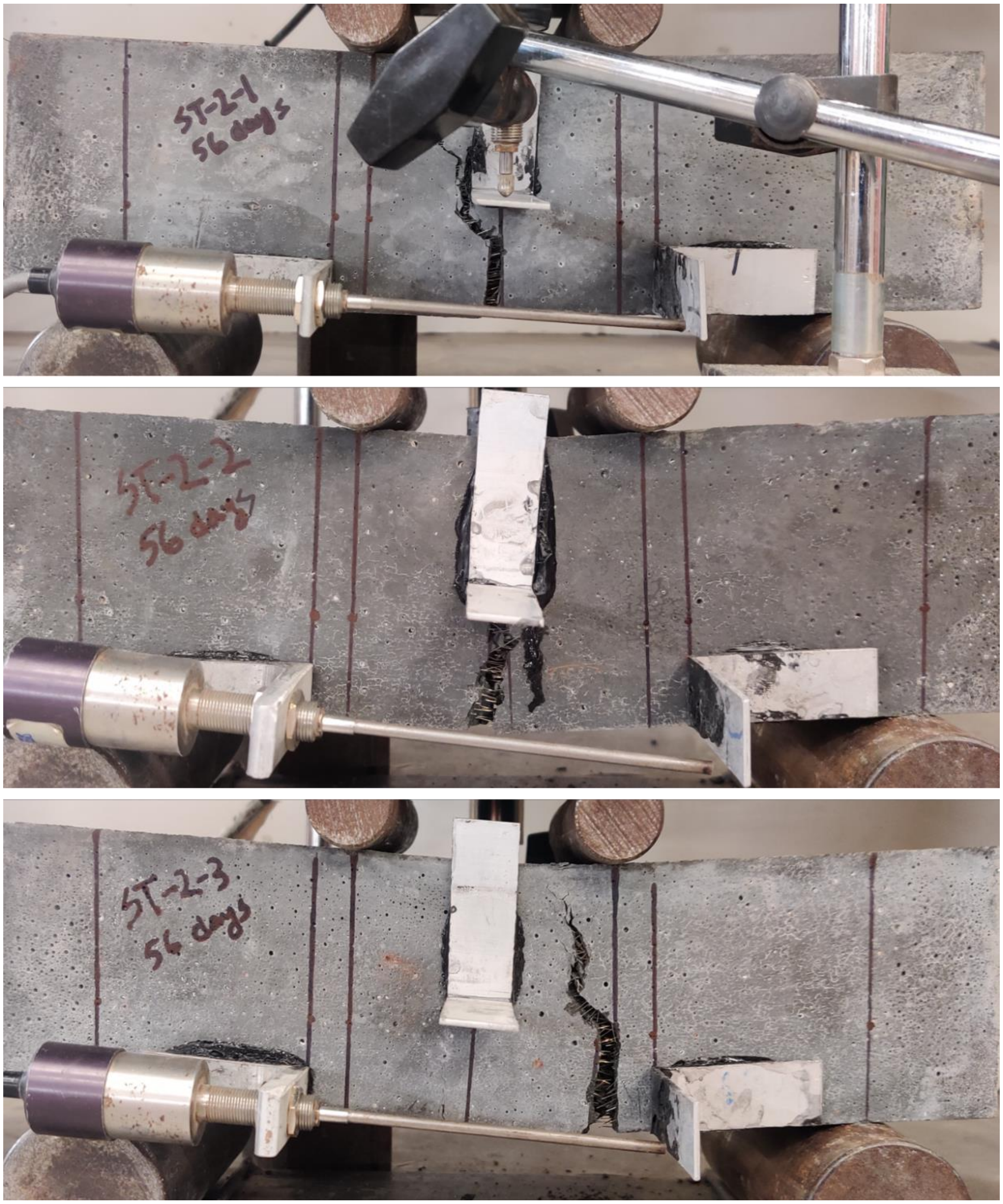

Figure 37. Crack pattern of ST-2% MOR specimens at 56 days age

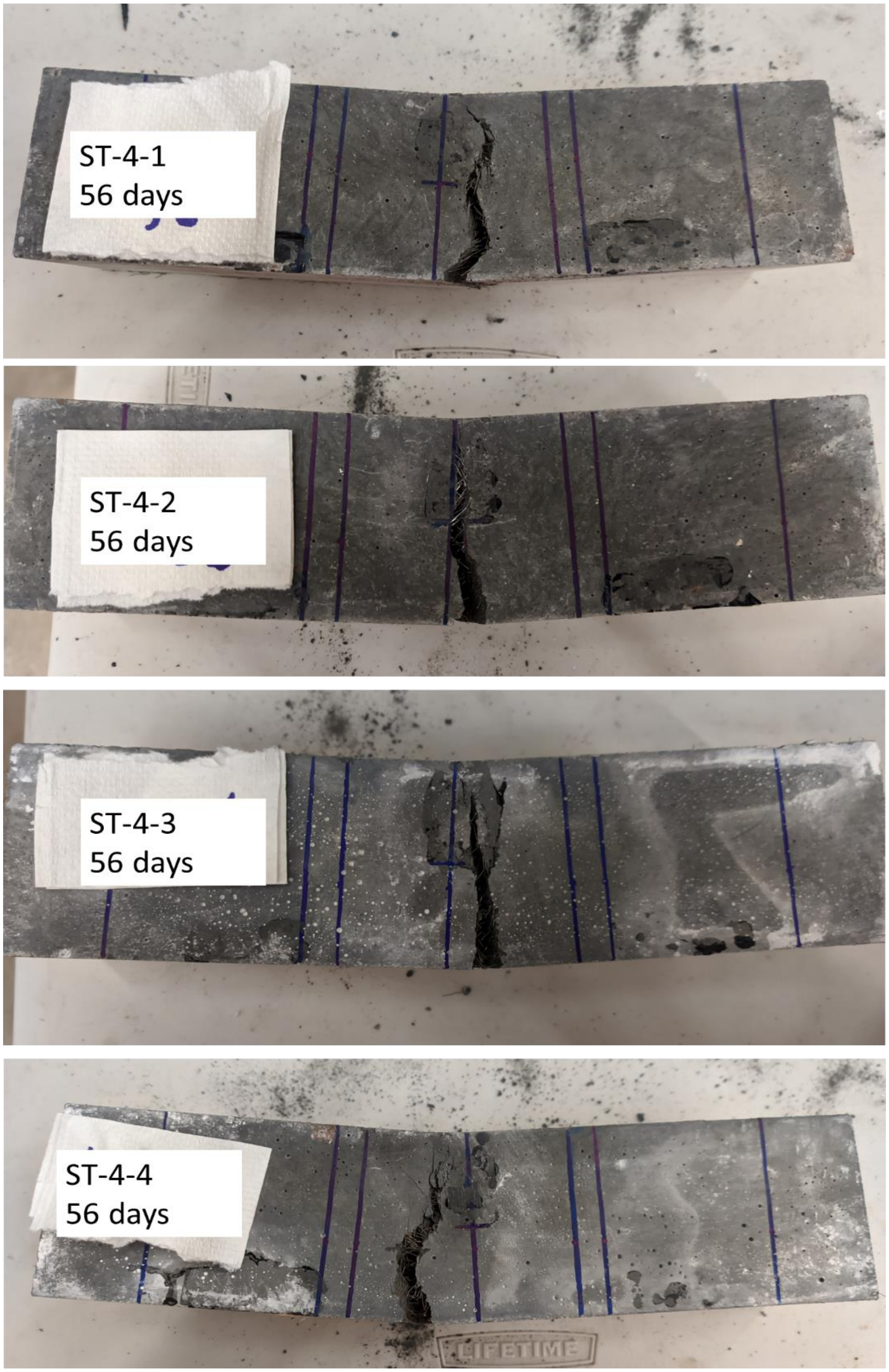

Figure 38. Crack pattern of ST-4% MOR specimens at 56 days age

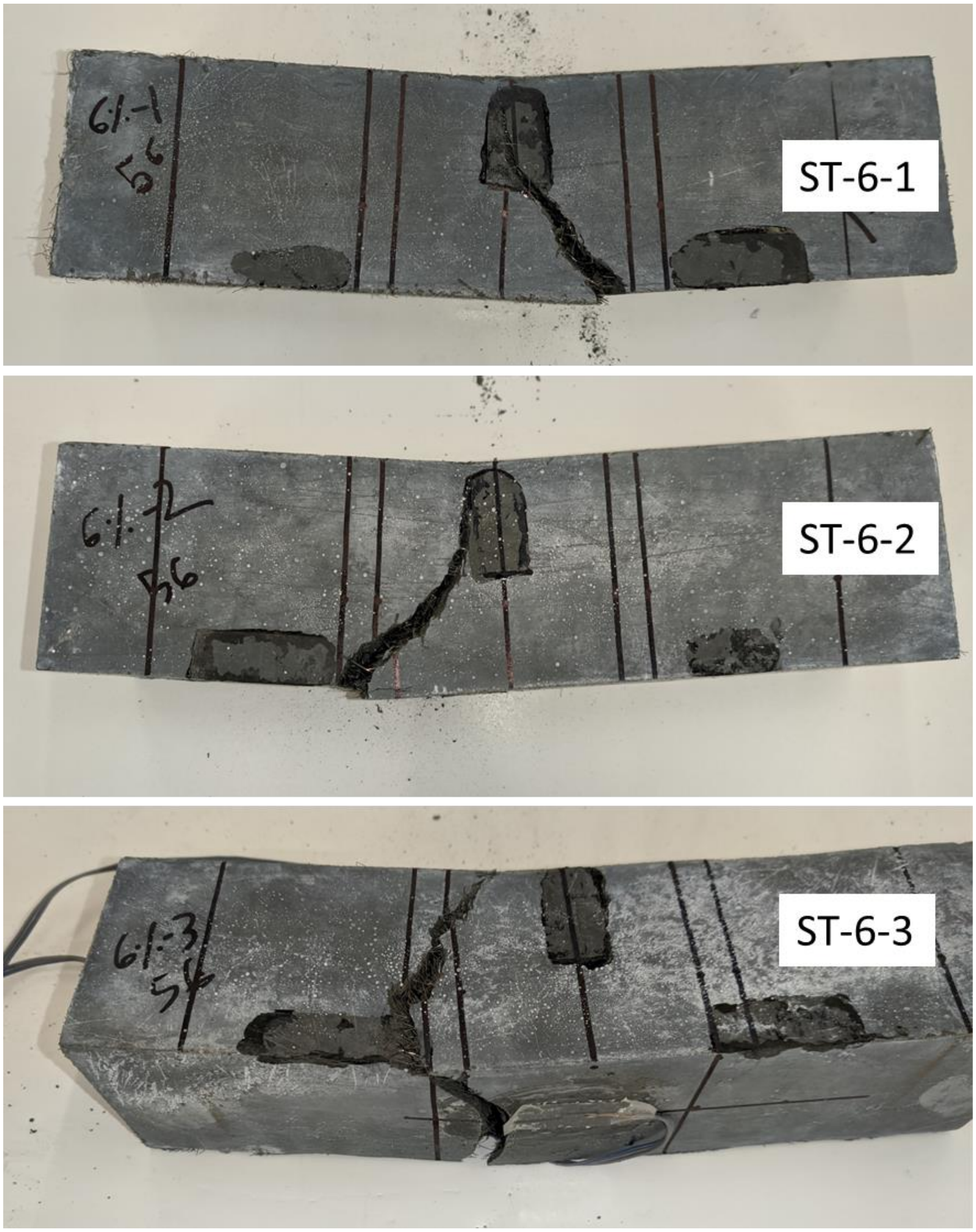

Figure 39. Crack pattern of ST-6% MOR specimens at 56 days age

4.3.2.2 Flexural Behavior

Figure 40 depicts the load-deflection behavior of J3 concrete MOR specimens with straight fibers at 56 days. Three distinctive stages in the load-deflection curves are visible for all the specimens; linear-elastic region, followed by fiber-activation and finally fiber-pullout. All the specimens showed deflection-hardening behavior ($f_{MOR} > f_{LOP}$) except ST-4-2, which showed deflection-softening ($f_{MOR} < f_{LOP}$) behavior after the initial crack.

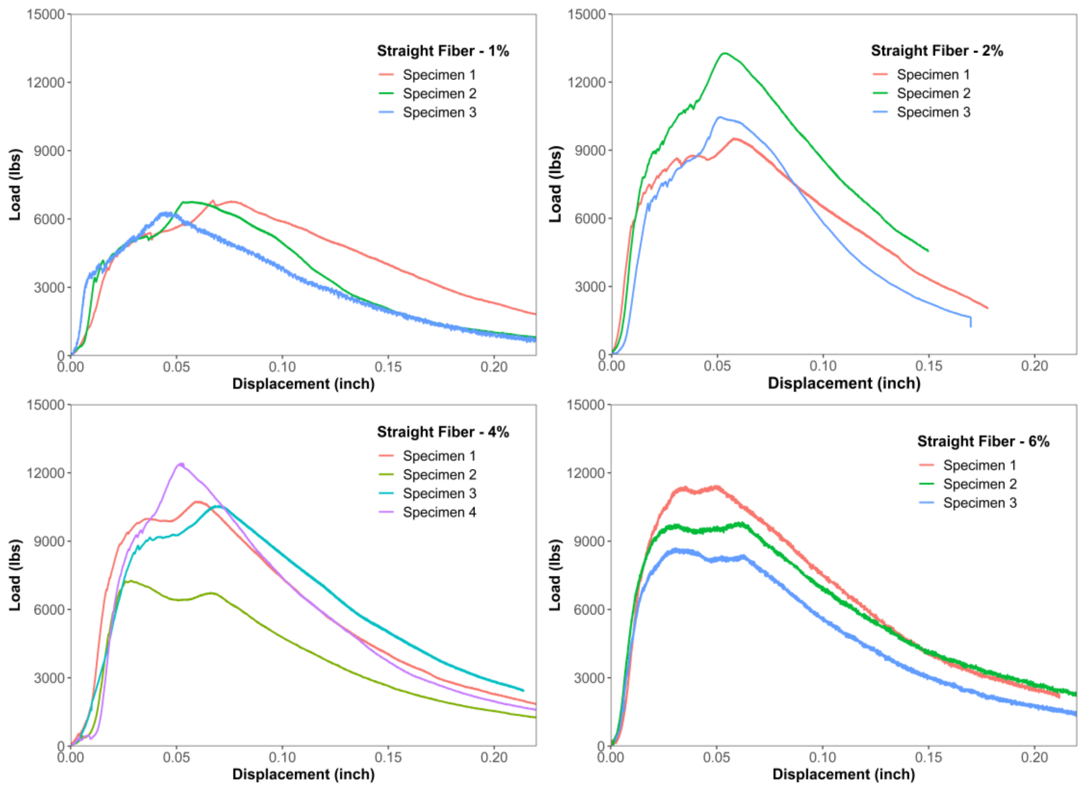

Figure 40. Load - deflection graphs for all straight fiber volumes at 56 days.

These load-deflection curves were used to determine the strength and deflection of the specimens at first-cracking load (LOP) and at post-cracking peak load (MOR). The average strengths of specimens were used to evaluate the effect of fiber percentage on the flexural strength of the J3 mix. However, specimens ST-2-2 and ST-6-3 were excluded from the average strength calculation as the primary crack in these specimens was located outside 5% of the span length beyond the middle third zone as stipulated by ASTM C78 [70]. In addition, specimen ST-4-2 was treated as an outlier because the specimen showed out of plane deflection.

Figure 41 summarizes the effect of straight fiber content on strength and deflection capacity of the specimens at 56 days with mean and first standard deviation. These behaviors closely resemble the behaviors observed from 28 days test results. First crack deflections are between 0.005 in. and 0.0067 in. and decreased with fiber volume. All the fiber percentages showed similar f_{LOP} values, which again indicates that though fiber volume can mildly impact the overall stiffness of the specimens before the first crack, it is not the controlling factor. As with 28 days results, strength increased with fiber volume fraction at LOP, which indicates that fiber presence lengthened the transition zone from linear-elastic stage to fiber activation stage. The average deflection at the MOR point is between 0.048 in. and 0.05 in., which is similar to the 28 days results, which reinforces speculation about fiber effective length. Identical patterns in the MOR strength were observed at both test ages. ST-2% had the highest capacity at 56 days, providing more evidence supporting the claim that ST-2% is optimum and the excessive fiber amount harmed MOR capacity of ST-4% and ST-6%.

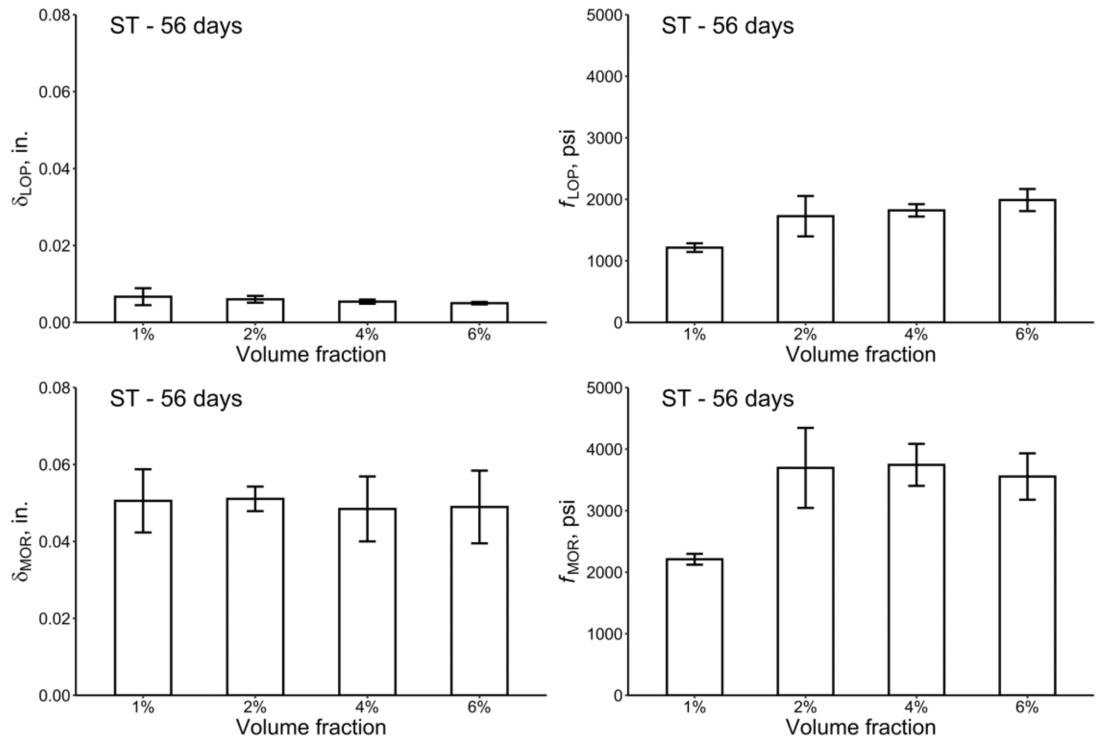

Figure 41. Effect of straight fiber percentages on strength and deflection capacity; at limit of proportionality (LOP) and at modulus of rupture (MOR) at 56 days.

4.3.2.3 Comparison Between Straight-Fiber MOR Strength at 28 and 56 days

To observe the effect of age on the specimens, the ratios of f_{MOR} and energy absorption (toughness or area under load-deflection curve) were calculated out to a deflection of L/10 (where L is span length), or 0.09 in. Figure 42 depicts the ratios of observed strength characteristics at 56 days to those at 28 days. The f_{MOR} ratio is around 1.3 for ST-1%, 1.09 for ST-2%, 1.07 for ST-4% and 1.2 for ST-6%, which show the most benefit from the effect of age. Considering the variability between tests and batches, and limited data points, it is hard to quantify the actual effect of age on f_{MOR} statistically. Increases in average toughness are also visible for ST-1% (ratio = 1.2), ST-2% (ratio = 1.1), ST-4% (ratio = 1.07) and ST-6% (ratio = 1.6). The same pattern is visible for both f_{MOR} and toughness that the effect of aging decreased with fiber volume fraction up to 4% and then again increased for 6%. As overall cementitious amount decreased as fiber volume increased, it was possible that extra cementitious materials impacted the results. However, for ST-6%, it could be control issue as the mix did not have enough flow to ensure proper fiber distribution. Overall observations indicate that bending capacity of the J3 specimens can increase from 28 days to 56 days.

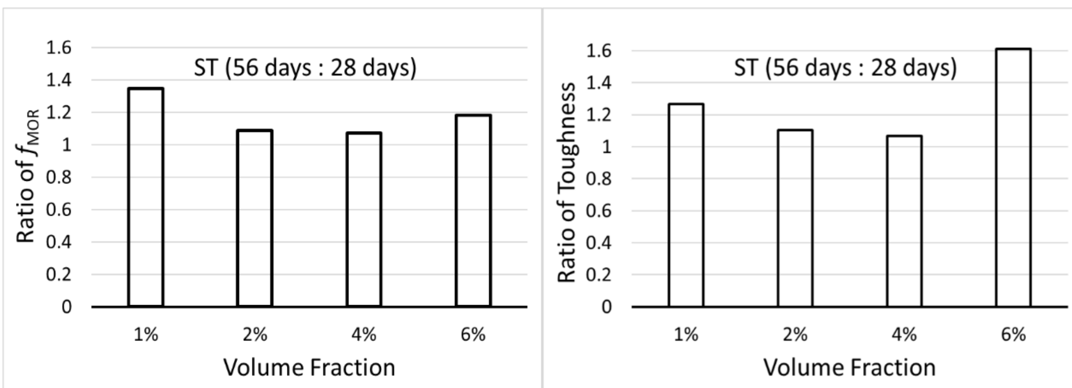

Figure 42. Ratios of strength and absorption capacity of e specimens at 56 days and 28 days of age.

4.3.3 Specimens with Hooked-End Fibers at 56 days age

4.3.3.1 Crack Pattern

Figure 43 - Figure 45 presents the crack patterns for the MOR test specimens with hooked-end (HE) fiber volume fractions at 56 days. As HE fibers were difficult to place, precaution was taken for HE-2% and HE-4% mixes by casting four specimens. Specimens with HE fibers also showed linear-elastic, crack-bridging, and fiber pull-out stages, similar to the ST fiber specimens. The fibers were activated after first crack and multiple cracks appeared after that. However, as the HE-fibers are longer and ends

were designed to fully develop interaction with the matrix, the final crack pattern in the fiber pull-out stage was different from the ST fiber specimens. Specimens with ST fibers showed more or less linear cracks and tried to fail in fiber pull-out. However, specimens with HE fibers exhibited more random cracks indicating failure of the concrete matrix in the final stage. As the HE fibers had better bond capacity due to their geometry, the HE specimens continued to resist significant magnitude of loads regardless of continuous softening of the concrete matrix due to cracking. Except for specimen HE-1-2, all the specimens developed final cracks in the middle third region.

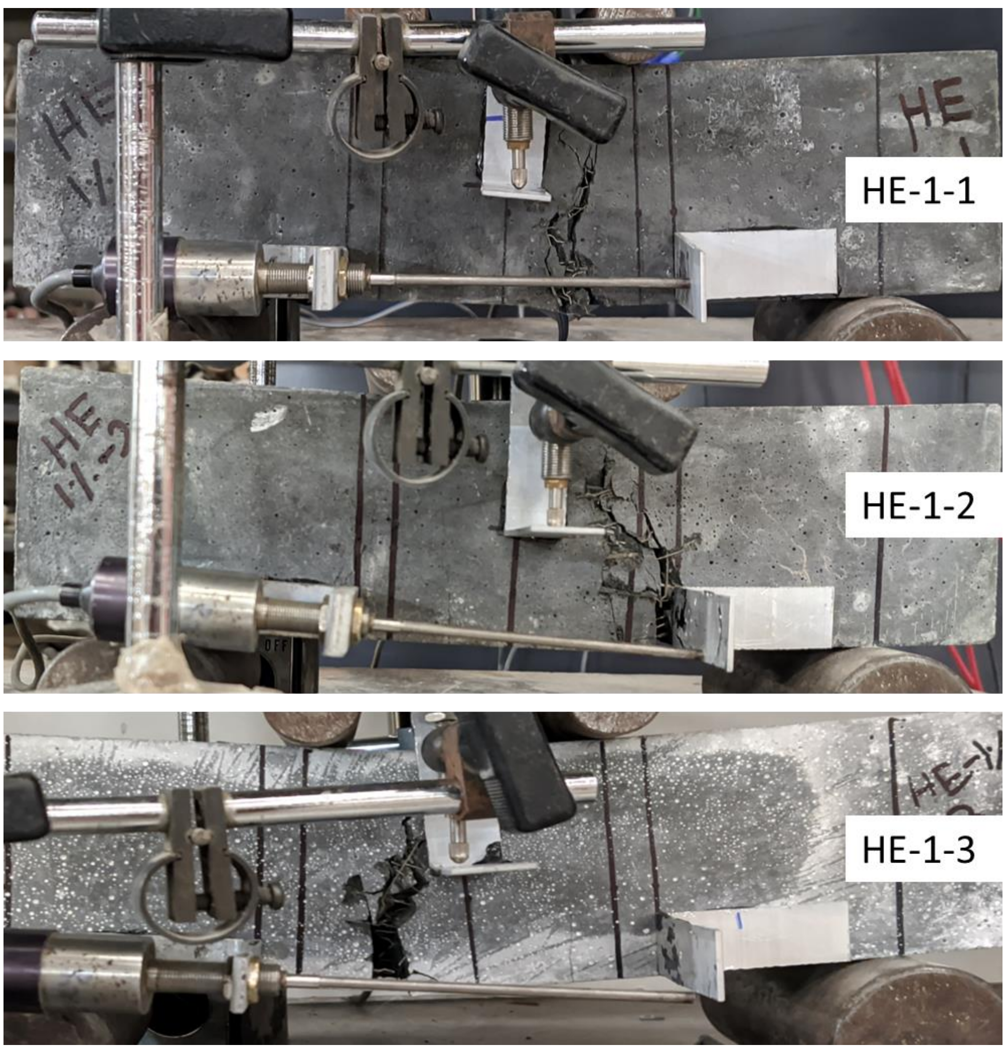

Figure 43. Crack pattern of HE-1% MOR specimens at 56 days age.

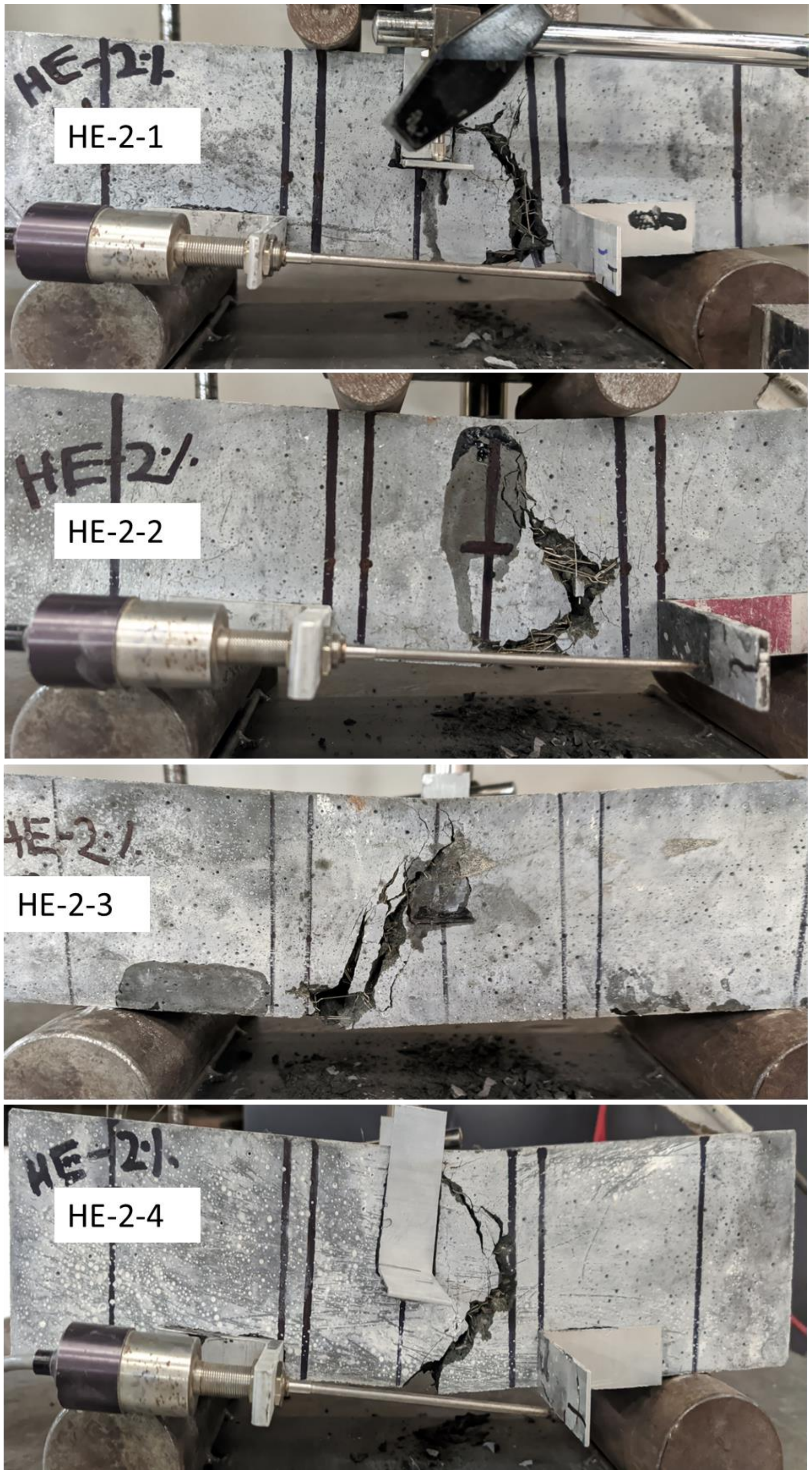

Figure 44. Crack pattern of HE-2% MOR specimens at 56 days age.

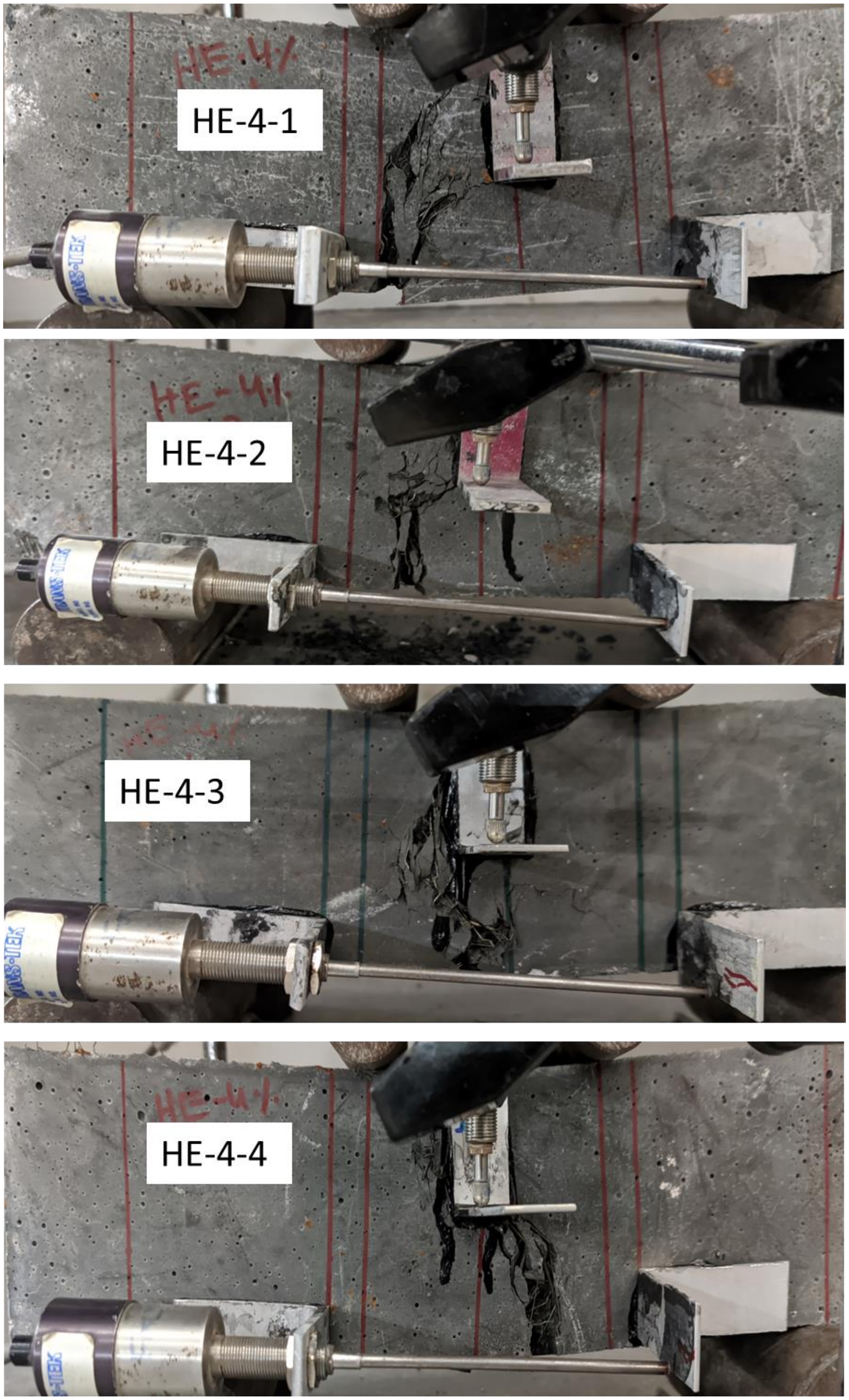

Figure 45. Crack pattern of HE-4% MOR specimens at 56 days age.

4.3.3.2 Flexural Behavior

Distinctive UHPC load-deflection behavior can be seen for the HE fiber specimens in Figure 46. All the specimens showed deflection-hardening behavior ($f_{MOR} > f_{LOP}$). These load-deflection curves were used to calculate average strength of the specimens at LOP and MOR.

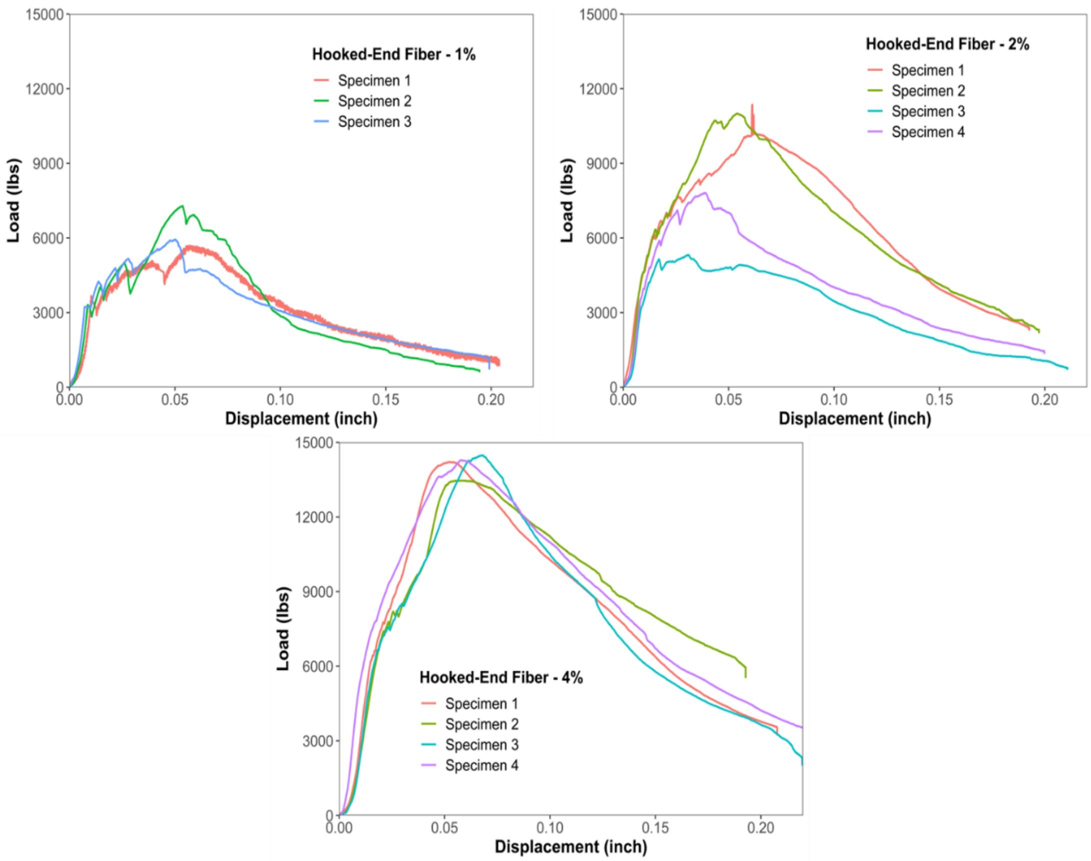

Figure 46. Load - deflection graphs for all hooked-end fiber volumes at 56 days age.

Figure 47 summarizes the strength values observed from the MOR tests for HE fiber specimens at two points (LOP and MOR) with mean and standard deviation. Deflection at first-cracking strength is between 0.0056 in. and 0.0065 in., which is similar to the first-cracking deflections of the specimens with ST fibers. Also, the f_{LOP} values are almost similar (1.2 ksi – 1.7 ksi) for all the fiber volume fractions, which indicates that like ST fibers HE fibers had little impact on pre-cracking concrete properties under flexure. Also, the average deflections at peak load (MOR) are between 0.048 in. and 0.052 in., which are also similar to the observed values from the ST fiber specimens. However, the cause of decreasing load after the peak is different. For the ST fiber specimens, the peak-load deflection was dominated by the fiber pull-out capacity and for the HE fiber, it was the induced damage in matrix that led to decreased load carrying capacity. Though deflections at the LOP and MOR points are the same for different fiber volume fractions, strength increased significantly with fiber amount indicating fibers impacting the post-cracking stiffness significantly.

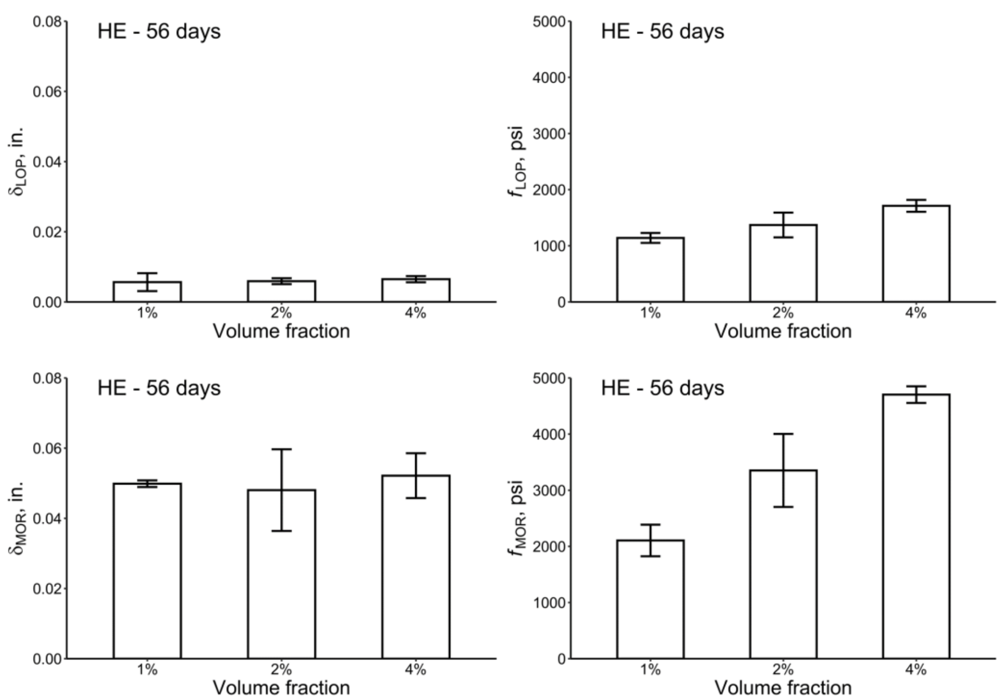

Figure 47. Effect of hooked-end fiber percentages on strength and deflection capacity; at limit of proportionality (LOP) and at modulus of rupture (MOR) at 56 days.

4.3.4 Comparison Between HE and ST Fibers

Figure 48 summarizes the effect of fiber types on the flexural strength of J3 specimens using LOP, MOR, and toughness for comparison. For the first-cracking (LOP) point, the ratios of HE specimen strength to ST specimen strength are 0.94, 0.80, and 0.94 for the 1%, 2% and 4% volume fractions. As f_{LOP} is generally a measure of matrix strength rather than fiber efficiency, it indicates that ST fibers may ensure better concrete matrix. This can be due to proper flow of the concrete mix, fiber distribution and orientation leading to better consolidation and reduced clogging and air content. As HE fibers (1.2 in.) were longer than ST fibers (0.5 in.), it is possible that the specimen dimensions (3 in. width and depth) made it difficult for HE fibers to properly distribute throughout the entire section and may have affected matrix consolidation.

Unlike f_{LOP}, f_{MOR} is a property of fiber efficiency. Figure 48 shows that ratios of f_{MOR} are 0.95, 0.91, and 1.26 for 1%, 2%, and 4% fiber volume fractions, respectively. As HE fibers induce significant damage to the concrete matrix during pull-out due to higher bond capacity, 1% and 2% fiber volume fraction shows lower MOR strength. Unlike HE-1% and HE-2%, HE-4% specimens have enough fibers crossing the damaged concrete zone to distribute larger applied loads. This explains the better MOR capacity of the HE-4% specimens than the ST specimens due to better protection against damage and more efficient load transfer due to higher length. However, HE fibers being longer and having better bond, could hold load for longer duration and deflection which can be observed from toughness ratios except for 1% fiber volume.

These ratios are 0.86, 1.08, and 1.18 for the 1%, 2% and 4% fiber volume fractions, respectively.

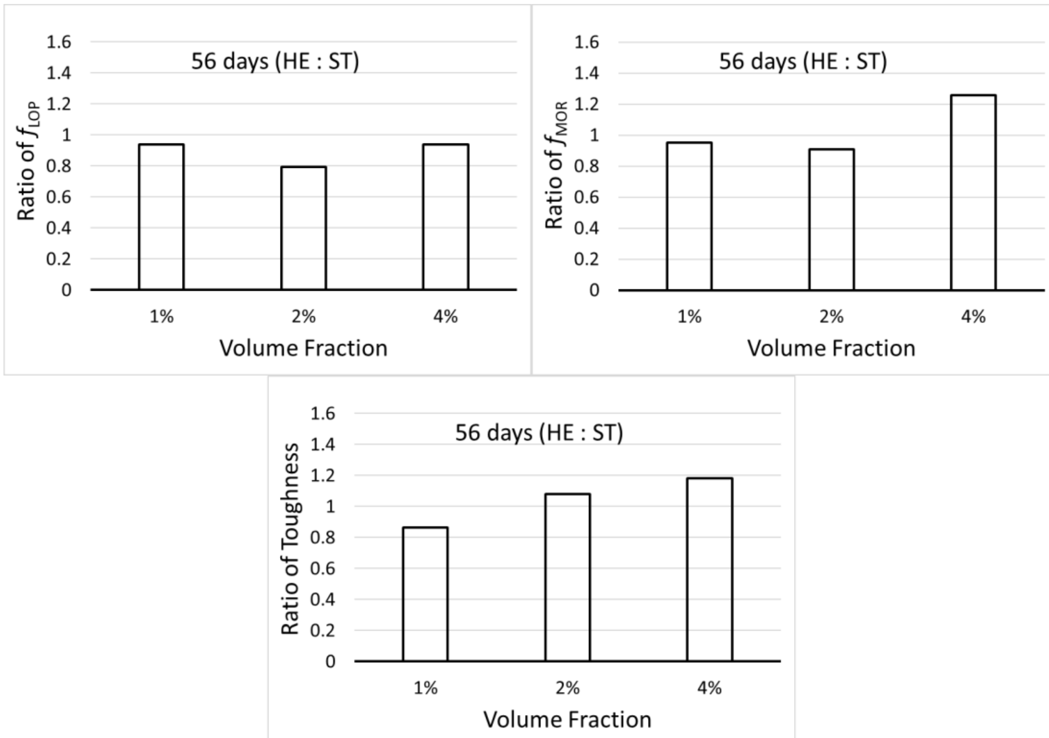

Figure 48. The difference in the strength and absorption capacity of the specimens due to difference in fiber type.

4.4 Direct Tensile Test Results

4.4.1 Specimens with Straight Fibers

4.4.1.1 Crack Patterns

Figure 49 shows the crack patterns observed in the ST-1% specimens during tension testing. A crack developed within the instrumented gauge length for all specimens. All the specimens developed cracks in the cast surface first and then the crack propagated to the other surfaces. All specimens exhibited multiple cracks along the gauge length before crack localization or widening of single crack due to fiber bridging. One specimen showed crack localization at the top of the gauge length, at the aluminum plate used for gripping and the other two showed crack localization in the middle zone of the specimen. After crack localization, the specimens were completely pulled apart and a discrepancy in fiber distribution was observed within the cross-section for all specimens. As the specimens were cast on their side and in the direction of gravity, it was observed at the specific crack location that the fibers tended to settle at the bottom of the form, which led to fewer fibers at the cast surface relative to other portions of the specimens leading to crack generation beginning at the cast surface.

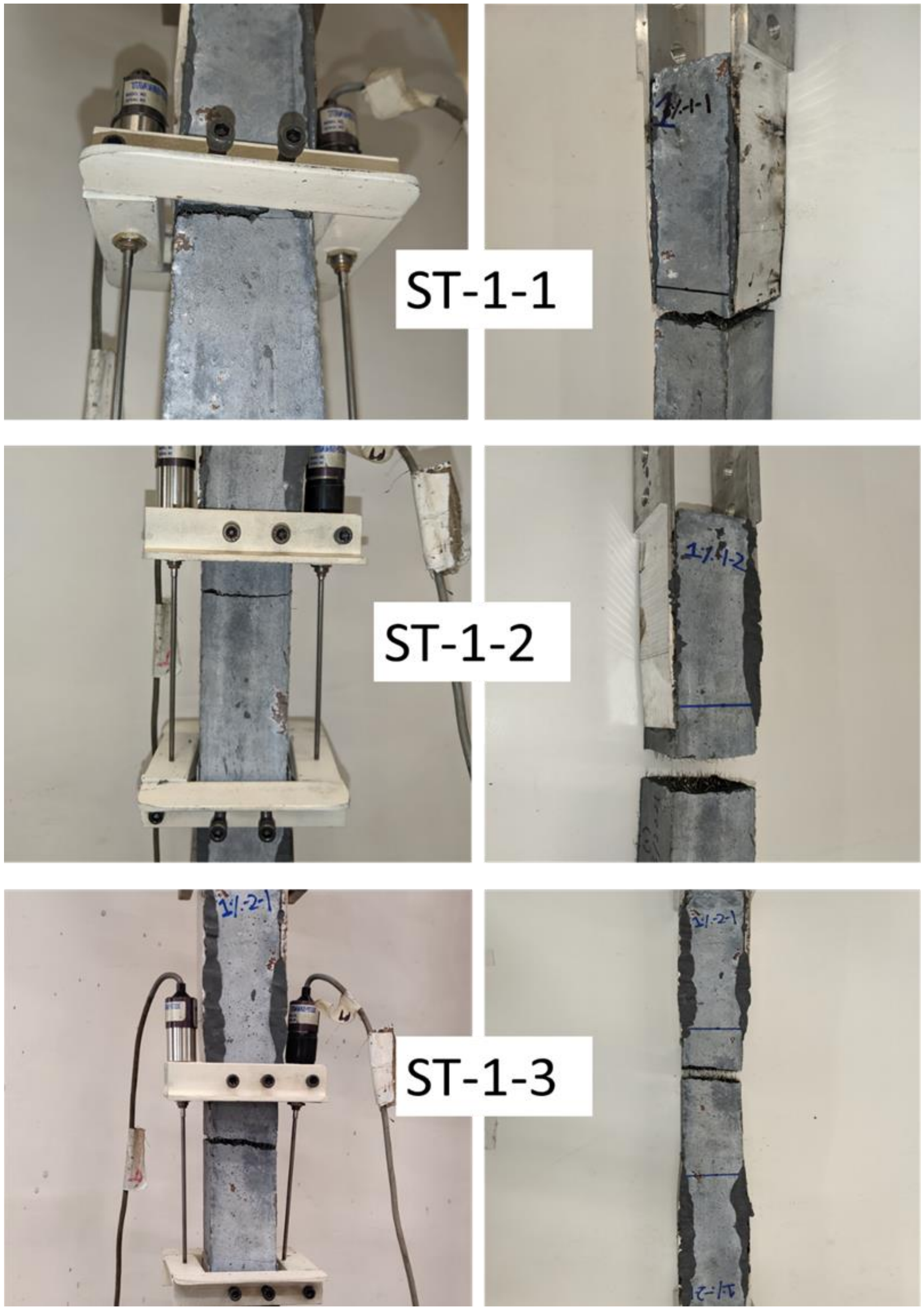

Figure 49. Crack pattern of ST-1% specimens in direct tensile test.

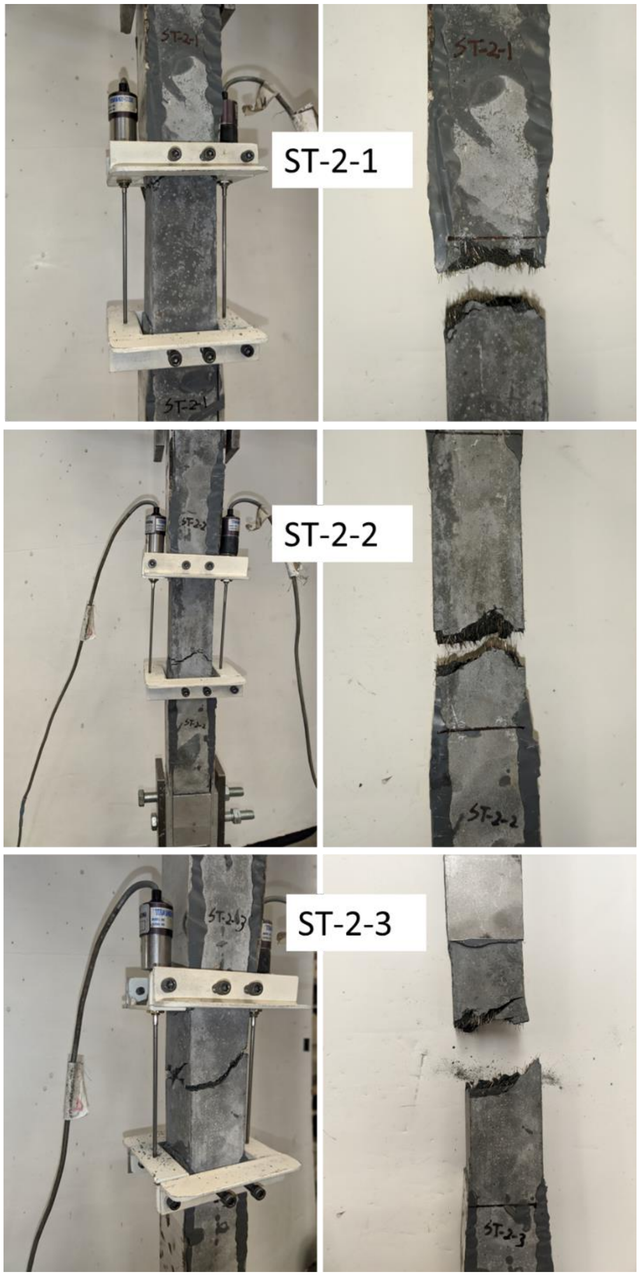

Figure 50 shows the cracks developed in the ST-2% specimens during the direct tensile test. Like the ST-1% specimens, cracks generated within the LVDT instrumented gauge length, and ST-2-1 showed crack localization at the top of the gauge length, where ST-2-3 showed at the middle and ST-2-2 showed crack localization at the relatively bottom portion of the gauge length. After pulling the specimens apart, non-uniform fiber distributions between the top and bottom (as-cast) surfaces was observed at that specific location.

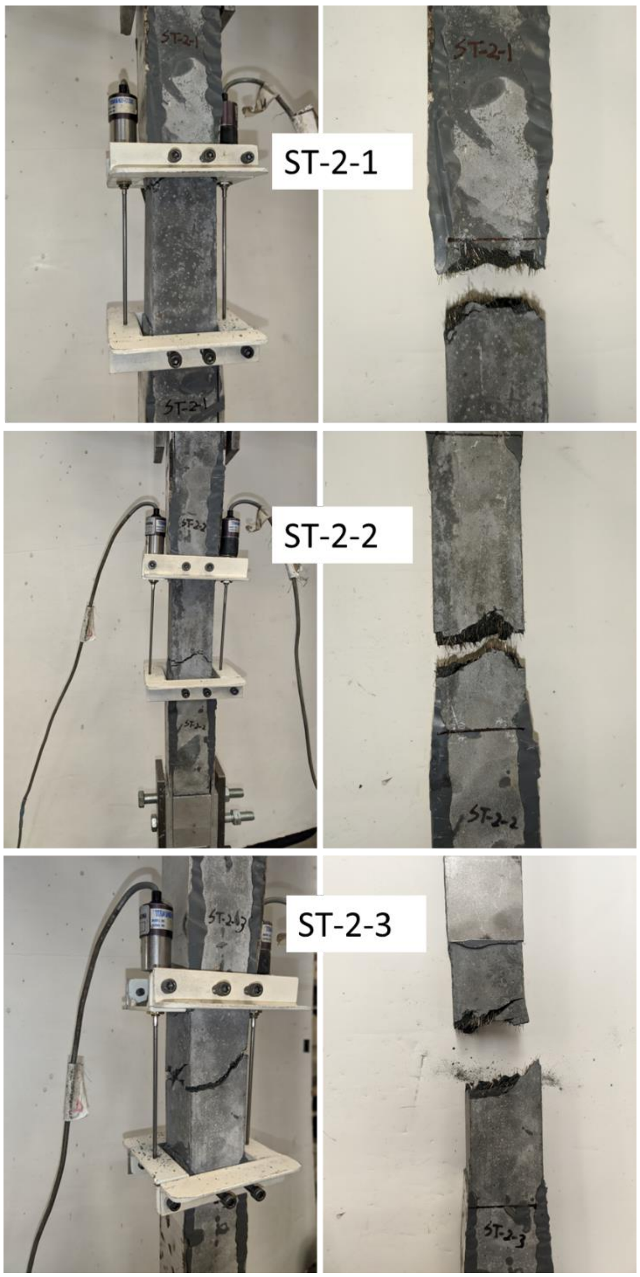

Figure 50. Crack pattern of ST-2% specimens in direct tensile test.

Figure 51 presents the cracks developed in the ST-4% specimens. Two of the specimens generated crack localization near the aluminum plates, but all specimens cracked within the instrumented gauge length. The damage severity in the crack localization zone was much higher for the ST-4% specimens than for the ST-1% or ST-2% specimens. This could be due to the higher number of fibers contributing to fiber bridging, so more energy was required to pull the specimens apart, leading to greater damage to the concrete matrix. Also, the crack patterns became highly non-uniform and did not cross the specimens in a straight line. The disparity in distribution of fibers described for the ST-1% and ST-2% specimens was also visible.

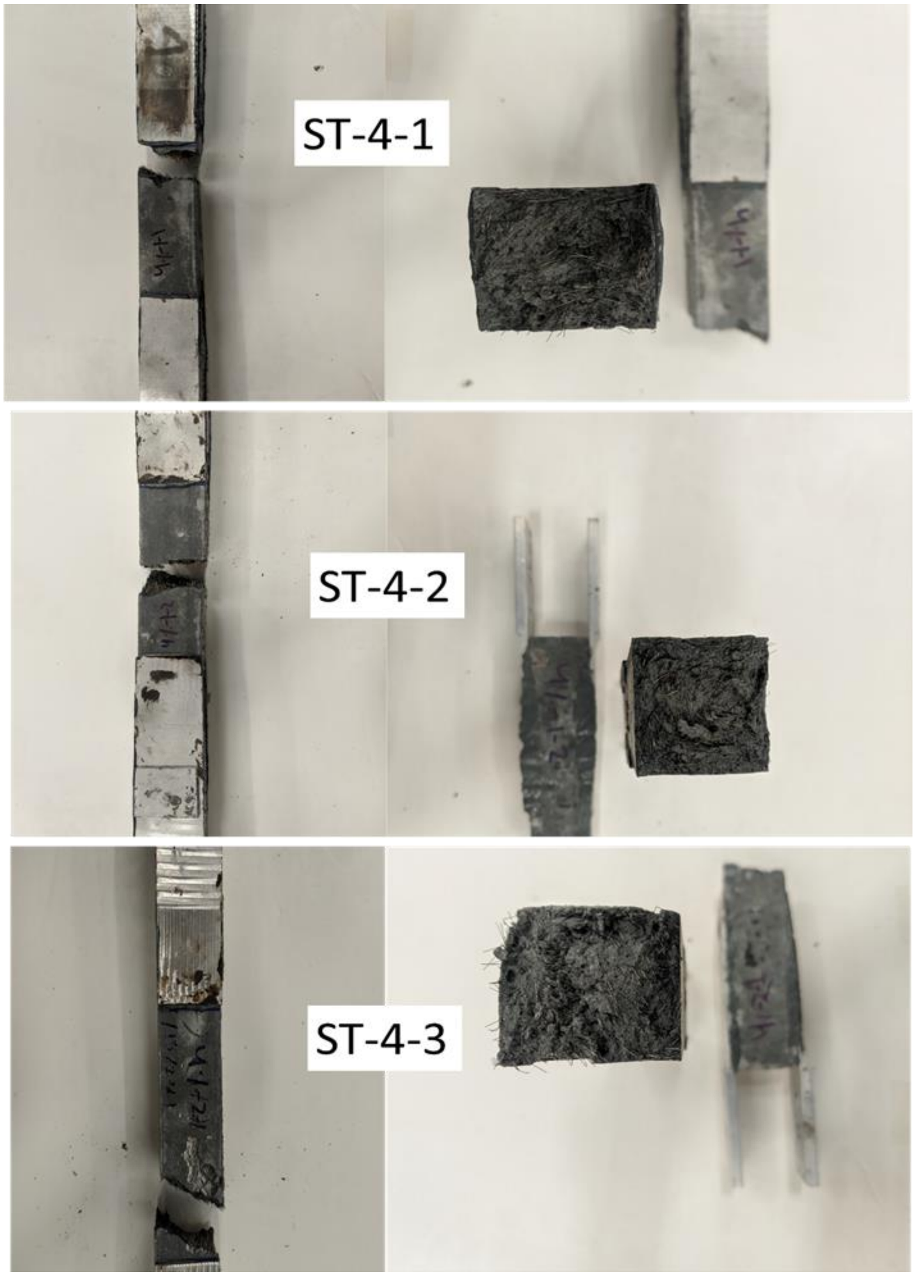

Figure 51. Crack pattern of ST-4% specimens in direct tensile test.

Figure 52 presents the ST-6% specimens after direct tensile testing. The specimens showed similar crack patterns to the ST-4% specimens. Two of the specimens had crack localization near the end of the aluminum loading plates and the other one showed localization in the middle of the specimen, however, all the crack localizations were within instrumented gauge length. The crack pattern was non-uniform, and severe damage similar to the ST-4% specimens was also observed in the ST-6% specimens. Non-uniform fiber distribution between casting and bottom surfaces was also present in all the specimens.

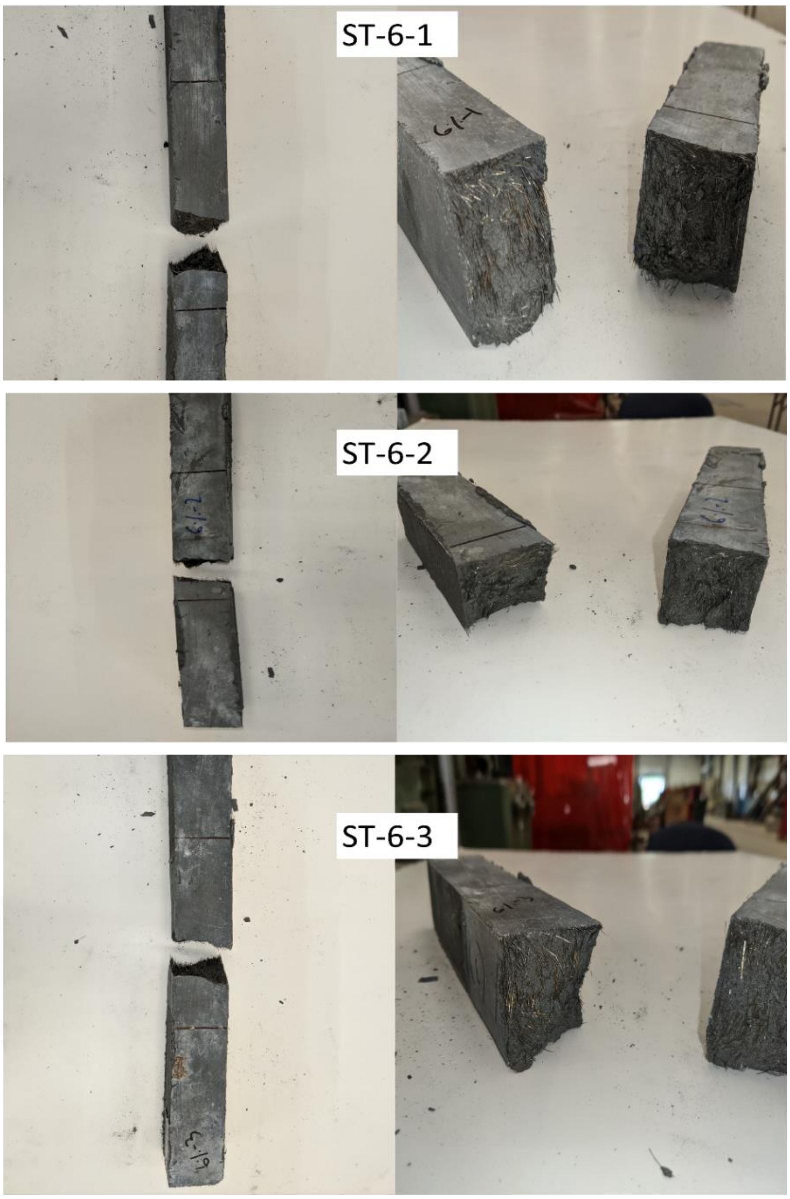

Figure 52. Crack pattern of ST-6% specimens in direct tensile test.

4.4.1.2 Axial Stress-Strain Behavior

According to Graybeal and Baby [37], in addition to tensile stress, specimens tested using this method are subjected to stress due to gripping and flexure. Bending behavior was observed at the moment of first-cracking in all of the specimens. In addition, as the casting surface had less fibers compared to the as-cast bottom surface at the locations where the specimens fractured, differential concrete section properties were present in two of the specimen faces. Due to specimens developing cracks in the cast surface first and then the crack propagating to the other surfaces, there was bending for a brief moment in the stress strain behavior. As the flexural strain gradient can reduce the strain reading from the LVDT mounted near the as-cast bottom surface, average strain values from the two different faces can provide more accurate overall strain values during the multi-cracking phase.

Figure 53 and Figure 54 present the stress-strain behavior of J3 specimens with steel microfibers. To negate the effect of bending strain the average strain values from two LVDTs across the whole gauge length were calculated. According to Graybeal and Baby [37] uniaxial tension response of UHPC can be observed in four distinct phases: elastic, multi-cracking, crack straining, and crack localization. From the stress-strain responses, linear elastic behavior of the specimens can be observed until first crack, which represents the tensile strength of the cementitious composite. After first crack, an almost constant stress level was present, which is the phase when multiple cracks formed within the gauge length because of fiber bridging. As the strength of cracked section is much higher than the uncracked section because of the interaction of steel fibers, fiber bridging takes place [37] This phase was more significant in the ST-1% and ST-2% specimens due to relatively better distribution of fibers. As the post-cracking behavior of UHPC is a function of fiber efficiency and matrix characteristics, it is possible for different specimens to demonstrate different behavior [37]. In the next stage, crack opening of the specimens happens because of the combination of elastic hardening and debonding between concrete matrix and fibers [37]. Except for specimens ST-1-1 and ST-4-2, every specimen showed higher post-cracking strength than strength at first-cracking, which also can be referred to as strain-hardening behavior [18]. The final stage of the axial stress-strain response is the continued widening of the specimens due to fiber pull-out and separation of the specimens into two halves. The average strain value when the specimens generated large crack opening or crack localization was much smaller for ST-4% and ST-6%.

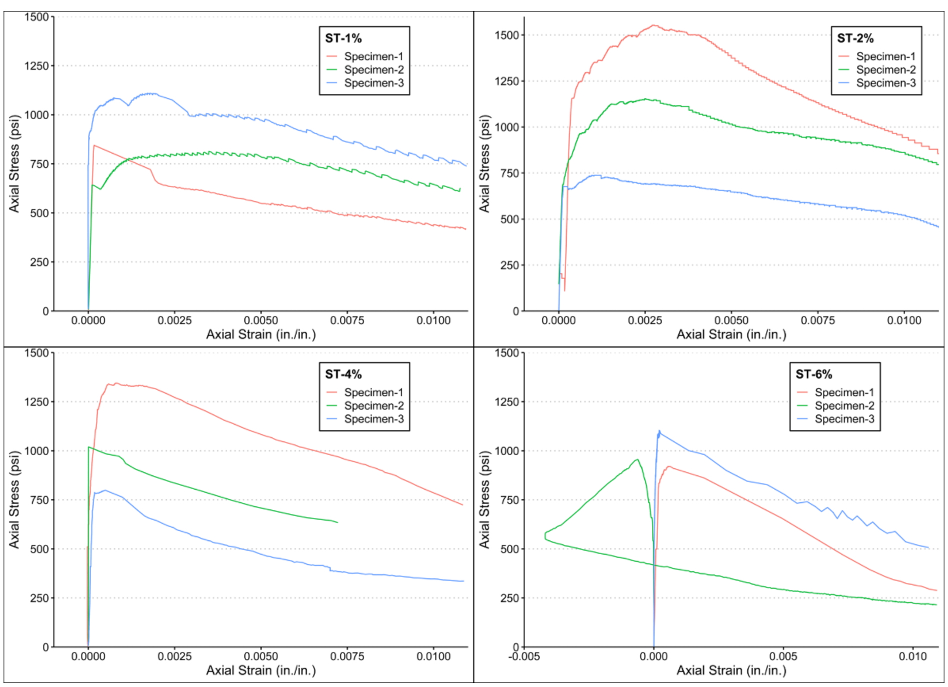

Figure 53. Full axial stress-strain behavior of J3 specimens with ST microfibers.

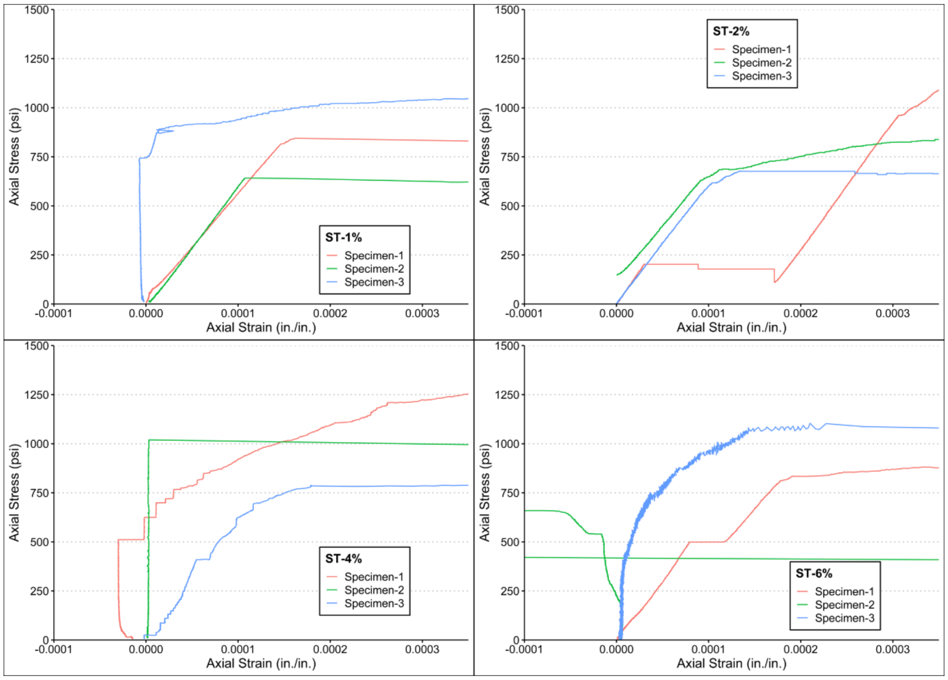

Figure 54. First-crack region of average axial stress-strain behavior of J3 specimens with ST microfibers.

4.4.2 Specimens with Hooked-End Fibers

4.4.2.1 Crack Patterns

Figure 55 depicts the cracks in the specimens tested under direct tensile load with 1% HE fibers. The cracks started to propagate from the cast surface to the bottom surface, which can be clearly seen in specimen HE-1-3. This was because of the tendency of the fibers to settle at the bottom, and this induced bending stress in the specimens during the first-cracking stage. Unlike the specimens with ST fibers, this bending of the specimens was present after the first cracking point. During the crack saturation stage, rather than widening of cracks due to fiber pull-out like the straight microfibers, the fibers caused damage to the specimen matrix. This characteristic of hooked-end fibers was also seen in the flexural tests. All the HE-1% specimens generated cracks within the gauge length. Expect for the HE-1-2, all the specimens showed crack localization at the middle of the gauge length.

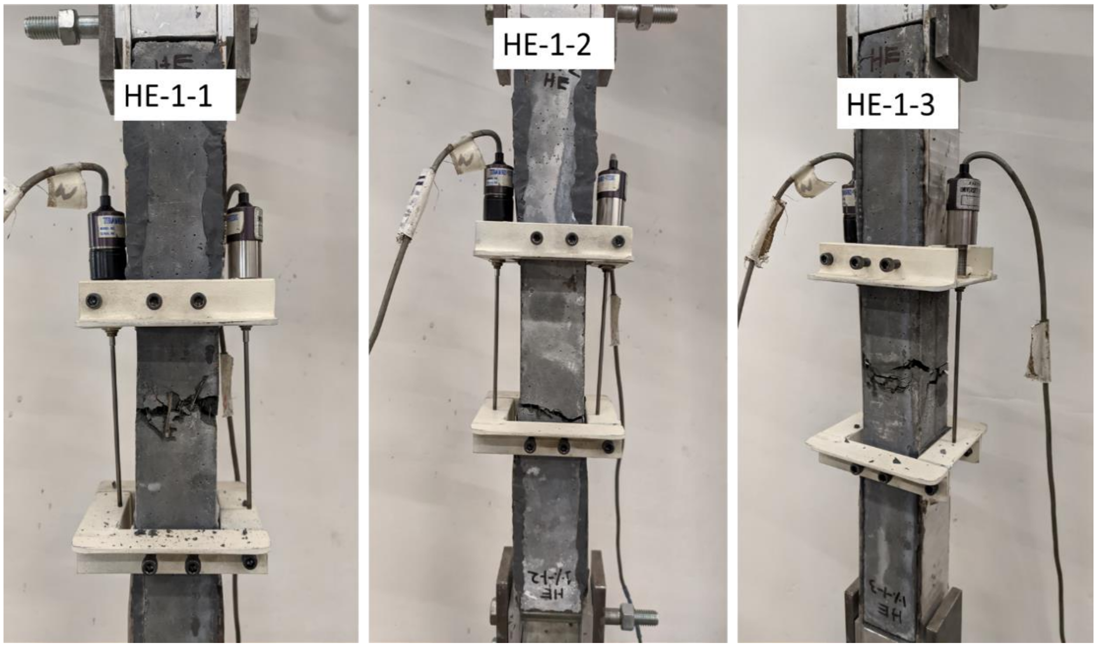

Figure 55. Crack pattern of HE-1% specimens in direct tensile test.

Figure 56 presents the crack pattern observed for the HE-2% specimens due to direct tension load. Bending was clearly observed in all the specimens, which can be at least partially attributed to the distribution of the fibers across the cross-section. Fiber distribution can be observed in the picture of the broken surface of specimens HE-2-1 and HE-2-2 in Figure 56. The response of the specimens was like the HE-1% tests and the cracks were highly irregular across the sections. All the tested specimens showed crack localization at the middle of the gauge length.

Figure 56. Crack pattern of HE-2% specimens in direct tensile test.

Only two specimens of HE-4% were tested under direct tension, as the third one had a substantial number of air voids in the specimens and due to high fiber amount the shape was irregular. Figure 57 presents the crack pattern that developed in the HE-4% specimens due to direct tensile test. The observations were similar to the HE-2% specimens and observed bending of the straight specimens continued after first cracking. Both specimens failed at the middle of the gauge length.

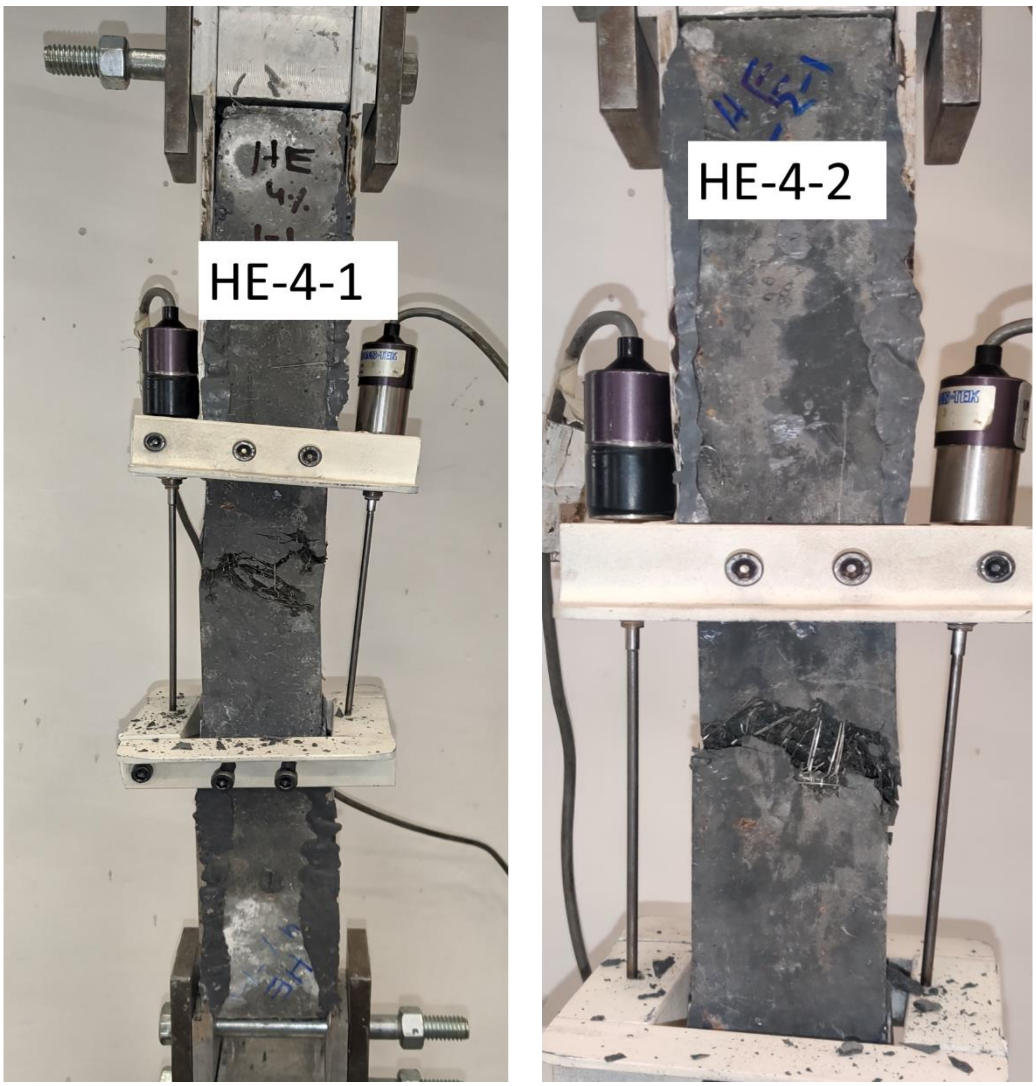

Figure 57. Crack pattern of HE-4% specimens in direct tensile test.

4.4.2.2 Axial Stress-Strain Behavior

Figure 58 and Figure 59 present the axial stress-strain behavior of J3 specimens with HE fibers. The deformation values measured on the two faces were averaged and used to calculate the average strain so that the effect of bending could be mitigated. However, unlike J3 specimens with ST fibers, specimens with HE fibers experienced bending after first cracking, which influenced the results. Similar to the specimens with ST fibers, all HE fiber specimens showed the first two significant phases, linear-elastic and multi-cracking phases. Specimen HE-1-2 experienced a sudden crack opening in addition to bending during the first-cracking phase, which significantly increased the strain in the specimen, which can be seen from the graphs. All the specimens showed a distinctive multi-crack phase. The HE-2% and HE-4% specimens showed strain-hardening behavior, whereas the HE-1% specimens showed strain-softening behavior. Crack localization occurred due to damage of the specimen matrix in the cracked zone rather than fiber pull-out.

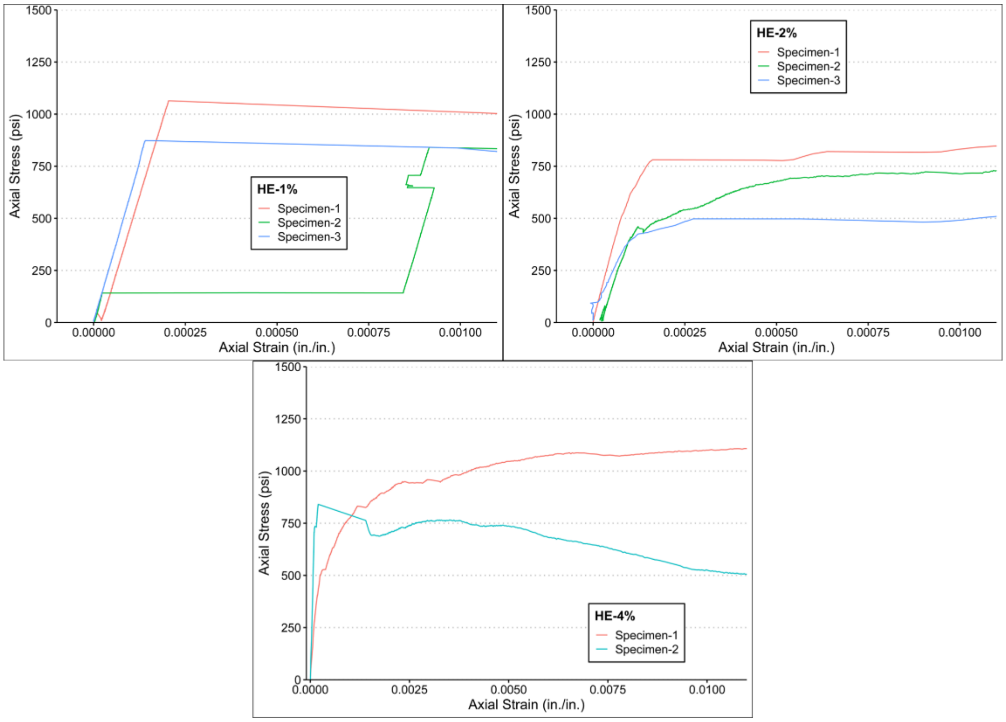

Figure 58. Full axial stress-strain behavior of J3 specimens with hooked-end fibers.

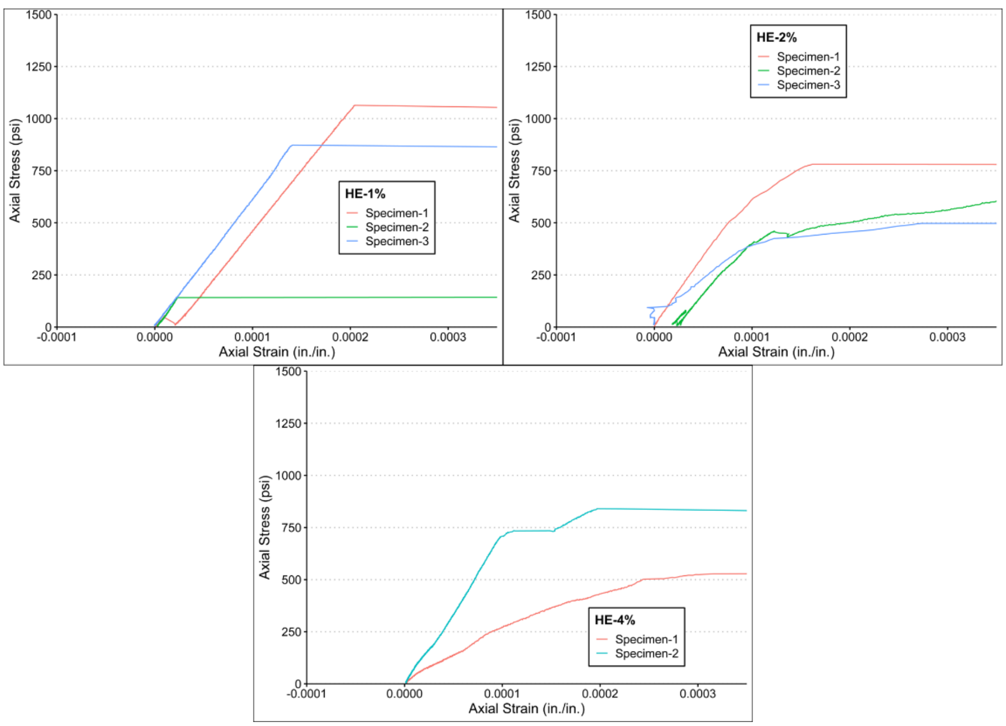

Figure 59. First-crack region of average axial stress-strain behavior of J3 specimens with hooked-end fibers.

4.4.3 Effect of Fiber Content and Fiber Types on the Direct Tensile Strength of J3 Specimens

Stress-strain relationships of the J3 specimens with different fiber types and fiber contents were used to calculate the maximum axial load capacity in tension. Maximum load capacities of the specimens were used to compare between the efficiency of fiber amounts and types for resisting tensile loads.

Figure 60 presents the average maximum tensile stress with standard deviation of the tested specimens with different types and fiber percentages. In case of the straight fibers, maximum average strength increased up to 2% fiber volume and then decreased with increasing fiber volume fraction. This trend is similar to flexural capacity, which indicated that there was no advantage of using ST fiber amounts higher than 2%.

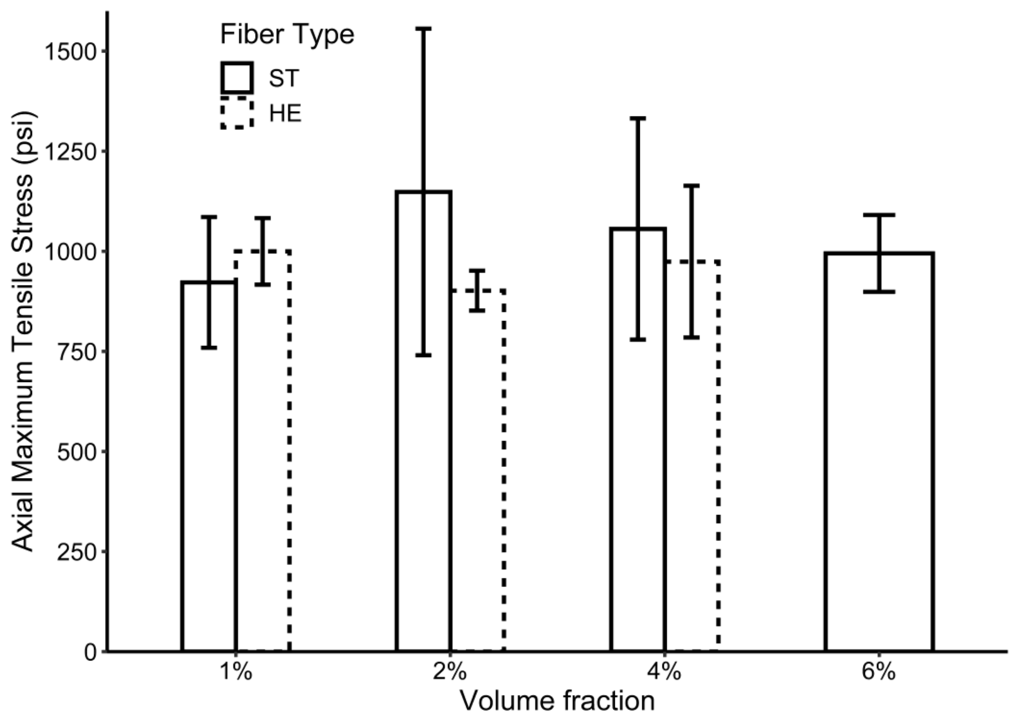

Figure 60. Average maximum tensile stress with different fiber types and content.

While evaluating the performance of specimens with hooked-end fibers, the HE-1% had the highest strength, followed by HE-4% and then HE-2%. A lower number of HE fibers can be beneficial for this test as HE fibers resulted in significant damage to the surrounding concrete matrix during the multi-cracking phase and onwards. From the results of flexural tests, it can be observed that having a higher number of fibers in the cracking zone provides protection from damage, however fiber distribution plays an important role in the direct tensile strength test. Having a higher quantity of 1.2 in. long fibers in a specimen with a 2 in. by 2 in. cross-section can significantly affect the fiber distribution. Thus, a decrease in tensile capacity was observed with higher quantities of hooked-end fibers.

When considering the effect of fiber types on tensile strength, it can be observed that for 1% fiber contents HE fibers performed better than ST fibers. This can be explained by the fact that HE fibers provide better reinforcement to the concrete matrix than straight microfibers. However, this advantage diminishes with further increasing fiber contents, (such as 2% and 4% fiber volume fraction in this research) because of difficulty in achieving proper fiber distribution.

4.5 Splitting-Tensile Strength Test

This test was performed on specimens having hooked-end (HE) fiber volume fractions of 1%, 2% and 4% at 56 days of age. Four specimens were cast and tested for HE-2% and HE-6% mixes. Four specimens were tested for these fiber contents as there were higher possibilities for generation of air pockets in HE-2% and HE-4% specimens due to flowability issues.

4.5.1 Crack Patterns

Figure 61 shows the crack patterns for HE-1% specimens under splitting-tensile loads. The first crack started developing in the middle of the gauge length for each specimen. However, after the first crack random cracks started developing across the section because of fiber-bridging. Specimen HE-1-1 developed cracks below the aluminum angle used to measure deflection in the multi-cracking phase, which caused the angle to debond and left the specimen with only one working LVDT. Development of the cracks in the specimens depended on the properties of the matrix and the crack pattern was random for each specimen. Generation of a visible crack on one face of the specimen did not guarantee the generation of crack on the other face. Generally, the first crack appeared at the as-cast surface. After the first crack, the specimens were subjected to a combination of compression and tensile stress. So alongside pulling the fibers out of the matrix, the surfaces subjected to loading were observed to flatten over the remainder of the test, as visible in Figure 61. The ultimate failure mode was crushing of the concrete in the two attached surfaces.

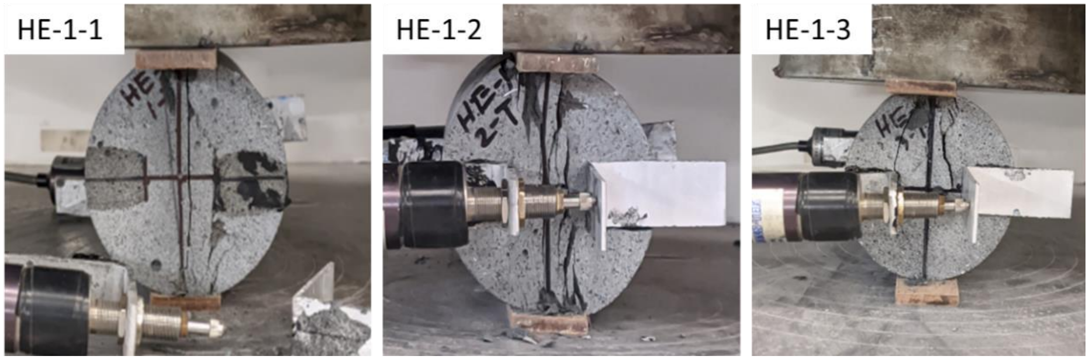

Figure 61. Crack patterns in HE-1% specimens after the splitting-tensile test.

Figure 62 presents pictures of the cracks developed in the HE-2% specimens during the splitting-tensile test. Like the HE-1% specimens, the HE-2% specimens exhibited random cracks after the first cracks and ultimately failed due to the crushing of the surfaces subjected to loading. Due to generation of the random cracks, aluminum angles attached to specimens HE-2-1, HE-2-2, and HE-2-4 fell off the as-cast surface. Like the HE-1% specimens, the HE-2% specimens were subjected to extreme damage and spalling of concrete during the fiber pull-out stage.

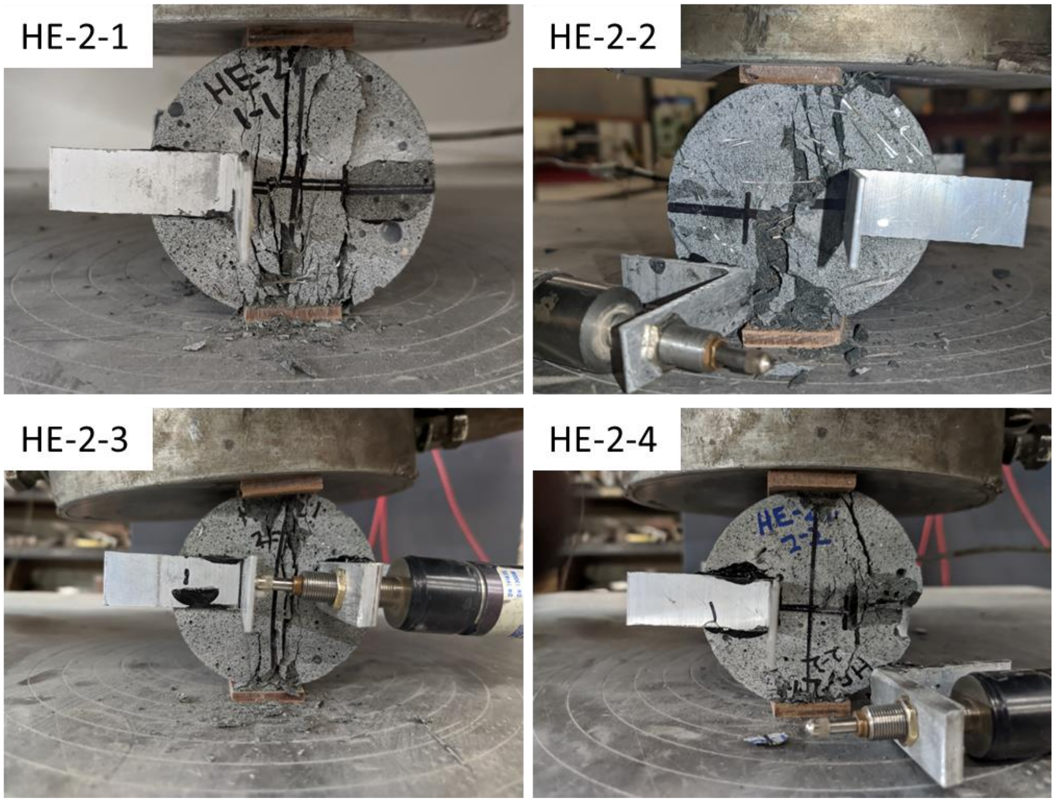

Figure 62. Crack patterns in HE-2% specimens after the splitting-tensile test.

Figure 63 presents the cracks developed in the HE-4% specimens during the splitting-tensile test. The crack development and failure pattern were like the HE-1% and HE-2% specimens. However, the induced damage in the specimens were less than for the HE-1% and HE-2% specimens due to a significantly higher amount of fibers present to resist damage.

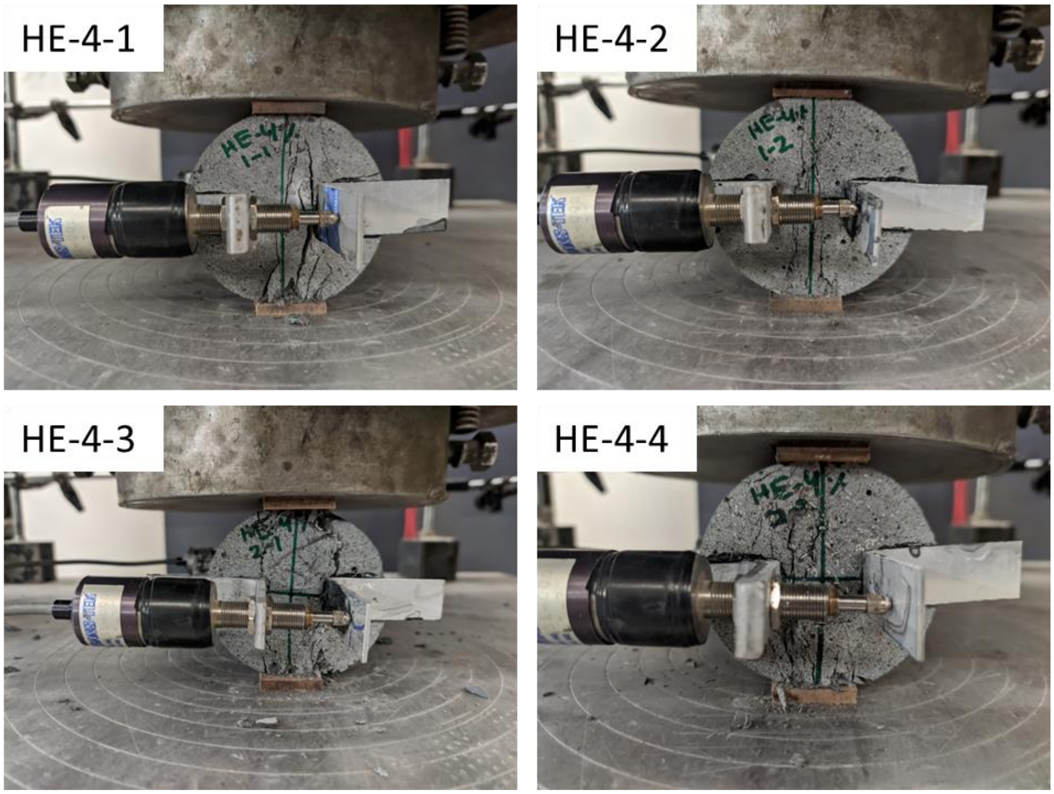

Figure 63. Crack patterns in the HE-4% specimens after splitting-tensile test.

Alongside cracks parallel to the line of loading, the specimens also generated cracks perpendicular to the loading line in the periphery. A typical specimen with this crack pattern is presented in Figure 64. These cracks were generated in the multi-cracking phase due to the presence of compression.

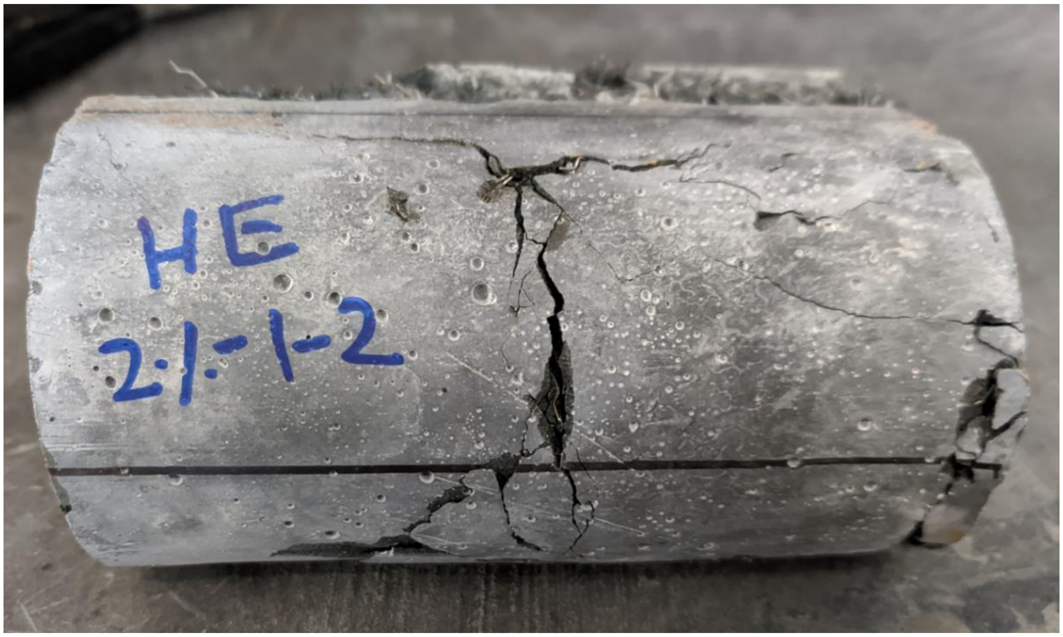

Figure 64. A typical specimen showing cracks running perpendicular to the line of loading alongside the specimen periphery.

4.5.2 Stress-Strain Response

Figure 65 presents the lateral stress-strain responses captured during the splitting-tensile strength tests of J3 concrete specimens with HE fibers. The lateral strain value was calculated using lateral deflection across the 1 in. gauge length, which did not capture the crack development outside that gauge length. For the HE-1% specimens, the discontinuity between the linear-elastic and post-cracking zone is significant. The first-cracking point can be clearly identified for the HE-1% specimens. However, with increasing fiber volume fractions, this change in slope of the stress-lateral strain curve at the point of first cracking is less distinctive. A change in the splitting-tensile stress can still be identified in the responses of HE-2% specimens at the point of first-cracking, though this portion is less significant than for the HE-1% specimens. This is due to the number of fibers resisting tensile stress and limiting load drop. As HE-4% specimens had a significantly higher number of fibers crossing the cracked faces, sudden load drops were not observed at the point of first crack. The first-cracking points for the HE-4% specimens were instead identified by determining the location of change in the slope of stress-lateral strain graphs. Strain-hardening behavior can be observed for all the specimens after cracking, which is the normal post-cracking response of UHPC in tension. Observing increased area under stress-strain curves presented in Figure 65, it can be stated that the energy absorption capacity increases with the increase in fiber volume fractions. However, these observed post-cracking behaviors are not actual tensile post-cracking behavior, as compression parallel to the cracks artificially inflates the post-cracking stress-strain response during splitting-tensile tests of UHPC [44].

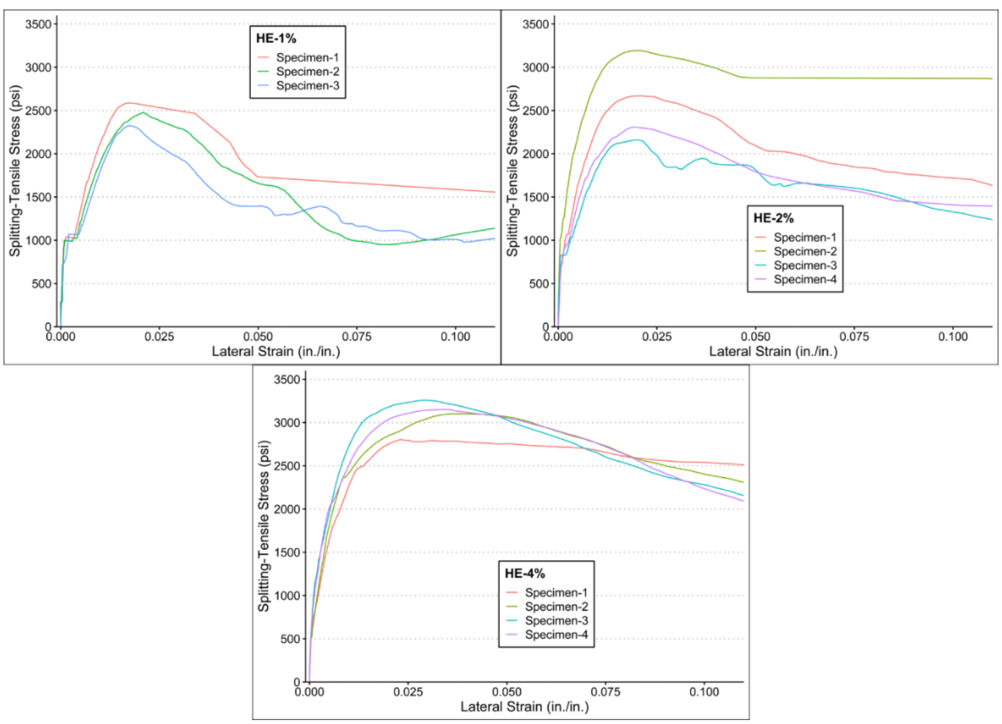

Figure 65. Splitting tensile stress-lateral strain response graphs for all J3 specimens with HE fibers.

Table 7 presents the summarized results observed from the stress-lateral strain behavior of J3 specimens with HE fibers. The HE-1% and HE-2% specimens showed identical average first-cracking strength and the HE-4% specimens showed lower average first-cracking strength. It can be summarized that fiber volume fractions were observed to have little to no impact on the first-cracking strength. It can be observed that cracks formed at much lower deflection for the HE-4% specimens than for the HE-1% and HE-2% specimens, as the HE-4% specimens had higher stiffness due to increased number of fibers. The HE-1% and HE-2% specimens showed similar deflection at the first-cracking point indicating similar uncracked concrete stiffness. As post-cracking response is a factor of fiber efficiency, increased apparent post-cracking peak strength was observed with increasing fiber volume fractions.

Table 7. Splitting tensile test results of all J3 specimens with hooked-end fibers.

Hooked-End Fiber Volume	Number of Specimens	First Cracking Strength, ksi		Transverse Deformation at First Cracking, inch		Apparent Peak Strength, ksi	
		Mean	Std. Dev.	Mean	Std. Dev	Mean	Std. Dev.
1%	3	1.03	0.036	0.0014	0.0006	2.43	0.132
2%	4	1.03	0.192	0.002	0.0005	2.58	0.460
4%	4	0.78	0.240	0.00083	0.0003	3.08	0.195

4.6 Freeze-Thaw (F-T) Resistance of J3 Concrete

This section summarizes the results of rapid freezing and thawing on pre-cracked and uncracked J3 concrete specimens with 1% and 2% HE fiber volume fractions. Damage was evaluated by measuring resonant frequency after specific numbers of cycles and flexural responses after the completion of 350 rapid freeze-thaw cycles and by comparing masses of the specimens before and after exposure. While displaying results, the pre-cracked specimens are referred as CR-1 and CR-2 and the uncracked specimens as UC-1 and UC-2 for each fiber content.

4.6.1 Crack Generation in the Intended Specimens

Table 8 presents a summary of the applied loads and deflections of the cracked specimens during flexural loading before starting the freeze-thaw test. Except HE-2% CR-2 all the specimens showed higher strength than average first-cracking strength shown by control specimens tested at 56 days. Though the control specimens and freeze-thaw specimens were not cast from same batch, average first cracking strength shows that the specimens shared almost the same matrix properties. Loading was intended to continue till the first load drop indicated by the loading machine. However, the actual loading was continued slightly after the first load-drop and the final vertical deflections were around 0.0075 in. for all the pre-cracked specimens.

Table 8. Observed strengths and deflections during pre-cracking samples before the freeze-thaw tests.

Fiber Content	Specimen	Stress at First Crack, psi	Vertical Deflection at First Crack, inch	Ratio of Strength to the Average First-Cracking Strength at 56 Days
HE-1%	CR-1	1320	0.0043	1.16
	CR-2	1180	0.0045	1.03
HE-2%	CR-1	1440	0.0044	1.05
	CR-2	1165	0.0048	0.85

After completion of the loading, the specimens were visually inspected to find the generated cracks. Figure 66 and Figure 67 depict the generated cracks in two HE-1% specimens and one HE-2% specimen. Though the cracks in the HE-1% specimens were clearly visible in the pictures, the cracks in the HE-2% specimens were too narrow to clearly capture in a photograph with the available equipment but were identified by visual inspection.

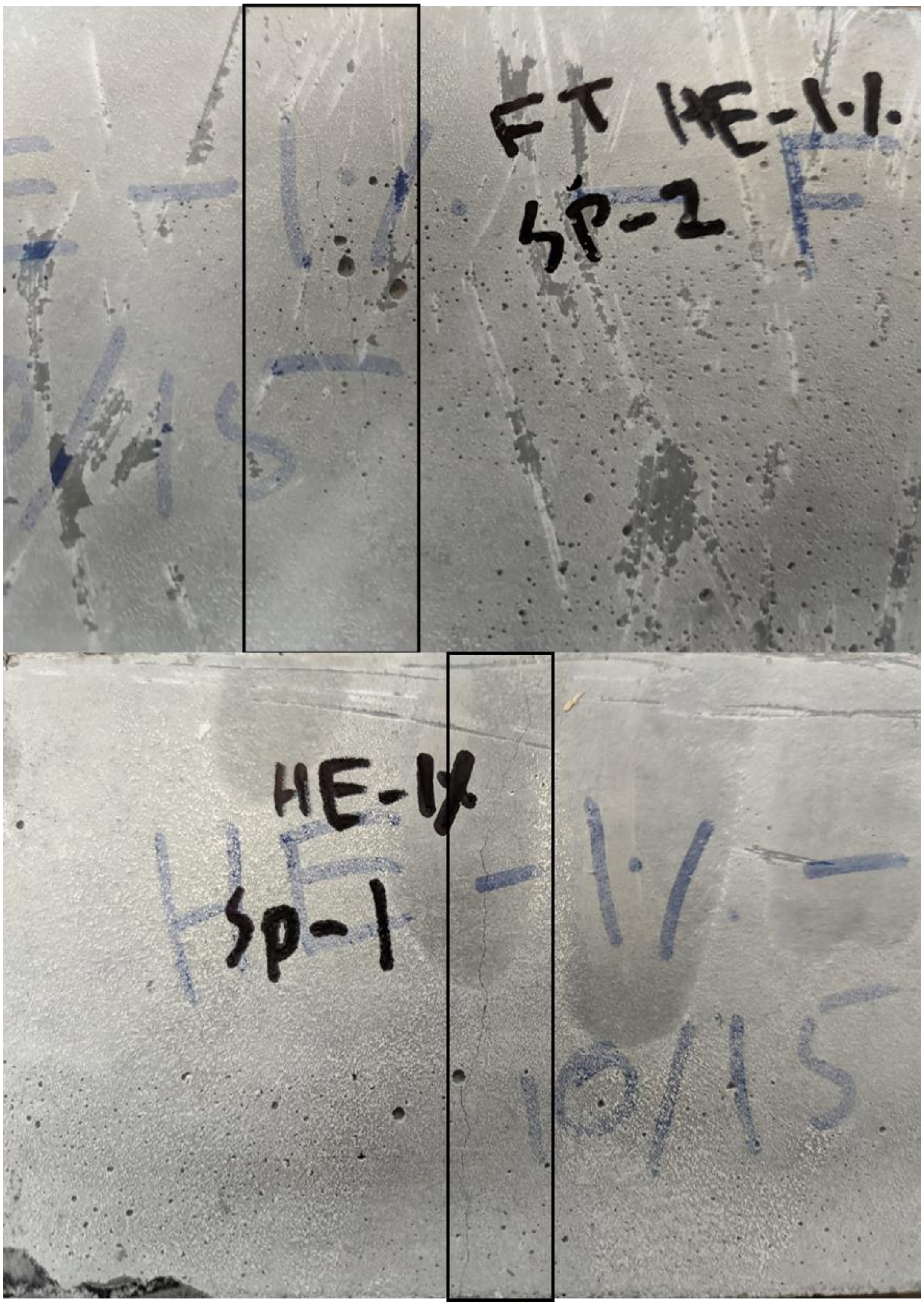

Figure 66. Generated hairline cracks in the HE-1% specimens.

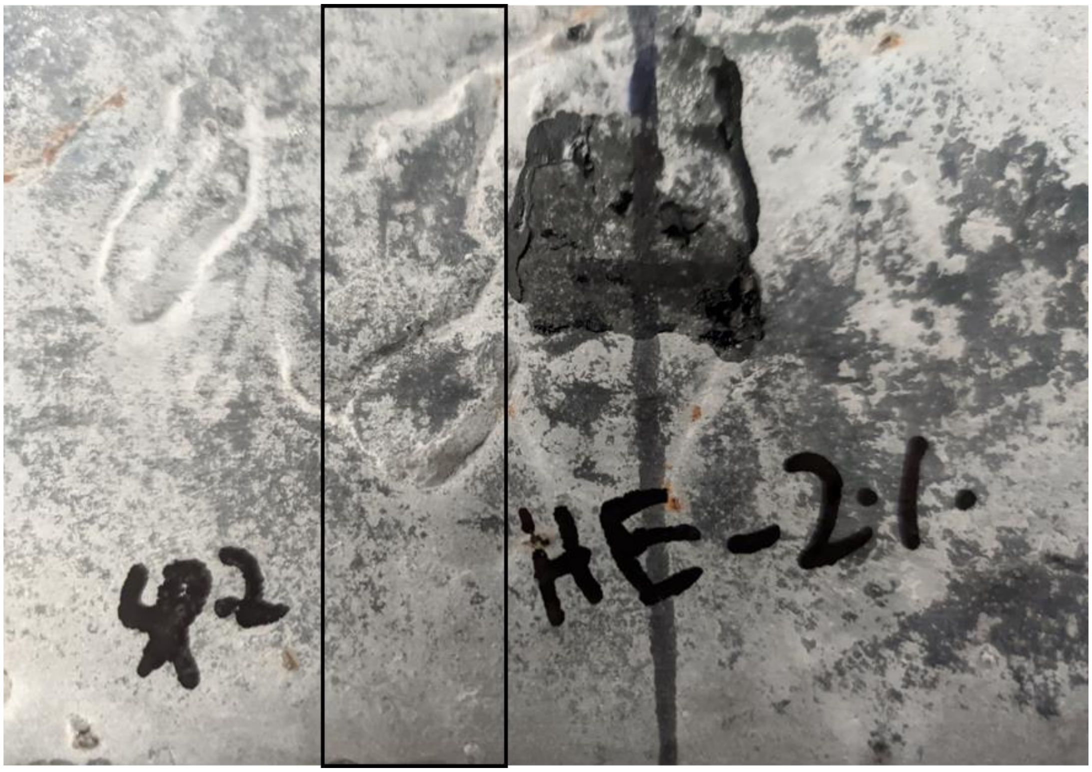

Figure 67. Generated hairline cracks in the HE-2% specimens.

4.6.2 Impact of Freeze-Thaw Cycles on the Specimens

Resonant frequency and weight of the specimens were measured periodically after specific numbers of cycles to track impacts of rapid freezing and thawing on the specimens. Figure 68 presents the resonant frequencies for both pre-cracked and uncracked HE-1% and HE-2% specimens throughout testing. Uncracked specimens with both fiber volume fractions showed almost identical resonant frequencies throughout the 352 freeze-thaw cycles. This observation indicated that, fiber volume fraction had no impact on the resonant frequency of the J3 concrete, and rapid freezing and thawing cycles did not generate any internal damage to impede the passing vibration. Due to the presence of cracks, pre-cracked specimens with both fiber volume fractions showed lower resonant frequency than the uncracked specimens throughout testing. As the pre-cracked HE-1% specimens had noticeably larger cracks than the pre-cracked HE-2% specimens, the pre-cracked HE-1% specimens showed lower resonant frequency at the start of the test. This observation indicates that fiber volume fraction can lower the damage induced in the cracked matrix, even if all the specimens showed similar vertical deflection during loading. The resonant frequencies of the pre-cracked specimens increased to a certain degree during freeze-thaw cycles, which indicate some healing of the cracks as water could reach unhydrated cement through cracks and continue hydration. After the completion of the test, all the pre-cracked and uncracked specimens showed almost identical resonant frequencies.

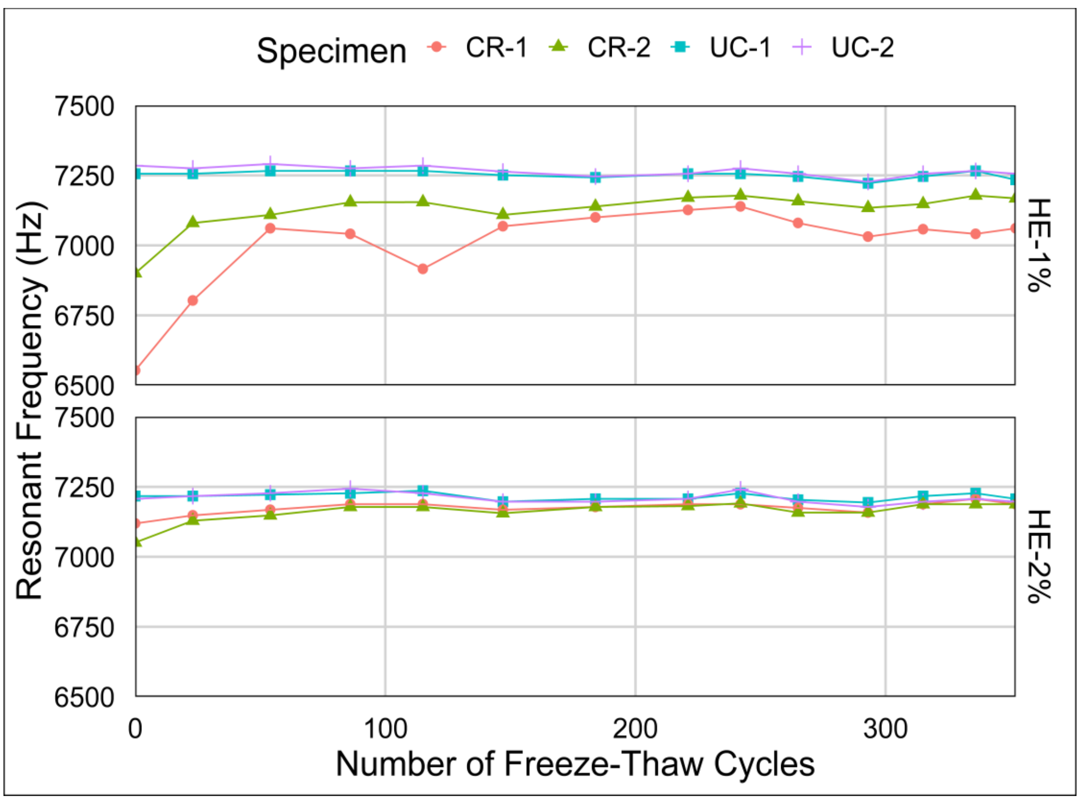

Figure 68. Average resonant frequency throughout the freeze-thaw test.

Figure 69 shows the change in dynamic modulus with increasing freeze-thaw cycles normalized against the values measured before the specimens went through rapid freezing and thawing cycles. The HE-1% pre-cracked specimens showed 8% and 4% increases and the HE-2% pre-cracked specimens showed 1% and 2% increases in dynamic modulus. For the HE-1% pre-cracked specimens, the majority of the increase occurred before completion of 54 cycles and for the HE-2% pre-cracked specimens, before completion of 23 cycles. Values stayed almost identical after that with minor changes. No uncracked specimen showed a measurable change in the dynamic modulus throughout the entire 352 rapid freezing and thawing cycles.

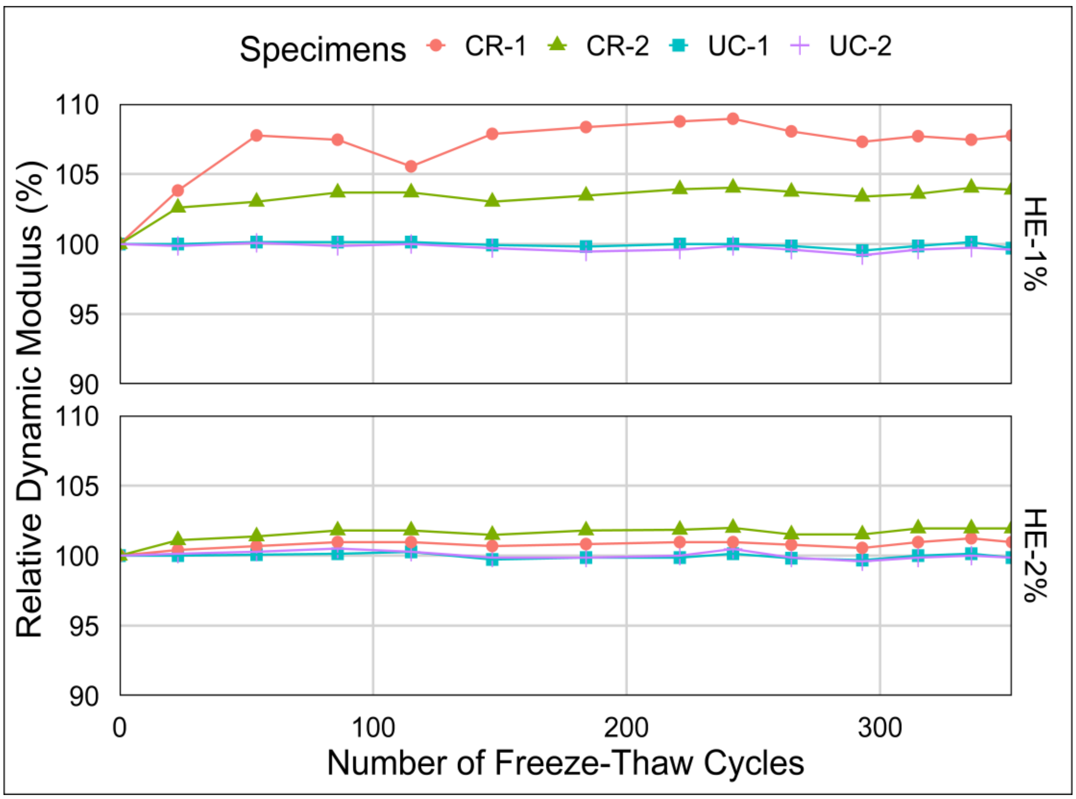

Figure 69. Relative dynamic modulus (normalized against the value at 0 cycle) throughout the freeze-thaw test.

Figure 70 presents the changes in masses of the HE-1% and HE-2% specimens with respect to the initial weights throughout the entire freeze-thaw test. Minor changes in weight were observed in the specimens, mostly due to minor chipping of the specimens along the top edges and opening of pores in the surfaces. The HE-1% specimens showed a maximum decrease of 0.01 lb and the HE-2% specimens showed a maximum decrease of 0.02 lb at any point of the test. However, after the completion of the test, specimens HE-1% CR-1 and CR-2 showed an overall increase and specimens UC-1 and UC-2 showed an overall decrease in weight. All the HE-2% specimens except UC-2 showed an overall increase in weight after the completion of the tests.

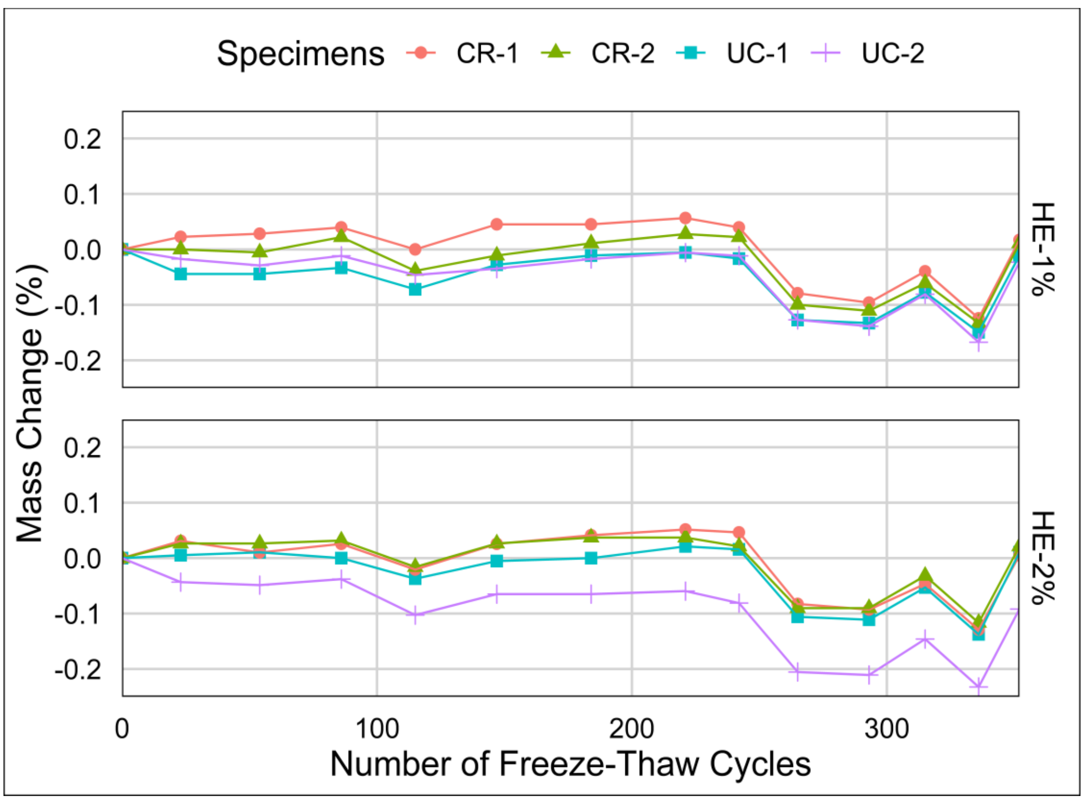

Figure 70. Change in mass associated with freeze-thaw cycles.

Figure 71 and Figure 72 present the HE-1% and HE-2% specimens after completion of the 352 cycles of the rapid freeze-thaw test. A crack gauge was used to identify crack widths in the pre-cracked specimens though it was an unsuccessful attempt. The cracks in all the pre-cracked specimens could not be identified by visual inspection after completion of freezing and thawing cycles because of reduction in crack widths due to the combination of hydration of unhydrated cement paste and generation of pores in the concrete surfaces. Alongside opening of pores, the damage in the specimens was observed as chipping along the edges and rusting of exposed fibers.

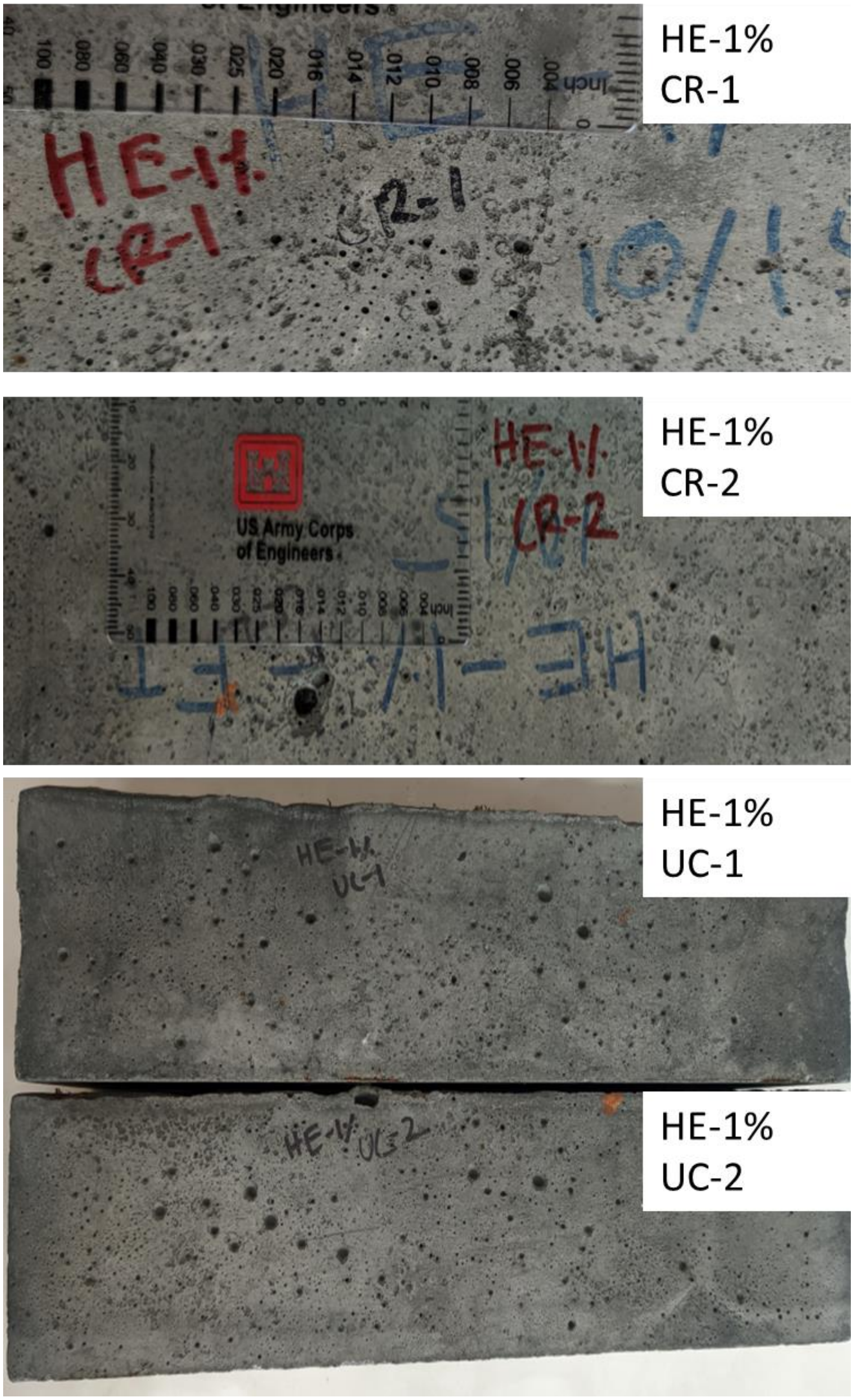

Figure 71. HE-1% specimens after completion of freeze-thaw testing.

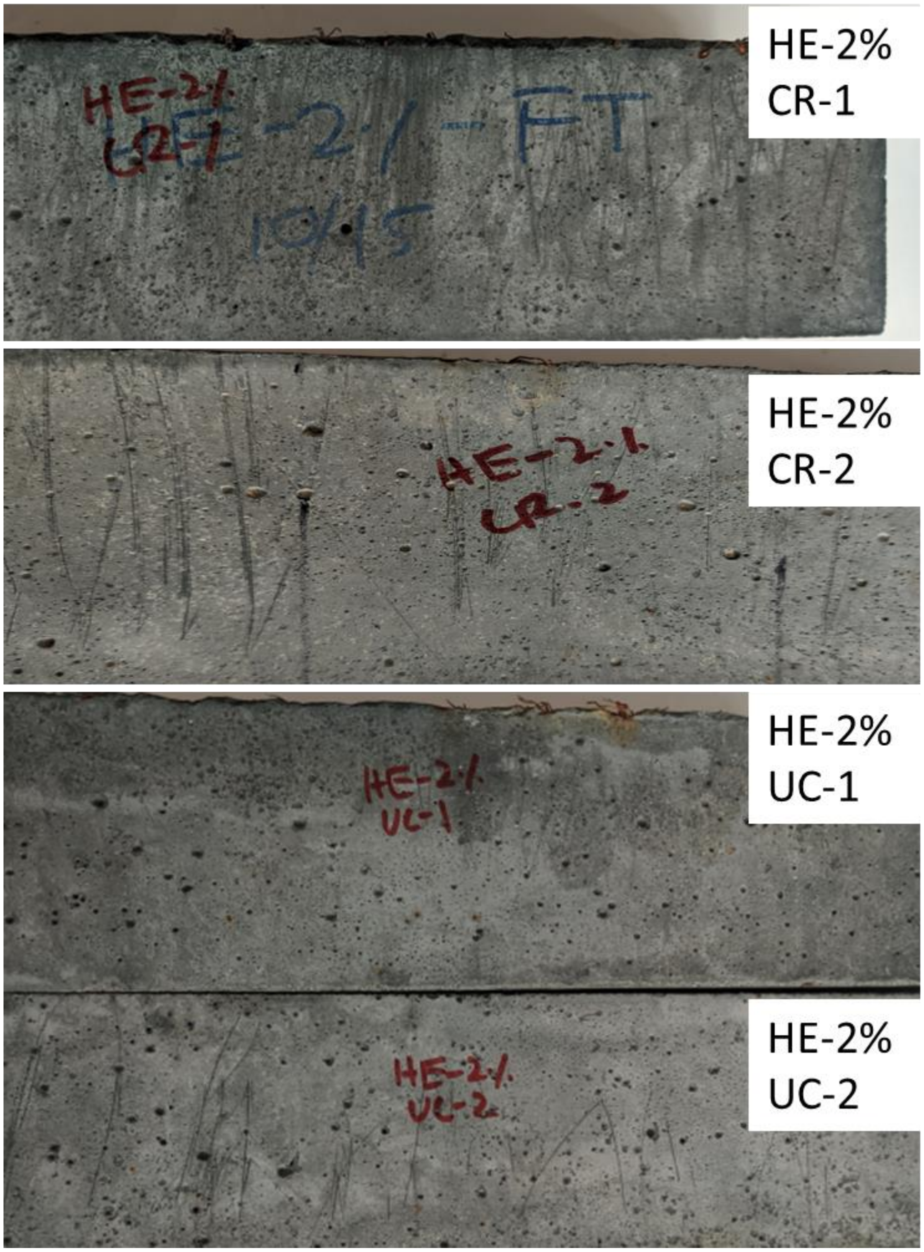

Figure 72. HE-2% specimens after completion of freeze-thaw testing.

4.6.3 Flexural Capacity of the Specimens after Freeze-Thaw Testing

After the completion of rapid freeze-thaw testing, all the specimens were loaded to measure residual flexural capacity (modulus of rupture) and the results were compared to the average strengths observed at the limit of proportionality (LOP) and modulus of rupture (MOR) for 56 days test flexural specimens described in section 4.3.3.2. Figure 73 and Figure 74 present the specimens after flexural test. All specimens showed similar random crack patterns to the base specimens tested at 56 days of age. Developed cracks were wider in the HE-1% specimens, which could be due to the higher number of fibers in the HE-2% specimens bridging the cracks. Specimen HE-1% UC-2 developed the major crack outside middle third zone, however the crack was outside of the middle third by no more than 5% of the span length so a correction was made according to ASTM C78 [70]. Specimen HE-1% CR-1 developed a minor crack outside of the middle third by more than 5% of the span length, however, the controlling fracture was in the middle third zone. Specimens HE-2% UC-1 and UC-2 developed major cracks at the boundary of the middle third zone.

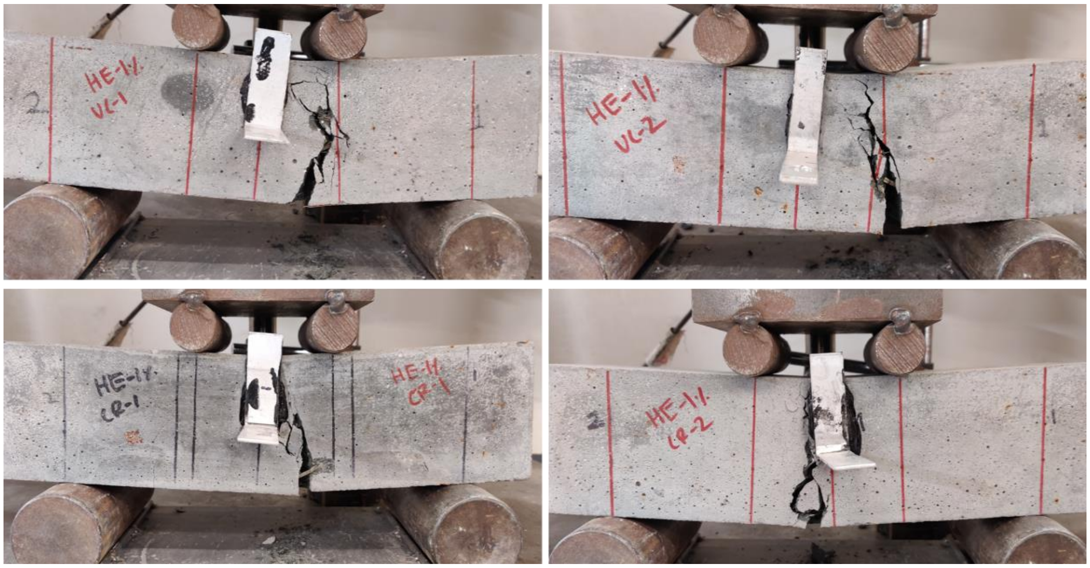

Figure 73. Cracks due to flexural testing for the HE-1% specimens exposed to rapid freezing and thawing.

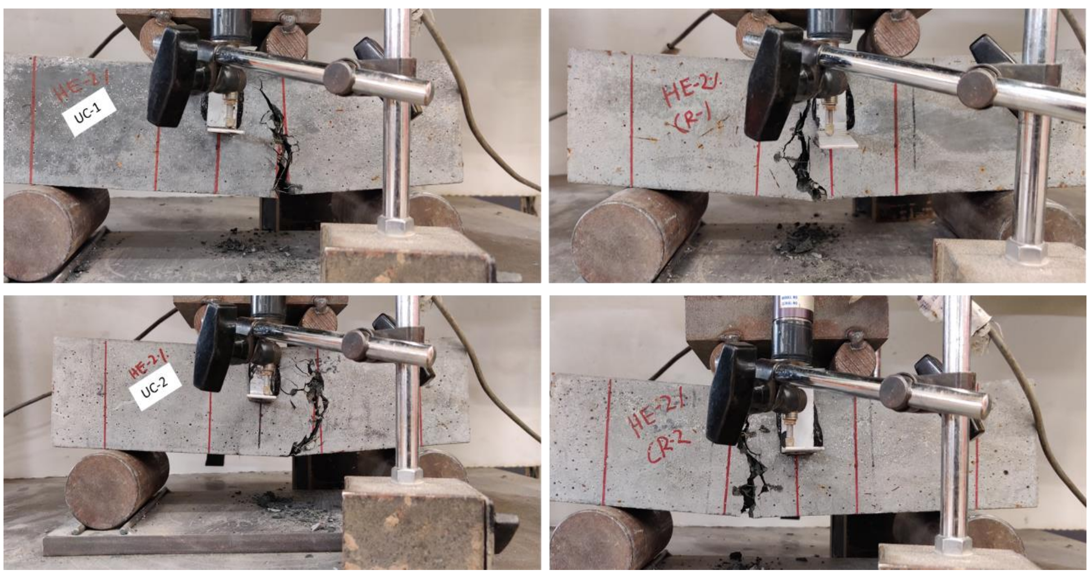

Figure 74. Cracks due to flexural testing for the HE-2% specimens exposed to rapid freezing and thawing.

Figure 75 presents the load-vertical deflection graphs for flexural tests of HE-1% and HE-2% specimens after completion of the freeze-thaw test. Like the base specimens under flexural loading at 56 days, specimens exposed to freeze-thaw showed linear-elastic, fiber-activation, and fiber-pullout phases. Linear-elastic behavior prior to pre-cracking similar to that of uncracked specimens was observed from pre-cracked specimens, which indicated healing of the prior cracks during exposure to freezing and thawing. Expect for specimen HE-1% UC-1, all the specimens showed deflection-hardening behavior during the fiber-activation stage. The load-deflection graphs were used to identify first-cracking strength and modulus of rupture to compare with the base specimens. As depicted in Figure 34, specimens exposed to the freeze-thaw test also showed deflection at the start of the flexural test due to roller settlement and chipping, which was subtracted to get the actual deflection at LOP and MOR.

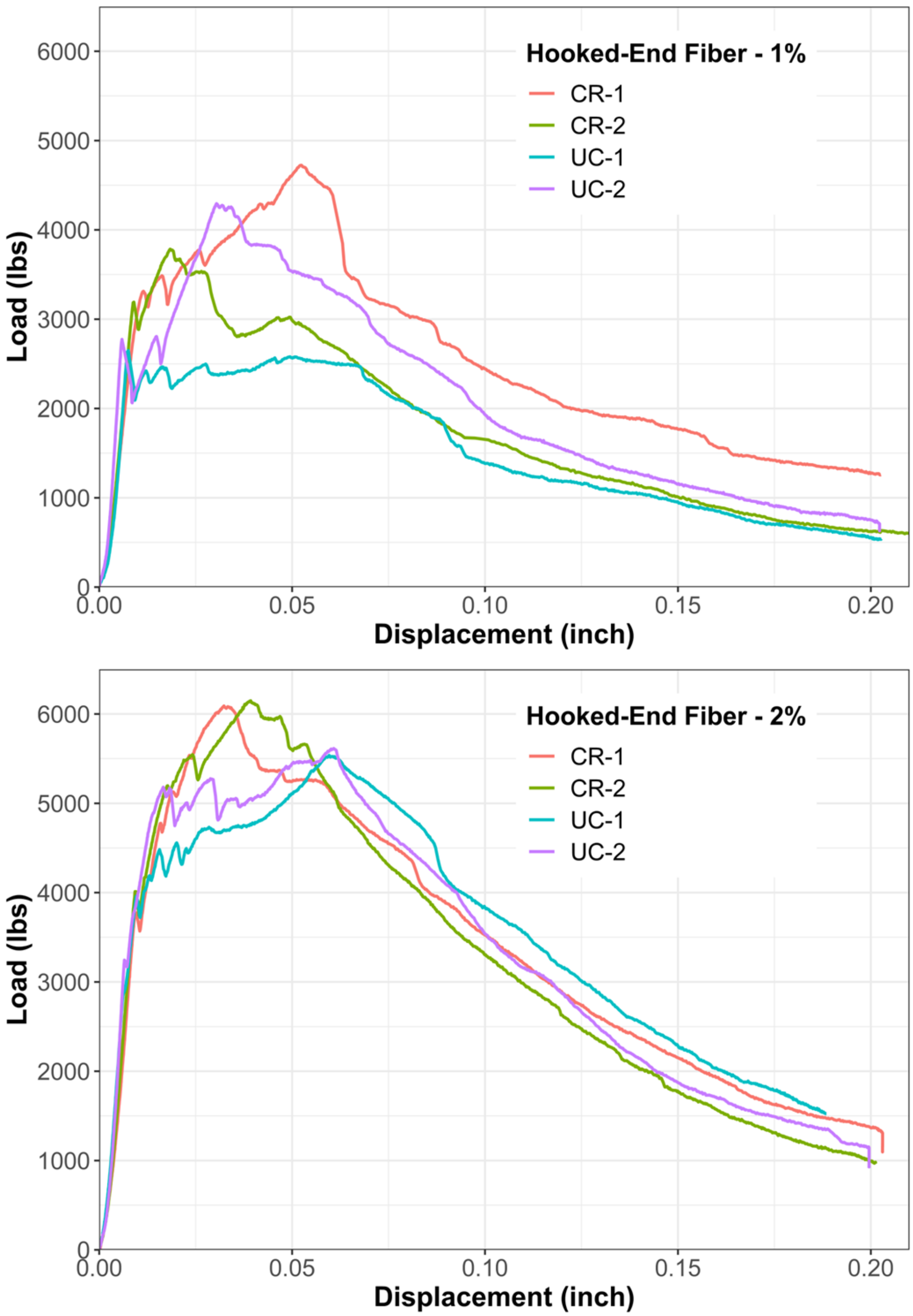

Figure 75. Load-deflection response of specimens subjected to rapid freeze-thaw test.

Table 9 summarizes the flexural performance of freeze-thaw specimens at the first-cracking or limit of proportionality (LOP) point. Comparing to strength and deflection at the beginning of freeze-thaw tests (Table 8), pre-cracked HE-1% and HE-2% specimens showed higher deflection at LOP under flexure after freeze-thaw test due to pre-existing crack, which was easier to stretch. Except HE-2% CR-2, all the cracked specimens showed less strength compared to when these were cracked at the start of the freeze-thaw test. These comparisons can state the fact that though resonant-frequency indicated that the section properties increased with the freeze-thaw cycles, however, presence of pre-existing cracks made it difficult to restore actual flexural capacity. Also, after the formation of a crack, the presence of fibers influence concrete stiffness at much higher degree than in the linear-elastic stage, which can be a reason why HE-2% CR-2 showed higher strength at LOP after exposure to freezing and thawing than what was observed at the start of the freeze-thaw test.

Also, both the pre-cracked and uncracked HE-1% specimens showed less strength compared to the base specimens with as much as a 22% difference. However, comparing between HE-1% specimens, it could be observed that cracked specimens showed higher strength and deflection at LOP than uncracked specimens. This could be due to the pre-cracked specimens showing pseudo linear-elastic behavior as they were already exposed to cracks. Unlike resonant frequency, the flexural strength test showed significant damage in concrete matrix in the HE-1% uncracked specimens. As first-cracking strength is primarily a property of concrete matrix rather than fiber-efficiency, it can be inferred that exposure to rapid freeze-thaw cycles deteriorated concrete properties, even though measured resonant frequency did not show any reduction. Flexural tests induce tension on the extreme edge surface of the concrete. Significant development of pores was observed on the specimen faces after the freeze-thaw test, which could indicate that the quality of the surrounding concrete deteriorated after exposure to freezing and thawing cycles. This can at least partially explain the decrease in first-cracking strength after the freeze-thaw test.

Similar conclusions can also be made for the difference in strength and deflection of the pre-cracked and uncracked HE-2% specimens at LOP. Uncracked HE-2% specimens showed lower strength and deflection at LOP than pre-cracked HE-2% specimens. The results at LOP shows that freeze-thaw test made almost identical damage in the specimen surfaces and deteriorated concrete matrix to an extent that it lost some of the stiffness and bending strength.

Table 9. Summary of freeze-thaw specimen flexural performance at the limit of proportionality point.

Fiber Content	Specimen	Strength, f_{LOP} (psi)	Deflection, δ_{LOP} (in.)	Ratio of Strength to the Average First-Cracking Strength at 56 Days
HE-1%	CR-1	1110	0.0083	0.97
	CR-2	1070	0.0056	0.94
	UC-1	890	0.0044	0.78
	UC-2	935	0.0037	0.82
HE-2%	CR-1	1275	0.0072	0.93
	CR-2	1350	0.0066	0.98
	UC-1	975	0.0036	0.71
	UC-2	1105	0.0037	0.81

Table 10 summarizes the performance of freeze-thaw specimens at the modulus of rupture (ultimate strength) point. Like the first-cracking strength, the HE-1% and HE-2% specimens exposed to freezing and thawing showed significantly less post-cracking peak strength than the base specimens. Post-cracking peak behavior mostly depends on the efficiency of fibers to bridge cracks and redistribute stress. However, hooked-end fiber specimens fail due to breaking of the surrounding concrete matrix rather than fiber pull-out due to superior bond between the fiber and surrounding concrete. As observed from the first-cracking behavior that freeze-thaw test can deteriorate the surface concrete; it is reasonable that the concrete near the surface cannot resist the damage done by hooked-end fibers during the fiber bridging stage. As the fibers prevent damage in the concrete matrix, observed better performance of pre-cracked specimens at LOP diminished at post-cracking peak strength.

Table 10. Summary of freeze-thaw specimen flexural performance at the modulus of rupture point.

Fiber Content	Specimen	Strength, f_{MOR} (psi)	Deflection, δ_{MOR} (in.)	Ratio of Strength to the Average Maximum Strength at 56 Days
HE-1%	CR-1	1580	0.049	0.75
	CR-2	1270	0.015	0.60
	UC-1	870	0.046	0.41
	UC-2	1440	0.028	0.68
HE-2%	CR-1	2045	0.030	0.61
	CR-2	2060	0.036	0.61
	UC-1	1860	0.057	0.55
	UC-2	1895	0.058	0.56

4.7 Girder Repair using UHPC

4.7.1 Initial Testing of the Girder

The undamaged prestressed beam was loaded until deck crushing was observed, taken as failure. Initial cracking was observed at 45 kips of load in the form of shear cracks accompanied by measured strand slip. The maximum load at the point of deck crushing was 54.5 kips corresponding to a deflection of 0.94 in. Figure 76 shows the girder after the initial test with shear cracks visible. The observed cracking, strand slip, and load-deflection behavior indicated a bond-shear type failure.

Figure 76. Girder with cracks after initial load test.

4.7.2 Testing of the Repaired Girder

The compressive strength of the ST-2% mix used to repair the girder was 19.8 ksi on the test day, which was much higher than the initial strength of the girder. The first crack observed for the repaired beam was a flexural crack that appeared at 35 kips of load and was accompanied by strand slip. The initial cracking load was less for the repaired girder. However, the maximum load was 83 kips, which was much higher than for the test of the undamaged girder. Failure was considered to have occurred at the point of deck crushing and the failure mechanism of the repaired girder was bond-flexural failure. Figure 77 shows the repaired girder with flexural cracks visible in the girder and no cracks visible in the repair. The final deflection of the repaired girder under maximum load was 1.5 in. and after releasing of the load, the repaired beam was able to recover 0.625 in. of deflection.

Figure 77. Repaired girder with cracks after loading to failure.

4.7.3 Load vs Deflection Curves for Girder

Figure 78 presents the load vs deflection curves for both the initial and repaired girder tests. Though the initial beam required a higher load to initiate cracking, it exhibited a relatively constant load with increased deflection, resulting from shear cracking and strand slip. Though the repaired girder showed cracks at smaller load, these cracks were flexural in nature and the girder sustained a much higher ultimate load. The repaired girder showed steeper slopes for the pre and post crack portions of the curves which indicates an increased stiffness after repair. The results suggest that UHPC jacketing was able to restore the shear capacity of the girder and change the controlling failure mechanism. No cracks were observed in the repair material indicating that the UHPC jacket created a near impermeable layer that could protect the damaged region from further deterioration in addition to increasing capacity of the end region.

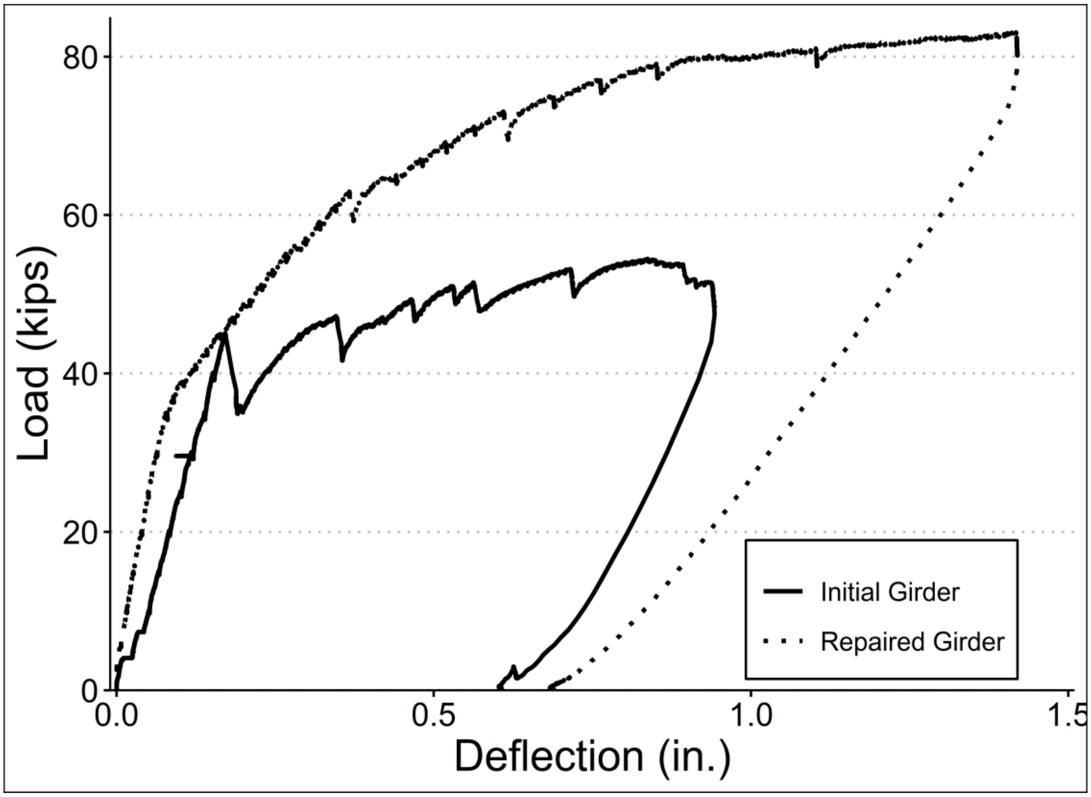

Figure 78. Load-deflection graphs for both the initial and repaired girder tests.

Chapter 5 Summary, Conclusions and Recommendations

5.1 Summary

Measurement of mechanical response and durability of J3 concrete with varying fiber contents of straight steel (ST) microfibers and long hooked-end (HE) fibers were the major objectives of this study. Compressive response, stiffness, tensile strength, and flexural strength emphasizing the limit of proportionality and modulus of rupture were the concrete properties investigated in this study. Freeze-thaw durability of J3 specimens having pre-existing cracks was also a focus of this experimental program. Alongside these, the efficacy of J3 concrete to restore shear capacity of the end region of a prestressed concrete bridge girder was examined.

Previous research works containing those above-mentioned tests were studied (Chapter 2) to develop an understanding of general UHPC behaviors. However, the fibers used in those studies are no longer available and specimens having 1%, 2%, 4%, and 6% straight micro-fibers from a new source and 1%, 2%, and 4% long hooked-end fibers were considered for this study to quantify the effect of different fibers on J3 properties. The uniaxial compression test, direct tensile test, third point bending test and splitting tensile strength were the experimental tests used in this study to identify mechanical response. A total of 352 rapid freezing and thawing cycles were performed on pre-cracked and uncracked specimens with 1% and 2% HE fiber volumes. Periodic resonant frequency and weight measurements, and residual flexural capacity of the specimens after completion of the freeze-thaw test were measured to quantify the damage due to rapid freeze-thaw cycles. J3 concrete with 2% straight fibers from the new source was used to repair the end region of a concrete girder having shear cracks to restore shear capacity of the girder. The approach and methodology section (Chapter 3) of this thesis provides the details regarding specimen fabrication and experimental test setups noting the additional necessary adaptations to the standards in order to fit the available equipment. The observations made from this experimental program are reported and discussed in the results and discussion section (Chapter 4).

5.2 Conclusions

From the limited numbers of tests done in this study, the following conclusions are drawn which best describe the behaviors of the J3 concrete under similar conditions.

- For the same volume fractions, hooked-end fibers impose more restrictions on the free flow of the concrete mix. Increasing HRWR has positive impact on the flow, however, it also increases the probability of segregation of the mix and generates air voids. Fiber volume fractions of 4% and 6% create clumps of fibers in the middle of the flow which negatively impacts the proper distribution of fibers in the molds leading to less fiber efficiency. Also, it was not possible to create an HE-6% mix.
- Increasing the number of straight microfibers in J3 concrete mixes in the range of 1%-6% fiber volume fractions did not bring positive impacts on compressive strength properties in this research.
- Regardless of fiber volume and type, uniaxial compressive stress-strain responses showed an almost linear elastic portion till first peak-strength,

sudden load drop after first peak-strength to second peak-strength, then gradual stress softening behavior due to fiber bridging and crack widening or localization. The second peak-strength and crack localization behavior showed dependency on the fiber volume fraction of the mix.

- Specimens in the third point bending test showed linear-elastic behavior in the uncracked stage, a fiber activation stage, and fiber pullout behavior. Almost all the specimens showed deflection hardening behavior in the fiber activation zone. Fiber types and volume fractions showed little influence on the average deflections at first crack and peak strength. Fiber volume showed an influence on both first-cracking strength and peak strength of J3 specimens. Fiber types showed minimal influence on first-cracking strength, however peak-strength and toughness of specimens were significantly influenced by fiber type. Fiber type also influenced the failure mode during the fiber pull-out stage, where straight fiber specimens failed due to fibers pulling out of the concrete matrix and hooked-end fiber specimens failed due to breaking of the concrete matrix surrounding the generated cracks.
- Specimens tested in uniaxial tension showed stress-strain responses which could be divided into linear-elastic, multi-cracking, crack-sustaining, and crack-localization stages. Except for the ST-1% specimens, HE-1% specimens, and one ST-4% specimen, every

specimen showed strain hardening behavior during the multi-cracking and crack-sustaining phases. Specimens with straight microfibers showed bending stress at the moment of first-cracking and the specimens with hooked-end fibers showed bending beyond the first-cracking point. Uneven distribution of fibers between different surfaces was observed at the location of fracture which could be the reason behind this behavior. This bending stress affected the maximum uniaxial tensile stress and made it difficult to summarize the effect of fiber volume and type on the peak tensile stress. Among all the specimens tested, the HE-1% and ST-1% specimens showed higher average first-cracking strength.

- Splitting tensile strength tests performed on hooked-end specimens showed linear elastic behavior until first crack and then strain hardening behavior, which was a combination of fiber bridging and compression of the specimens' surface where load was being applied. The distinctions between linear-elastic behavior and post-cracking response were reduced with higher fiber volume fractions. The HE-1% and HE-2% specimens showed identical first cracking strength (the true measurement of splitting tensile strength), where HE-4% showed a lower value. However, the apparent peak strength increased with fiber volume fractions because of fiber bridging, which is not an exact measure of post-cracking peak-response.

- Pre-cracked specimens were able to regain the lost resonant frequency over the course of freeze-thaw cycles, and at the end of the freeze-thaw test both pre-cracked and uncracked specimens had the same resonant frequency. The test indicated that fiber volume fraction did not influence the resonant frequency of specimens, freeze-thaw cycles did not degrade the resonance frequency of the specimens, and J3 concrete was able to heal cracks in suitable conditions. While measuring the residual flexural capacity of the specimens, fiber volume showed minimal influence on strength at limit of proportionality and peak-strength. Though resonant frequency did not measure any degradation in the specimens, the flexural strength test identified reduced strength potentially due to damage of the concrete at the specimen surface. The HE-1% specimens showed ratios of 0.87 and 0.61, and HE-2% specimens showed ratios of 0.64 and 0.58 of the first-cracking and peak-strength of the base HE-1% and HE-2% specimens.
- J3 jacketing was shown to be an efficient method to restore the shear capacity of a pre-damaged prestressed concrete girder. J3 jacketing significantly increased the maximum sustained load of the girder from 54.5 kips to 83 kips and changed the controlling failure mechanism from bond-shear cracks to bond-flexural cracks. Also, it provided an impermeable layer for water ingress and superior stiffness.

5.3 Recommendations

Based on the observed J3 concrete behavior under different tests for this experimental program, the following recommendations are suggested:

- Except for cases of strict tensile demand, fiber volume should not be above 2% as it will pose significant difficulties in achieving workability and homogenous fiber distribution. A 4% fiber volume can be used for cases where higher tensile capacity is required. The dimension of hooked-end fibers makes it difficult to place in slender molds. However, in proper sized molds, hooked-end fibers can provide higher energy absorption capacity than straight microfibers.
- For capturing axial compressive stress-strain behavior, the setup used in this experiment was not reliable as the LVDTs picked up deflections of multiple parts of the test setup which were difficult to subtract from the data. A better test setup should be used where gauge length is equal to the length of the specimens.
- Slender direct tensile specimens pose significant drawbacks when cast with relatively higher size and amount of fibers to represent the fiber distribution found in actual large-scale structures [43]. To get proper representative samples, a slender section from a large block could be cut to measure the direct tensile response. The LVDTs should also be attached to the specific face of the specimens to get deflection values in case bending is present at one moment in the test.

- Future freeze-thaw specimens should have more and larger cracks to see whether volume increase of water in the cracks during freezing can actually damage the specimens.

Chapter 6 References

[1] E. Fehling, M. Schmidt, J. C. Walraven, T. Leutbecher, and S. Fröhlich, *Ultra-High Performance Concrete UHPC: Fundamentals, Design, Examples*, First Edit. Berlin, Germany: Ernst & Sohn, 2014.

[2] B. Graybeal, E. Brühwiler, B.-S. Kim, F. Toutlemonde, Y. L. Voo, and A. Zaghi, "International Perspective on UHPC in Bridge Engineering," *J. Bridg. Eng.*, vol. 25, no. 11, p. 04020094, 2020, doi: 10.1061/(asce)be.1943-5592.0001630.

[3] B. A. Graybeal, *Design and Construction of Field-Cast UHPC Connections*. 2014.

[4] ACI Committee 239, *ACI 239R-18 Ultra-High-Performance Concrete: An Emerging Technology Report*. American Concrete Institution, 2018.

[5] B. A. Graybeal, "Development of Non-Proprietary Ultra-High Performance Concrete for Use in the Highway Bridge Sector: TechBrief," 2013.

[6] T. Looney, A. Mcdaniel, J. Volz, and R. Floyd, "Development and Characterization of Ultra-High Performance Concrete with Slag Cement for Use as Bridge Joint Material," *Br. J. Civ. Archit. Eng.*, vol. 01, no. 02, pp. 1–14, 2019.

[7] W. Meng, M. Valipour, and K. H. Khayat, "Optimization and performance of cost-effective ultra-high performance concrete," *Mater. Struct. Constr.*, vol. 50, no. 1, pp. 1–16, 2017, doi: 10.1617/s11527-016-0896-3.

[8] R. Zhong, K. Wille, and R. Viegas, "Material efficiency in the design of UHPC paste from a life cycle point of view," *Constr. Build. Mater.*, vol. 160, pp. 505–513, 2018, doi: 10.1016/j.conbuildmat.2017.11.049.

[9] M. Alkaysi and S. El-Tawil, "Effects of variations in the mix constituents of ultra high performance concrete (UHPC) on cost and performance," *Mater. Struct. Constr.*, vol. 49, no. 10, pp. 4185–4200, 2016, doi: 10.1617/s11527-015-0780-6.

[10] A. S. McDaniel, "DEVELOPMENT OF NON-PROPRIETARY ULTRA-HIGH-PERFORMANCE CONCRETE MIX DESIGNS.," University of Oklahoma, 2017.

[11] M. A. Bajaber and I. Y. Hakeem, "UHPC evolution, development, and utilization in construction: A review," *J. Mater. Res. Technol.*, vol. 10, pp. 1058–1074, 2021, doi: 10.1016/j.jmrt.2020.12.051.

[12] B. Nematollahi, "A review on ultra high performance 'ductile' concrete (UHPdC) technology," *Int. J. Civ. Struct. Eng.*, vol. 2, no. 3, 2012, doi: 10.6088/ijcser.00202030026.

[13] O. Mishra and S. P. Singh, "An overview of microstructural and material properties of ultra-high-performance concrete," *J. Sustain. Cem. Mater.*, vol. 8, no. 2, pp. 97–143, 2019, doi: 10.1080/21650373.2018.1564398.

[14] Z. Wu, C. Shi, and K. H. Khayat, "Investigation of mechanical properties and shrinkage of ultra-high performance concrete: Influence of steel fiber content and shape," *Compos. Part B Eng.*, vol. 174, no. May, p. 107021, 2019, doi: 10.1016/j.compositesb.2019.107021.

[15] A. Le Hoang and E. Fehling, "Influence of steel fiber content and aspect ratio on the uniaxial tensile and compressive behavior of ultra high performance concrete," *Constr. Build. Mater.*, vol. 153, no. November, pp. 790–806, 2017, doi: 10.1016/j.conbuildmat.2017.07.130.

[16] S. J. Barnett, J. F. Lataste, T. Parry, S. G. Millard, and M. N. Soutsos, "Assessment of fibre orientation in ultra high performance fibre reinforced concrete and its effect on flexural strength," *Mater. Struct. Constr.*, vol. 43, no. 7, pp. 1009–1023, 2010, doi: 10.1617/s11527-009-9562-3.

[17] S. T. Kang and J. K. Kim, "The relation between fiber orientation and tensile behavior

in an ultra high performance fiber reinforced cementitious composites (UHPFRCC)," *Cem. Concr. Res.*, vol. 41, no. 10, pp. 1001–1014, 2011, doi: 10.1016/j.cemconres.2011.05.009.

[18] K. Wille, D. J. Kim, and A. E. Naaman, "Strain-hardening UHP-FRC with low fiber contents," *Mater. Struct. Constr.*, vol. 44, no. 3, pp. 583–598, 2011, doi: 10.1617/s11527-010-9650-4.

[19] Z. Wu, C. Shi, W. He, and L. Wu, "Effects of steel fiber content and shape on mechanical properties of ultra high performance concrete," *Constr. Build. Mater.*, vol. 103, pp. 8–14, 2016, doi: 10.1016/j.conbuildmat.2015.11.028.

[20] M. A. Ibrahim, M. Farhat, M. A. Issa, and J. A. Hasse, "Effect of material constituents on mechanical & fracture mechanics properties of ultra-high-performance concrete," *ACI Struct. J.*, vol. 114, no. 3, pp. 453–465, 2017, doi: 10.14359/51689717.

[21] R. Wang and X. Gao, "Relationship between flowability, entrapped air content and strength of UHPC mixtures containing different dosage of steel fiber," *Appl. Sci.*, vol. 6, no. 8, 2016, doi: 10.3390/app6080216.

[22] A. Alsalman, C. N. Dang, and W. Micah Hale, "Development of ultra-high performance concrete with locally available materials," *Constr. Build. Mater.*, vol. 133, no. May 2018, pp. 135–145, 2017, doi: 10.1016/j.conbuildmat.2016.12.040.

[23] N. K. Lee, K. T. Koh, S. H. Park, and G. S. Ryu, "Microstructural investigation of calcium aluminate cement-based ultra-high performance concrete (UHPC) exposed to high temperatures," *Cem. Concr. Res.*, vol. 102, no. September, pp. 109–118, 2017, doi: 10.1016/j.cemconres.2017.09.004.

[24] S. Kazemi and A. S. Lubell, "Influence of Specimen Size and Fiber Content on Mechanical Properties of Ultra-High-Performance Fiber-Reinforced Concrete," *ACI*

Mater. J., vol. 109, no. 6, 2012, doi: 10.14359/51684165.

[25] M. Pourbaba, E. Asefi, H. Sadaghian, and A. Mirmiran, "Effect of age on the compressive strength of ultra-high-performance fiber-reinforced concrete," *Constr. Build. Mater.*, vol. 175, pp. 402–410, 2018, doi: 10.1016/j.conbuildmat.2018.04.203.

[26] J. Xue, B. Briseghella, F. Huang, C. Nuti, H. Tabatabai, and B. Chen, "Review of ultra-high performance concrete and its application in bridge engineering," *Constr. Build. Mater.*, vol. 260, p. 119844, 2020, doi: 10.1016/j.conbuildmat.2020.119844.

[27] W. Meng and K. H. Khayat, "Effect of Hybrid Fibers on Fresh Properties, Mechanical Properties, and Autogenous Shrinkage of Cost-Effective UHPC," *J. Mater. Civ. Eng.*, vol. 30, no. 4, p. 04018030, 2018, doi: 10.1061/(asce)mt.1943-5533.0002212.

[28] D. Y. Yoo, J. H. Lee, and Y. S. Yoon, "Effect of fiber content on mechanical and fracture properties of ultra high performance fiber reinforced cementitious composites," *Compos. Struct.*, vol. 106, pp. 742–753, 2013, doi: 10.1016/j.compstruct.2013.07.033.

[29] D. Y. Yoo, S. T. Kang, N. Banthia, and Y. S. Yoon, "Nonlinear finite element analysis of ultra-high-performance fiber-reinforced concrete beams," *Int. J. Damage Mech.*, vol. 26, no. 5, pp. 735–757, 2017, doi: 10.1177/1056789515612559.

[30] M. Shafieifar, M. Farzad, and A. Azizinamini, "Experimental and numerical study on mechanical properties of Ultra High Performance Concrete (UHPC)," *Constr. Build. Mater.*, vol. 156, pp. 402–411, 2017, doi: 10.1016/j.conbuildmat.2017.08.170.

[31] J. J. Park, D. Y. Yoo, G. J. Park, and S. W. Kim, "Feasibility of reducing the fiber content in ultra-high-performance fiber-reinforced concrete under flexure," *Materials (Basel).*, vol. 10, no. 2, 2017, doi: 10.3390/ma10020118.

[32] S. Abbas, A. M. Soliman, and M. L. Nehdi, "Exploring mechanical and durability properties of ultra-high performance concrete incorporating various steel fiber lengths

and dosages," *Constr. Build. Mater.*, vol. 75, pp. 429–441, 2015, doi: 10.1016/j.conbuildmat.2014.11.017.

[33] D. Y. Yoo, S. Kim, G. J. Park, J. J. Park, and S. W. Kim, "Effects of fiber shape, aspect ratio, and volume fraction on flexural behavior of ultra-high-performance fiber-reinforced cement composites," *Compos. Struct.*, vol. 174, pp. 375–388, 2017, doi: 10.1016/j.compstruct.2017.04.069.

[34] L. Zhang, J. Liu, J. Liu, Q. Zhang, and F. Han, "Effect of Steel Fiber on Flexural Toughness and Fracture Mechanics Behavior of Ultrahigh-Performance Concrete with Coarse Aggregate," *J. Mater. Civ. Eng.*, vol. 30, no. 12, p. 04018323, 2018, doi: 10.1061/(asce)mt.1943-5533.0002519.

[35] D. Y. Yoo, M. J. Kim, S. W. Kim, and J. J. Park, "Development of cost effective ultra-high-performance fiber-reinforced concrete using single and hybrid steel fibers," *Constr. Build. Mater.*, vol. 150, pp. 383–394, 2017, doi: 10.1016/j.conbuildmat.2017.06.018.

[36] D. J. Kim, S. H. Park, G. S. Ryu, and K. T. Koh, "Comparative flexural behavior of Hybrid Ultra High Performance Fiber Reinforced Concrete with different macro fibers," *Constr. Build. Mater.*, vol. 25, no. 11, pp. 4144–4155, 2011, doi: 10.1016/j.conbuildmat.2011.04.051.

[37] B. A. Graybeal and F. Baby, "Development of Direct Tension Test Method for Ultra-High- Performance Fiber-Reinforced Concrete," *ACI Mater. J.*, vol. 110, no. 2, 2013, doi: 10.14359/51685532.

[38] A. M. T. Hassan, S. W. Jones, and G. H. Mahmud, "Experimental test methods to determine the uniaxial tensile and compressive behaviour of Ultra High Performance Fibre Reinforced Concrete(UHPFRC)," *Constr. Build. Mater.*, vol. 37, pp. 874–882,

2012, doi: 10.1016/j.conbuildmat.2012.04.030.

[39] K. Wille, S. El-Tawil, and A. E. Naaman, "Properties of strain hardening ultra high performance fiber reinforced concrete (UHP-FRC) under direct tensile loading," *Cem. Concr. Compos.*, vol. 48, pp. 53–66, 2014, doi: 10.1016/j.cemconcomp.2013.12.015.

[40] J. Liu *et al.*, "Combined effect of coarse aggregate and fiber on tensile behavior of ultra-high performance concrete," *Constr. Build. Mater.*, vol. 121, pp. 310–318, 2016, doi: 10.1016/j.conbuildmat.2016.05.039.

[41] B. Chun and D. Y. Yoo, "Hybrid effect of macro and micro steel fibers on the pullout and tensile behaviors of ultra-high-performance concrete," *Compos. Part B Eng.*, vol. 162, no. September 2018, pp. 344–360, 2019, doi: 10.1016/j.compositesb.2018.11.026.

[42] Z. P. Bažant, "Concrete fracture models: Testing and practice," *Eng. Fract. Mech.*, vol. 69, no. 2, pp. 165–205, 2001, doi: 10.1016/S0013-7944(01)00084-4.

[43] E. Denneman, E. P. Kearsley, and A. T. Visser, "Splitting tensile test for fibre reinforced concrete," *Mater. Struct. Constr.*, vol. 44, no. 8, pp. 1441–1449, 2011, doi: 10.1617/s11527-011-9709-x.

[44] B. A. Graybeal, "Practical means for determination of the tensile behavior of ultra-high performaonce concrete," *J. ASTM Int.*, vol. 3, no. 8, 2006, doi: 10.1520/JAI100387.

[45] H. H. Qadir, R. H. Faraj, A. F. H. Sherwani, B. H. Mohammed, and K. H. Younis, "Mechanical properties and fracture parameters of ultra high performance steel fiber reinforced concrete composites made with extremely low water per binder ratios," *SN Appl. Sci.*, vol. 2, no. 9, pp. 1–12, 2020, doi: 10.1007/s42452-020-03425-3.

[46] Z. B. Haber, I. D. la Varga, B. A. Graybeal, B. Nakashoji, and R. El-Helou, "Properties and Behavior of UHPC-Class Materials," *Fhwa-Hrt-18-036*, no. March, p. 153, 2018.

[47] P. S. Song and S. Hwang, "Mechanical properties of high-strength steel fiber-reinforced

concrete," *Constr. Build. Mater.*, vol. 18, no. 9, pp. 669–673, 2004, doi: 10.1016/j.conbuildmat.2004.04.027.

[48] M. Alkaysi, S. El-Tawil, Z. Liu, and W. Hansen, "Effects of silica powder and cement type on durability of ultra high performance concrete (UHPC)," *Cem. Concr. Compos.*, vol. 66, pp. 47–56, 2016, doi: 10.1016/j.cemconcomp.2015.11.005.

[49] O. Bonneau, M. Lachemi, É. Dallaire, J. Dugat, and P. C. Aïtcin, "Mechanical properties and durability of two industrial reactive powder concretes," *ACI Mater. J.*, vol. 94, no. 4, pp. 286–290, 1997, doi: 10.14359/310.

[50] B. A. Graybeal, "Material Property Characterization of Ultra-High Performance Concrete," *Fhwa*, no. FHWA-HRT-06-103, p. 186, 2006.

[51] Z. Ma, T. Zhao, and J. Yang, "Fracture Behavior of Concrete Exposed to the Freeze-Thaw Environment," *J. Mater. Civ. Eng.*, vol. 29, no. 8, p. 04017071, 2017, doi: 10.1061/(asce)mt.1943-5533.0001901.

[52] J. Li, Z. Wu, C. Shi, Q. Yuan, and Z. Zhang, "Durability of ultra-high performance concrete – A review," *Constr. Build. Mater.*, vol. 255, p. 119296, 2020, doi: 10.1016/j.conbuildmat.2020.119296.

[53] Z. Yang, W. J. Weiss, and J. Olek, "Using Acoustic Emission For The Detection Of Damage Caused By Tensile Loading And Its Impact On The Freeze-Thaw Resistance Of Concrete," *Conmat 2015*, no. January, 2005.

[54] C. Magureanu, I. Sosa, C. Negrutiu, and B. Heghes, "Mechanical Properties and Durability of Ultra-High-Performance Concrete," no. 109, pp. 177–184, 2012.

[55] E. Shaheen, N. G. Shrive, S. Allena, and C. M. Newtson, "Optimization of mechanical properties and durability of reactive powder concrete," *ACI Mater. J.*, vol. 104, no. 5, p. 547, 2007.

[56] H. Do Yun and K. Rokugo, "Freeze-thaw influence on the flexural properties of ductile fiber-reinforced cementitious composites (DFRCCs) for durable infrastructures," *Cold Reg. Sci. Technol.*, vol. 78, pp. 82–88, 2012, doi: 10.1016/j.coldregions.2012.02.002.

[57] A. Ogawa, Y. Hitomi, and H. Hoshiro, "PVA-fiber reinforced high performance cement board," in *Proceedings of International Workshop on HPFRCC in Structural Applications*, 2006, pp. 243–251.

[58] K. Rokugo, M. Moriyama, S. C. Lim, and Y. Asano, "Tensile performance of pre-cracked SHCC after freeze-thaw cycles," in *7th International RILEM Symposium on FRC: Design and Application*, 2008, pp. 1071–1078.

[59] S. J. Jang, K. Rokugo, W. S. Park, and H. Do Yun, "Influence of rapid freeze-thaw cycling on the mechanical properties of sustainable strain-hardening cement composite (2SHCC)," *Materials (Basel).*, vol. 7, no. 2, pp. 1422–1440, 2014, doi: 10.3390/ma7021422.

[60] M. Á. Carbonell Muñoz, "Compatibility of ultra high performance concrete as repair material : bond characterization with concrete under different loading scenarios," Michigan Technological University, Houghton, Michigan, 2012.

[61] K. M. Zmetra, K. F. McMullen, A. E. Zaghi, and K. Wille, "Experimental Study of UHPC Repair for Corrosion-Damaged Steel Girder Ends," *J. Bridg. Eng.*, vol. 22, no. 8, p. 04017037, 2017, doi: 10.1061/(asce)be.1943-5592.0001067.

[62] B. Shafei, B. Phares, and W. Shi, "Beam End Repair for Prestressed Concrete Beams," 2711 South Loop Drive, Suite 4700 Ames, IA 50010-8664, 2020.

[63] A. Ramachandra Murthy, B. L. Karihaloo, P. Vindhya Rani, and D. Shanmuga Priya, "Fatigue behaviour of damaged RC beams strengthened with ultra high performance fibre reinforced concrete," *Int. J. Fatigue*, vol. 116, no. December 2017, pp. 659–668,

2018, doi: 10.1016/j.ijfatigue.2018.06.046.

[64] M. Ahmadi, “END REGIONS REPAIR OF PRESTRESSED GIRDERS FOR RESTORING THE SHEAR CAPACITY USING UHPC, FR-SCC, AND MALP,” University of Oklahoma, 2021.

[65] P. M. Huynh, “METHOD OF REHABILITATION FOR CORROSION DAMAGE IN THE END REGION OF PRESTRESSED CONCRETE BRIDGE GIRDERS,” University of Oklahoma, 2021.

[66] Y. Dyachkova, “EFFECT OF STEEL FIBER CONTENT ON MECHANICAL PROPERTIES OF NON- PROPRIETARY ULTRA-HIGH PERFORMANCE CONCRETE.,” University of Oklahoma, 2020.

[67] Astm C1437, “Standard Test Method for Flow of Hydraulic Cement Mortar,” *ASTM Int. West Conshohocken, PA*, 2020.

[68] ASTM C39, “Standard Test Method for Compressive Strength of Cylindrical Concrete Specimens,” *ASTM Int. West Conshohocken, PA*, 2014.

[69] ASTM C469, “Standard Test Method for Static Modulus of Elasticity and Poisson’s Ratio of Concrete,” *ASTM Stand.*, pp. 2–6, 2014, doi: 10.1520/C0469_C0469M-14E01.

[70] ASTM C78, “Standard Test Method for Flexural Strength of Concrete (Using Simple Beam with Third-Point Loading),” *ASTM Int. West Conshohocken, PA*, 2021.

[71] ASTM C496, “Standard Test Method for Splitting Tensile Strength of Cylindrical Concrete Specimens,” *ASTM Int. West Conshohocken, PA*, 2017.

[72] Astm C666, “Standard Test Method for Resistance of Concrete to Rapid Freezing and Thawing,” *ASTM Int. West Conshohocken, PA*, 2015, doi: 10.1520/C0666.

[73] ASTM C1856, “Standard Practice for Fabricating and Testing Specimens of Ultra-High Performance Concrete,” *ASTM Int. West Conshohocken, PA*, 2017.

[74] ASTM C1609, "Standard Test Method for Flexural Performance of Fiber-Reinforced Concrete (Using Beam With Third-Point Loading)," *ASTM Int. West Conshohocken, PA*, 2019.

[75] R. Campos, "EFFECT OF FIBER CONTENT ON TENSILE STRENGTH OF NON-PROPRIETARY ULTRA HIGH PERFORMANCE CONCRETE," University of Oklahoma, 2020.

[76] "AASHTO LRFD bridge design specifications," *Washington, D.C. Am. Assoc. State Highw. Transp. Off.*, 2017.

[77] J. Ma, M. Orgass, F. Dehn, D. Schmidt, and N. V. Tue, "Comparative Investigations on Ultra-High Performance Concrete with or without Coarse Aggregates," in *Proceedings of the international symposium on ultra high performance concrete, Kassel*, 2004, no. September, pp. 205–212.